Versuchsanstalt für Wasserbau
Hydrologie und Glaziologie
der Eidgenössischen
Technischen Hochschule Zürich

**Mitteilungen 233**

# On the uncertainties in glacier mass balance modelling

Jeannette Gabbi

Zürich, 2015

Herausgeber: Prof. Dr. Robert Boes

*Zitiervorschlag für VAW-Mitteilungen:*

Gabbi J. (2015).
On the uncertainties in glacier mass balance modelling.
*VAW-Mitteilungen* 233, Versuchsanstalt für Wasserbau, Hydrologie und Glaziologie (VAW),
(R. M. Boes, ed.), ETH Zürich, Schweiz.

Im Eigenverlag der
Versuchsanstalt für Wasserbau,
Hydrologie und Glaziologie
ETH Zürich
CH-8093 Zürich

Tel.: +41 - 44 - 632 4091
Fax: +41 - 44 - 632 1192
e-mail: info@vaw.baug.ethz.ch

Zürich, 2015

ISSN 0374-0056

# Preface

Glaciers are an important source of water for large sections of the Alps and their variations are among the clearest natural indicators of ongoing climate change. The well-documented retreat of alpine glaciers in the past decades is still one of the clearest signs that the energy balance on the earth's surface has changed significantly in recent times. The expected reduction in ice volume in the coming decades will lead first to increased and later to diminished annual runoff, depending on the glaciated and catchment areas. This will also affect the discharge regime. Glacier shrinkage impacts many sectors that depend on glacier meltwater, such as hydropower, fresh water supply and irrigation, as well as tourism.

This research work was conducted as part of the National Research Programme NRP61 "Sustainable water management" project, aiming to better understand how future glacier evolution under climate change will affect water resources. In the context of the current debate on climate change, the relation between glaciers and climate is still an important research topic. A main aspect of this work was the assessment of the impacts of uncertainties affecting the results of modelling glacier surface mass balance over periods of several decades. This could only be achieved thanks to the available data for several glaciers (surface mass balances and volume changes) covering a time period of almost one century.

This work contains three main parts: (1) an assessment of the impact of uncertainties in the ice thickness distribution within a glacier on the runoff projections in a glacial catchment, (2) a comparison of the performance of different glacier surface melt models for long-term simulations of glacier response, and (3) an evaluation of the impact of Saharan dust and black carbon on the albedo and long-term glacier mass balance. The main outcome of this work highlights the complexities and interlinks between climate and glacier changes, and provides several contributions for an improved modeling of the relevant processes.

Zurich, April 2015 Martin Funk

# Contents

# Abstract

Global warming has led to a substantial retreat of mountain glaciers all over the world. Sound knowledge of the glacier response to climate variability is essential to make reliable predictions of the future glacier evolution. Long-term mass balance simulations are subject to considerable uncertainties with respect to climate input data and model approach. This thesis aims providing an improved understanding of glacier mass balance modelling over periods of several decades in order to reduce uncertainties and better constrain the dimension of future glacier and runoff changes. In particular, implications of the initial ice-thickness distribution, the melt model approach and variations in surface albedo on glacier mass balance are examined in detail.

The ice-thickness distribution is an important prerequisite for many glaciological applications, especially for simulating the future glacier evolution. Helicopter-borne ground penetrating radar (GPR) measurements provide a unique tool to infer the glacier-wide ice-thickness distribution, as large areas can be recorded in short time. Based on a dense network of ground- and helicopter-based GPR measurements the ice-thickness distribution in the Mauvoisin region (Swiss Alps), comprising a glacier coverage of $63\,\mathrm{km}^2$, was derived. A total ice volume of $3.69 \pm 0.31\,\mathrm{km}^3$ was computed. The measurement-based ice thickness distribution was then compared to an ice-thickness estimation approach which infers the ice thickness based on surface characteristics. Results showed that the estimation approach overestimated the total ice volume by 36%. Furthermore, glacio-hydrological modelling was performed and glacier and runoff projections into the 21st century were calculated. A sensitivity analysis, evaluating the impact of an erroneous ice-thickness distribution on runoff simulations, showed that an accurate estimation of the ice volume is indispensable for making reliable predictions of future runoff changes.

Furthermore, an accurate modelling of the melt process is essential to simulate the glacier evolution under changing climate conditions. There is a gradual transition from simple degree-day models, using temperature as sole index, to physically-based energy balance models accounting for all energy fluxes at the glacier-atmosphere interface. In a comparative analysis, the performance of five different melt models (a classical, three enhanced temperature-index models and an energy-balance model) was investigated over a multi-decadal period for Rhonegletscher (Swiss Alps). Detailed seasonal mass balance measurements of the years 2006-2012, including subseasonal stake readings and extensive snow depth surveys, served for model calibration. Very little difference in performance among the melt models was noticeable over the calibration period. Only the energy-balance model showed less consistency with observation, probably due to the forcing with data of an off-glacier weather station which might poorly predict the conditions in the glacier-boundary layer. Volume changes of six subperiods between 1929 and 2012 served for model validation over the long-term. Results indicated that models including a separate term for shortwave radiation agree best with observations. More empirical approaches, directly linking melt rate with temperature, seem to be oversensitive to changes in the temperature regime and require recalibration for distinct climate conditions.

In addition to the type of melt equation, also an accurate simulation of variations in snow and ice surface albedo is important for reliable estimates of the glacier response to climate changes. Light-absorbing impurities, as mineral dust or black carbon (BC), strongly affect the albedo of snow/ice surface and thus the glacier mass balance. In the Alps, mineral dust deposits mainly comprise long-range transported crustal impurities i.e. Saharan dust. Based on a 100-year record of seasonal mass balance measurements the effect of Saharan dust and BC over the period 1914-2014 was assessed. The analysis was performed for two locations on Claridenfirn (Swiss Alps): a site in the accumulation area experiencing mainly mass gain and a site migrating from mass gain to predominately mass loss conditions. A coupled mass balance and snow/firn layer model was developed. Atmospheric deposition rates of Saharan dust and BC were retrieved from ice/firn cores of two high-alpine sites. The combined effect of Saharan dust and BC enhanced annual melt over 1914-2014 by 14-18% on average. Results suggest that BC has a substantially stronger impact on mass balance than Saharan dust. The annual mass balance is reduced by 21-41 mm $a^{-1}$ due to the presence of Saharan dust and by 177-293 mm $a^{-1}$ due to BC. The mass balance change induced by snow impurities is dependent on the location: conditions with mainly positive mass balances lead to a continuous burial of impurity-loaded layers, whereas sites dominated by negative mass balances show a pronounced re-exposure of buried impurity-enriched layers. Moreover, the analysis showed that in periods of intense melting, as observed in the 1940s and 2000s, similar impurity concentrations as in years with exceptionally large deposition rates may be achieved.

# Zusammenfassung

Die globale Erwärmung hat zu einem rasanten Gletscherrückzug geführt, der weltweit zu beobachten ist. Fundierte Kenntnisse über den Zusammenhang zwischen Klima und Gletscherschwankungen sind unerlässlich, um aussagekräftige Prognosen über die zukünftige Entwicklung von Gletschern zu machen. Massenbilanzberechnungen über längere Zeiträume werden durch verschiedene Unsicherheiten beeinflusst, wobei insbesondere Unklarheiten über die vorherrschenden Klimabedingungen und den Modellansatz einen Einfluss ausüben. Diese Arbeit trägt zu einem besseren Verständnis von Modellierungen der Massenbilanz über Zeiträume von mehreren Jahrzehnten bei, mit dem Ziel Unsicherheiten zu reduzieren und zukünftige Gletscher- und Abflussveränderungen besser prognostizieren zu können.

Basierend auf einem dichten Netz an boden- und helikoptergestützten Radarmessungen wurde die Eisdickenverteilung im Mauvoisin Gebiet (Schweizer Alpen) bestimmt. Das Untersuchungsgebiet weist heutzutage eine verglescherte Fläche von 63 $km^2$ auf, welche auf fünf grössere (5-18 $km^2$) und mehrere kleinere Gletscher ($<5$ $km^2$) verteilt ist. Mittels der Messungen wurde ein Eisvolumenvorkommen von $3.69 \pm 0.31$ $km^3$ für das Gebiet bestimmt. Diese messgestützte Eisdickenverteilung wurde dann mit dem Resultat eines etablierten Eisdickenabschätzungsansatzes verglichen, welcher ausgehend von der Oberflächentopographie die Eisdicke bestimmt. Dabei hat sich gezeigt, dass der Abschätzungsansatz das Eisvolumen im Durchschnitt um 36% überschätzt. In einem nächsten Schritt wurden Gletscher- und Abflussprognosen für die Vergangenheit und Zukunft erstellt (1900-2100). Mittels einer Sensitvitätsanalyse wurde untersucht wie stark sich Unsicherheiten in der Eisvolumenberechnung auf Abflussprognosen auswirken. Dabei wurde festgestellt, dass genaue Kenntnisse über die Eisdickenverteilung im Untersuchungsgebiet wesentlich sind, um eine verlässliche Aussage über die Ablussentwicklung bis zum Ende des 21. Jahrhunderts machen zu können.

Für die Modellierung des Gletscherverhaltens unter sich ändernden Klimabedingungen ist eine exakte Modellierung der Schmelze unabdingbar. Gletscherschmelze kann mittels unterschiedlich komplexen Schmelzmodellen berechnet werden, wobei ein fliessender Übergang zwischen empirischen Schmelzmodellen, die im wesentlichen nur die Temperatur als Input benötigen, und physikalischen Energie-Bilanz-Modellen, welche alle Energieflüsse an der Gletscheroberfläche berücksichtigen, besteht. In einer Vergleichsstudie wurde das Langzeitverhalten von fünf verschiedenen Schmelzmodellansätzen (ein klassisches, drei erweiterte Temperatur-Index-Schmelzmodelle und ein Energie-Bilanz-Modell) über eine Periode von mehreren Jahrzehnten für den Rhonegletscher (Schweizer Alpen) analysiert. Saisonale Massenbilanzmessungen mit subsaisonalen Pegelablesungen und flächendeckenden Schneehöhensondierungen der Jahren 2006-2012 dienten zur Kalibrierung der Modellparameter. Über die Kalibrationsperiode, zeigen alle Modell eine gute Korrelation mit den Messungen. Davon ausgenommen ist das Energie-Bilanz-Modell, welches etwas stärker von den beobachteten Massenbilanzen abweicht. Der Grund für das schlechte Abschneiden des physikalischen Modells könnte in der Unsicherheit über die Extrapolation der gemessenen Energieflüsse liegen und der Verwendung von meteorologischen

Daten, die ausserhalb des Gletschers gemessen wurden. Anhand von Volumenänderungen von sechs Perioden, welche die Jahre 1929-2012 abdecken, wurde die Langzeiteffizienz der Schmelzmodelle getestet. Dabei hat sich gezeigt, dass nur Modelle, welche einen separaten Term für die Strahlungsbilanz beinhalten, fähig sind dem generellen Trend der vergangenen Eisvolumenveränderungen zu folgen. Schmelzmodellansätze, welche die Schmelze direkt aus der Lufttemperatur herleiten, scheinen zu empfindlich auf Änderungen im Temperaturregime zu reagieren und benötigen eine Anpassung der Modellparameter für die jeweiligen Klimaverhältnisse.

Neben dem Schmelzmodellansatz, müssen auch Veränderungen im Oberflächenalbedo berücksichtigt werden, um eine verlässliche Aussage über die Gletscherschmelze zu machen. Lichtabsorbierende Partikel in Schnee und Eis kontrollieren die Albedo und somit auch die Massenbilanz. Zu den lichtabsorbierende Partikel auf Alpengletschern zählen in erster Linie Russpartikel sowie Mineralstaub, welcher zu einem grossen Teil aus Sahara Staub besteht. Basierend auf einer kontinuierlichen Messreihe mit saisonalen Massenbilanzen, welche eine Periode von 100 Jahren abdeckt, wurde die Massenbilanz am Claridenfirn (Schweizer Alpen) über die Periode 1914-2014 modelliert, um den Langzeiteffekt von Sahara Staub und Russpartikel auf die Schmelze zu untersuchen. Die Analyse wurde an zwei Standorten durchgeführt: eine Messstelle, die sich im Akkumulationsgebiet befindet und eine zweite, die im Verlaufe der Zeit vom Akkumulations- ins Ablationsgebiet wandert. Für die Analyse wurde ein kombiniertes Massenbilanz und Schnee/Firnschichtenmodell verwendet. Atmosphärische Ablagerungsraten von Mineralstaub und Russ wurden anhand von zwei Eisbohrkernen vom Colle Gnifetti (Walliser Alpen) und Fiescherhorn (Berner Alpen) hergeleitet. Der kombinierte Effekt von Sahara Staub und Russ hat die jährliche Schmelzmenge im Durchschnitt um 14-18% erhöht, wobei Russpartikel einen deutlich grösseren Einfluss auf die Schmelze ausüben im Vergleich zu Sahara Staub. Durch die Anwesenheit von Sahara Staub im Schnee und Firn wird die jährliche Massenbilanz durchschnittlich um 21-41 mm $a^{-1}$ reduziert, durch Russpartikel um 177-293 mm $a^{-1}$. Der Einfluss von lichtabsorbierenden Verunreinigungen hängt aber stark vom Standort ab. Während am oberen Pegel die Staubschichten kontinuierlich durch den Winterschnee überdeckt werden, führen negativen Massenbilanzen am unteren Pegel zur Freilegung von bereits vergrabenen Staubschichten und somit zu einem beschleunigten Abschmelzen. Desweiteren hat die Studie gezeigt, dass in Perioden mit intensiver Schmelze, wie das in den 1940er und 2000er Jahren zu beobachtet war, ähnlich hohe Staubkonzentrationen an der Oberfläche erreicht werden können wie in Jahren mit sehr grossem atmosphärischem Eintrag.

# Chapter 1

# Introduction

## 1.1 Glaciers in the context of climate change

Glaciers are directly linked to atmospheric changes and are among the best natural indicators of climate variability due to their proximity to melt conditions (Houghton et al., 2001). The close relationship between snow/ice melt and air temperature (e.g. Ohmura, 2001) is responsible for the sensitivity of the cryosphere to temperature fluctuations. The increase in the global mean air temperature, observed since the late 19th century, is the main cause for the severe shrinkage of mountain glaciers and ice sheets all over the world (Gardner et al., 2013). Since the beginning of the 20th century global temperature has increased by about 0.85°C on average, with a more rapid increase since the 1950s (IPCC, 2013). The observed global warming can not be explained by internal variability alone and is primarily a result of increasing anthropogenic emissions of greenhouse gases whereas natural forcing (i.e. solar forcing) accounts for a relatively small share of the total temperature increase. According to climate projections into the 21st century, based on the assumption of sustained greenhouse gas emissions, a further rise in global mean temperature of 0.3–0.7°C for near-term climate (2016-2035) and 2–4°C for long-term climate (1981-2100) compared to present (1986-2005) is expected (IPCC, 2013). A temperature change of this magnitude will have profound consequences on the cryosphere, with further impacts on the environment and human life.

The Alpine environment is particularly sensitive to fluctuations in the climate system and the effects of climate change are already visible, as shown by the rapid volume losses of many Alpine glaciers (e.g. Bauder et al., 2007; Zemp et al., 2008). Since the middle of the 19th century, glaciers in the Alps have lost almost 70% of their initial ice volume (Haeberli et al., 2007). Due to a high population density in the Alpine region and the surrounding lowlands, future changes of mountain glaciers will have a strong impact on society (Kaser et al., 2010) despite the diminishingly small fraction of glacier covered area in the European Alps compared to global ice coverage. Glaciers act as huge fresh water reservoirs and play a crucial role in the hydrological cycle affecting the volume, the seasonal distribution and the water quality of runoff. The Alps, in particular the Swiss part, are known as "Water towers of Europe" (EEA, 2009) and form the source regions of the many major rivers in the Western and Central Europe flowing to North Sea (Rhine river), to the Mediterranean (Rhone river), the Adriatic (Ticino/Po river) and the Black sea (Inn/Danube). Corresponding headwaters are characterized by a considerable degree of glacier coverage and runoff of this regions consists to a larger part of melt water from snow and ice. Expected changes in glacier and snow cover will affect the runoff regime of Alpine rivers, but also the lowlands will experience a significant reduction of summer runoff due to the glacier retreat (Huss, 2011; Beniston and Stoffel, 2014).

Currently a total ice volume of $74 \pm 9\,km^3$ is stored in ice bodies in the Swiss Alps (Farinotti et al., 2009a) which is expected to decline dramatically in future. Regional climate projections for Switzerland (CH2011, 2011) enable to investigate future glacier changes. By the end of the 21st century, about 86–94% of the current glacier covered area in the Swiss Alps is expected to be vanished (Huss, 2012). The retreat of Alpine glaciers will severely constrain the water availability required for drinking water, irrigation and hydropower production. Furthermore, the potential risk of floods and other natural hazards is expected to increase and the economy and tourism sector will be threatened by changes in the climate forcing (Beniston, 2012). In this respect, precise knowledge about the impact of the climate change on cryosphere and potential implications on the human society are of crucial importance. Data on past glacier changes are therefore a key element for understanding the interaction of climate and glaciers and enable us to predict how glaciers will respond in future. Consequently, long and continuous records are of inestimable value.

## 1.2 Evidence of glacier changes in the Swiss Alps

Measurements of glacier mass balance have a long history in the Swiss Alps and earliest records date back to the late 19th century. In 1885, first direct mass balance measurements (using stake and snow pits; Cogley, 2010) were performed on Rhonegletscher and maintained for about two decades (Mercanton, 1916). The worldwide longest continuous time series of direct mass balance observations exist for Claridenfirn where since 1914 the glacier mass balance has been recorded at two sites providing an almost complete record of seasonal mass balance measurements for a 100-year period (Müller and Kappenberger, 1991). Shortly thereafter, additional mass balance observations started at Silvrettagletscher and Grosser Aletschgletscher. Since the 1950s–1960s, glacier-wide mass balance monitoring programs were successively initiated at several glaciers in the Swiss Alps (Limmern/Plattalvagletscher, Gries- and Silvrettagletscher, Glacier du Giétro, Glacier de Tsanfleuron, Ghiacciaio del Basòdino, Glacier de Corbassière, Allalin- and Schwarzberggletscher; Aellen, 1995). More recently, mass balance surveys have been launched on Findelen-, Rhone- and Pizolgletscher. Direct mass balance measurements provide accurate point mass balance data at high temporal resolution and are optimally complemented by indirect mass balance measurements of ice volume changes yielding glacier changes with a broad surface coverage but at lower temporal resolution. Comparison of digital elevation models of different years derived from topographic maps (historical and official national maps) or areal photographs (available since the 1960s) provide evidence of ice volume changes in the Swiss Alps over the last 100-150 years (Bauder et al., 2007). More recently also space-borne systems have been used to derive digital elevation models of glacier surface propagation inheriting the ability to cover large and remote areas at high temporal resolution, but with a lower accuracy compared to airborne data (e.g. Kääb, 2008; Berthier et al., 2010; Hurkmans et al., 2014).

## 1.3 Glacier mass balance modelling

Understanding the sensitivity of surface mass balance to climate change is essential for evaluating the effect of present and future climate change in mountain areas. Continuous mass balance modelling therefore presents a useful tool to assess the relation between climate forcing and glacier mass balance. Furthermore, homogenization of mass balance records achieving

consistency in spatial and temporal variations of glacier mass changes (Huss et al., 2009a) as well as glacier projections into the future rely on mass balance modelling.

In order to calculate the glacier evolution, distributed mass balance models have been coupled to ice flow models. In the past, a large number of such combined mass balance and glacier evolution models have been proposed (e.g. Schneeberger et al., 2001; Gerbaux et al., 2005; Huss et al., 2008b; Machguth et al., 2009; Jouvet et al., 2011; Dumont et al., 2012). They substantially differ in complexity and incorporate various approaches for modelling ablation, accumulation and ice dynamics with different demands in terms of input and calibration data.

## Ablation modelling

The interaction between glacier and climate conditions has been intensively studied in the past. Already in the early 19th century the relationship between the climate variables, air temperature and solar radiation, and melt was recognized (Finsterwalder and Schunk, 1887; Hess, 1904). Since then, a wide variety of melt models with different numbers of meteorological variables have been developed. These range from most simple models relating melt directly to air temperature to sophisticated energy-balance models considering all relevant energy fluxes in the glacier-atmosphere boundary layer. A detailed overview about the different melt model approaches is given in Hock (2003, 2005).

*Classical temperature-index or degree-day melt models*: Classical degree-day melt models relate melt by a proportionality factor (i.e. melt factor) directly to the sum of positive air temperatures:

$$M = \begin{cases} f_{\mathrm{M}} \left( T_{\mathrm{a}} - T_{\mathrm{T}} \right) & : \quad T_{\mathrm{a}} > T_{\mathrm{T}} \\ 0 & : \quad T_{\mathrm{a}} \leq T_{\mathrm{T}} \end{cases} \tag{1.1}$$

where $M$ is the melt, $f_{\mathrm{M}}$ is the melt factor, $T_{\mathrm{a}}$ the air temperature and $T_{\mathrm{T}}$ the threshold temperature distinguishing for the onset of melt. The close relationship between air temperature and melt rates is given by the high correlation between air temperature and several components of the energy balance (e.g. Braithwaite and Olesen, 1990; Lang and Braun, 1990; Ohmura, 2001). The main disadvantage of these approaches is that melt factors vary strongly in space and time (Braithwaite, 1995) due to changes in the relative contribution of individual energy-balance components to melt as a response to changes in direct solar radiation and surface albedo. Hence, melt factors require recalibration for each site and for distinct climate conditions (Carenzo et al., 2009).

*Enhanced temperature-index melt models*: As a response to this inability, extended formulations of the classical temperature-index model were developed incorporating additional meteorological variables such as shortwave or net radiation, wind speed or vapour pressure (e.g. Zuzel and Cox, 1975; Kustas and Rango, 1994; Brubaker et al., 1996; Tangborn, 1999). Often solar radiation is incorporated into the melt equation which allows accounting for topographic effects such as slope, aspect and shading yielding better spatial results compared to the simple temperature-index models. One of the most common and most widely used enhanced temperature-index model is the formulation by Hock (1999) in which the melt factor varies as a function of potential clear-sky direct solar radiation, $I_{\mathrm{pot}}$:

$$M = \begin{cases} \left( f_{\mathrm{M}} + a * I_{\mathrm{pot}} \right) T_{\mathrm{a}} & : \quad T_{\mathrm{a}} > T_{\mathrm{T}} \\ 0 & : \quad T_{\mathrm{a}} \leq T_{\mathrm{T}} \end{cases} \tag{1.2}$$

where $a$ is a coefficient. This formulation has the advantage that no additional meteorological data in addition to temperature are needed. Other commonly used approaches (e.g. Cazorzi and Fontana, 1996; Pellicciotti et al., 2005) includes a separate term for net or shortwave radiation balance, $R$, and have the general form of:

$$M = \begin{cases} f_M T_a + a R & : \quad T_a > T_T \\ 0 & : \quad T_a \leq T_T. \end{cases} \tag{1.3}$$

*Energy-balance models*: In contrast to empirical melt models, physically-based energy balance models evaluate all energy fluxes at the glacier-atmosphere interface. The energy balance at the glacier surface is defined as

$$Q_N + Q_H + Q_L + Q_G + Q_R + Q_M = 0, \tag{1.4}$$

where $Q_N$ is the net radiation, $Q_H$ and $Q_L$ the turbulent heat fluxes (sensible and latent heat), $Q_G$ the ground heat flux, $Q_R$ the heat flux supplied by rain and $Q_M$ the melt energy (Hock, 2005). Melt rates are derived by the melt energy and the latent heat of fusion. Numerous distributed energy balance models have been proposed in the past (e.g. Hock and Holmgren, 2005; Anslow et al., 2008; Mölg et al., 2008; MacDougall and Flowers, 2011). Energy-balance modelling, however, requires accurate knowledge about the magnitude of the energy fluxes which is often only available at the point scale and for short periods of time. For distributed energy-balance modelling the required variables have to be extrapolated to the glacier-scale which introduces large uncertainties in the melt modelling.

Temperature-index models have been widely used for distributed modelling due to their simplicity, their low data requirements and their general good performance. Temperature data are often the only available meteorological variable and is relatively easily to extrapolate and forecast which further emphasize the precedence of temperature-index models over data-intense energy-balance models.

## Accumulation modelling

In addition to ablation processes, a correct simulation of the accumulation is crucial for reliable estimates of the glacier mass balance as winter accumulation has a major control on the timing of ice exposure and thus melt rates. The snow accumulation pattern is controlled by (1) preferential snow deposition, (2) wind induced snow redistribution and (3) gravitational snow transport (i.e. avalanches, snow slides; Kuhn, 1995; Lehning et al., 2008). The processes mentioned and the circumstance that measurements of solid precipitation in high mountain areas are subject to large uncertainties (Sevruk, 1985) make it difficult to predict snow accumulation (Dadic et al., 2010). Since wind fields in steep terrain are highly complex, drifting snow is therefore often rudimentary implemented in mass balance models, basically as a function of terrain parameters (Liston and Sturm, 1998; Winstral and Marks, 2002; Winstral et al., 2013). More recent approaches use the output of mesoscale atmospheric models to derive more realistic wind fields for steep topographies and are able to capture large-scale patterns of snow depositions (e.g. Lehning et al., 2008; Raderschall et al., 2008; Schneiderbauer and Prokop, 2011; Vionnet et al., 2014). Gravitational snow transport involves redistribution of snow from higher to lower elevations and may strongly affect the snow pattern (Strasser

et al., 2008). For glacier mass balance studies, in general simplified parameterisations for gravitational redistribution are applied which calculate snow transport and deposition by flow routing based on topography (Gruber, 2007; Bernhardt and Schulz, 2010).

Glacier mass balance models often compute distributed snow accumulation from precipitation measurements of nearby weather stations in combination with lapse rates, from gridded precipitation data sets or from the output of climate models applying a threshold temperature for liquid and solid precipitation (Hock, 1999; Finger et al., 2012; Salzmann et al., 2012). More sophisticated models include in addition simple parameterisations for snow redistribution processes based on terrain parameters (e.g. Huss et al., 2008a; Carenzo, 2012; Mayr et al., 2013).

### Ice dynamics

Glacier geometry changes as a response to climate fluctuations are a result of surface mass balance and ice flow dynamics. Several approaches for the ice dynamics of alpine glaciers have been developed in the past, ranging from simple flowline models (Oerlemans, 1997; Sugiyama et al., 2007) to sophisticated three-dimensional ice flow models (e.g. Blatter, 1995; Gudmundsson, 1999; Jouvet et al., 2008). However, such approaches require extensive input data, computational time and are not easy applicable for large scale catchments. Recently, a simple method to parameterise ice flow has been proposed and validated by Huss et al. (2010), based on glacier surface elevation and ice thickness changes, which allows accounting for ice flow but is far less computational demanding than complex numerical ice flow models.

### Ice-thickness distribution

Knowledge about the total ice volume and the spatial distribution is needed for many glaciological applications such as ice flow modelling studies and for glacier projections. Ice-thickness can be locally deduced from borehole measurements or over a larger area from ground-penetrating radar measurements. Both techniques demand for inter- and extrapolation of point measurements to assess the spatial distribution of the ice volume. A simple and wide-spread approach is the glacier volume-area scaling, where ice volume is calculated as a power law function of the surface area (Chen and Ohmura, 1990; Bahr et al., 1997; Radić and Hock, 2008). Other empirical approaches estimate the ice-thickness based on surface slope assuming perfect plasticity and an average basal shear stress (Haeberli and Hoelzle, 1995; Li et al., 2012). Alternatively, numerous physically-based approaches have been proposed which infer the spatially distributed ice-thicknesses from surface characteristics using the glaciers mass turnover and principles of ice flow mechanics (e.g. Farinotti et al., 2009b; Huss and Farinotti, 2012; Paul and Linsbauer, 2012; Mcnabb et al., 2012; Clarke et al., 2013; van Pelt et al., 2013; Michel-Griesser et al., 2014).

## 1.4 Objectives

A wide variety of studies have modelled glaciers and associated changes in the runoff regime in the past and/or into the future on a local (e.g. Farinotti et al., 2011; Uhlmann et al., 2013), regional (e.g. Huss, 2012; Kääb et al., 2012) or global scale (e.g. Giesen and Oerlemans, 2013; Radic et al., 2014). Such distributed simulations over long-term periods are subject to a high

level of uncertainty arising from unknown climate input data and insufficient understanding of the climate-glacier feedback (e.g. Kobierska et al., 2013; Linsbauer et al., 2013; Huss et al., 2014). Uncertainties in the climate forcing are mainly related to the quality and representativeness of meteorological time series and the extrapolation to the glacier-scale as well as to the climate model and downscaling techniques in case of future projections. Furthermore, the modelled time evolution of glaciers is affected by uncertainties in the ice-thickness distribution and in the modelling of mass balance and ice flow dynamics. This thesis aims to reduce uncertainties in long-term mass balance modelling and thus to improve the accuracy and reliability of glacier and runoff simulations for the past and future. Moreover, the study contributes to a better understanding of the melt process by analysing the transferability of melt model parameters in time. The thesis focuses on two main subjects: firstly on the significance of the ice volume and the ice-thickness distribution and secondly on the precise representation of melt. Sound knowledge about the spatial ice-thickness distribution is essential for glacier retreat simulations and for runoff projections as the initial ice volume defines the water resources stored in the ice body. However, the ice-thickness distribution is difficult to measure and often modelling approaches are applied to infer the ice volume. The objective of the thesis is to show limitations of ice-thickness estimation approaches and to demonstrate the impact of an inaccurate ice volume estimates on runoff projections. The major focus of the thesis is on the melt process as glacier melt has a central role in mass balance modelling. Different melt model approaches have been proposed in the past, differing substantially in their complexity and their demands of input data. At the point-scale with known input data, physically-based energy balance models clearly outmatch empirical melt models. However, for modelling studies over long-term periods extending over several decades and at the scale of a whole glacier, it is less clear which approach provides best results. Accordingly, the study aims providing indications which melt relationships are robust in time and thus suited for long-term mass balance simulations with respect to an improved melt modelling over decadal periods and under a changing climate. Furthermore, emphasize is put on surface albedo since shortwave radiation controls the energy balance at the glacier surface and consequently temporal and spatial variation in surface albedo have a controlling influence on melt (Sicart et al., 2002). Light-absorbing impurities exert a considerable effect on the albedo of snow and ice surfaces. During conditions of melt, snow impurities are partly retained at the glacier surface leading to melt amplification. This thesis attempts to identify the contribution of light-absorbing impurities to glacier melt over multi-decadal periods in order to gain new insight into long-term changes in surface albedo and their impact on glacier mass balance. Particular attention is focused on differences between prevailing accumulation and ablation conditions.

## 1.5 Structure of the thesis

The thesis is composed of three separate and self-contained chapters on the influence of 1) the ice-thickness distribution, 2) the melt model approach and 3) the surface albedo (i.e. the influence of snow impurities) on the long-term simulations of the glacier response. Each chapter consists of an introduction, data and methods, results, discussion and conclusions sections. The thesis is completed by an overall conclusion and an outlook showing the potential for further analysis based on the findings of this work.

In the following an overview about the content of the main chapters is presented:

**Chapter 2: "Ice volume distribution and implications on runoff projections in a glacierized catchment"**

This chapter is published under the same title in *Hydrology and Earth System Sciences* (Gabbi et al., 2012). Based on a comprehensive set of helicopter-based ground penetrating radar measurements in combination with an ice-thickness estimation approach we determined the bedrock topography of the glaciers in the Mauvoisin region (Valais Alps, Switzerland). The ice-thickness distribution was then used as input for a combined glacio-hydrological model to derive glacier and runoff projections for the 21st century. We assessed the impact of the ice-thickness distribution on runoff projections and showed that an accurate estimate of the ice volume is crucial for reliable glacier and runoff simulations into the future.

**Chapter 3: "A comparison of empirical and physically-based glacier surface melt models for long-term simulations of glacier response"**

This chapter is published under the same title in *Journal of Glaciology* (Gabbi et al., 2014). The performance of five glacier melt models with different complexities is examined over a multi-decadal period in order to assess the suitability to model glacier projections. The analysis comprises a classical temperature-index model, three enhanced temperature-index models as well as a full energy-balance model. Results revealed that models with intermediate sophistication, including the full shortwave radiation balance, perform best over long-term periods. In contrast, the relationships of more empirical approaches do not seem to be robust in time due to their oversensitivity to temperature fluctuations.

**Chapter 4: "The impact of Saharan dust and black carbon on albedo and long-term glacier mass balance"**

This chapter is prepared for submission to *The Cryosphere* (Gabbi et al., 2015). The long-term effect of Saharan dust and other light-absorbing snow impurities on the surface albedo and mass balance of an Alpine glacier is analyzed. The employed model includes a parameterisation for snow albedo accounting for the effect of mineral dust and black carbon and a snow density model in order to track the snow and impurity layers in time. Results suggest that in years with a very high supply of Saharan dust or in melt-intense periods as in the late 1940s and 2000s, snow impurities substantially affect the glacier mass balance.

# Chapter 2

# Ice volume distribution and implications on runoff projections in a glacierized catchment

J. Gabbi[1], D. Farinotti[1], A. Bauder[1] and H. Maurer[2]

[1]Laboratory of Hydraulics, Hydrology and Glaciology (VAW), ETH Zürich, Zürich, Switzerland
[2]Institute of Geophysics, ETH Zürich, Zürich, Switzerland

Published, Hydrology and Earth System Sciences

**Citation** Gabbi J., D. Farinotti, A. Bauder, and H. Maurer (2012). Ice volume distribution and implications on runoff projections in a glacierized catchment. *Hydrology and Earth System Sciences*,16,1-14,doi:10.5194/hess-16-1-2012.

**Abstract**

A dense network of helicopter-based ground penetrating radar (GPR) measurements was used to determine the ice-thickness distribution in the Mauvoisin region. The comprehensive set of ice-thickness measurements was combined with an ice-thickness estimation approach for an accurate determination of the bedrock. A total ice volume of $3.69 \pm 0.31\,\mathrm{km}^3$ and a maximum ice-thickness of 290 m were found. The ice-thickness values were then employed as input for a combined glacio-hydrological model forced by most recent regional climate scenarios. This model provided glacier evolution and runoff projections for the period 2010–2100. Runoff projections of the measured initial ice volume distribution show an increase in annual runoff of 4 % in the next two decades, followed by a persistent runoff decrease until 2100. Finally, we checked the influence of the ice-thickness distribution on runoff projections. Our analyses revealed that reliable estimates of the ice volume are essential for modelling future glacier and runoff evolution. Wrong estimations of the total ice volume might even lead to deviations of the predicted general runoff trend.

## 2.1 Introduction

The demand for renewable energy is rising, especially when considering the declining confidence in nuclear power and the ascending greenhouse gas emissions (Bundesamt für Energie, 2011a). Particularly in alpine regions with sufficient amounts of precipitation, hydropower is one of the

most efficient and appropriate energy sources (Bundesamt für Energie, 2011b). In many high-mountain basins the water supply to hydropower reservoirs primarily consists of melt providing considerable amounts of water even in summer, when precipitation events are rare (Verbunt et al., 2003; Hock et al., 2005). Glaciers act as large freshwater reservoirs accumulating snow during the cold season and releasing the water accumulated as snow and ice during summer. This leads to sustainable differences in the runoff regime of glacierized basins compared to non-glacierized ones (e.g. Chen and Ohmura, 1990). However, the projected climate change and the associated glacier retreat entail the potential risk of serious diminution of the glacial induced water supply (Braun et al., 2000; Huss et al., 2008b; Farinotti et al., 2012).
In recent years, different studies examined the impact of climate change on runoff projections for high-alpine basins (Braun et al., 2000; Verbunt et al., 2003; Horton et al., 2006; Schaefli et al., 2007; Huss et al., 2008b; Farinotti et al., 2012; Uhlmann et al., 2013). Highly glacierized catchments require appropriate modelling of glacial processes including mass balance modelling (Klok and Oerlemans, 2002; Pellicciotti et al., 2005; Huss et al., 2008b) and adaptation of the glacier surface geometry (Vieli et al., 1997; Schneeberger et al., 2003; Huss et al., 2010; Jouvet et al., 2011). The initial ice volume distribution forms the basis for the determination of the glacier and runoff evolution of glacierized catchments. In order to deal with difficulties arising from the scarce or no data availability of the glacier bed, ice-thickness estimation approaches (e.g. Farinotti et al., 2009b; Fischer, 2009; Paul and Linsbauer, 2012) have been developed.
This study focuses on the determination of the glacier bed topography in the Mauvoisin region and the impact of the initial ice volume distribution on runoff projections of high-mountain catchments until 2100. A dense network of helicopter- and ground-based ground penetrating radar (GPR) measurements served as data basis for the determination of the ice-thickness distribution. The ice-thickness measurements were combined with an ice-thickness estimation approach in order to determine the glacier bed topography in the study area as accurately as possible (Sect. 2.3). Integrating the newly acquired knowledge about the ice volume distribution, the Glacier Evolution and Runoff Model (GERM, Huss et al., 2008b; Farinotti et al., 2012) forced by most recent climate scenarios (Bosshard et al., 2011) was applied to derive glacier evolution and runoff projections until 2100 for the region (Sect. 2.4). The model approach and the sensitivity of the model parameters have been tested in the study of Farinotti et al. (2012). In the scope of this study, the impact of uncertain ice-thickness estimations, due to a lack of ice-thickness measurements or the usage of inappropriate ice-thickness estimation methods, on runoff projections was analysed (Sect. 2.5). Uniform ice-thickness distribution, commonly used in macro-scale hydrological models, and more sophisticated results obtained from an ice-thickness estimation method (Farinotti et al., 2009b) deriving the distribution according to the surface topography were considered. Furthermore, the effect of over- or underestimation of the total ice volume was investigated. The main part of the article is divided in three separate sections about (1) the ice-thickness distribution, (2) the glacio-hydrological modelling, and (3) the ice volume sensitivity analysis whereby each section contains the corresponding methods and results.

## 2.2 Study site and data

The Mauvoisin area is situated in the south-western part of the Valais Alps, Switzerland (Fig. 2.1). The catchment extends over an area of 150 $km^2$, with 63 $km^2$ covered by glaciers in 2009, accommodating five larger glaciers (5–18 $km^2$) and several smaller glaciers (<5 $km^2$).

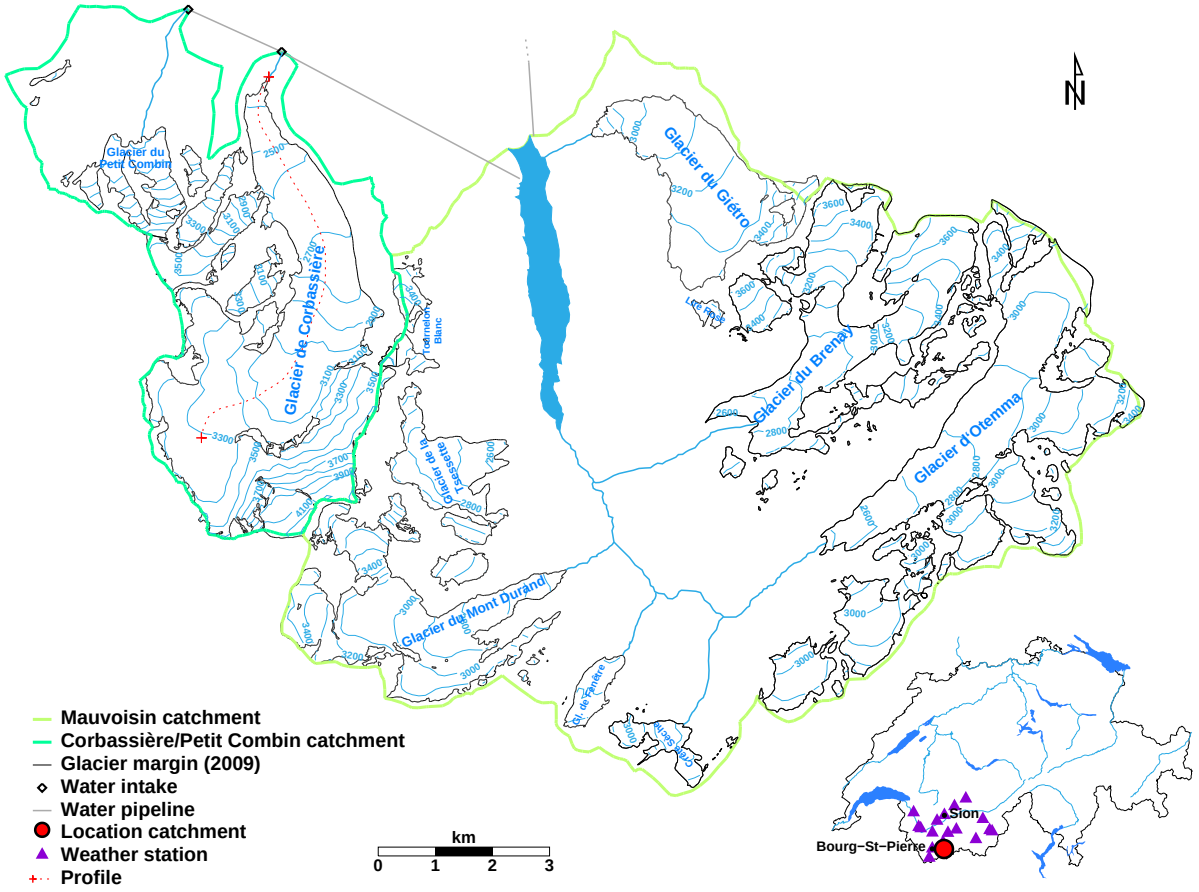


Figure 2.1: Overview of the Mauvoisin region. The inset on the bottom right shows the location of the catchment within Switzerland and the weather stations used in this study. The red dashed line refers to the profile of Fig. 2.11.

Due to the northwest orientation of the valley axis, the glaciers show exposures from southwest via north to east. They range in altitude from 2200 to 4300 m a.s.l. (Tab. 2.1).

The climate in the Mauvoisin region is characterized by mean precipitation amounts of about 1600 mm $a^{-1}$ and a mean annual temperature of $-3.5\,^{\circ}C$.

The transient modelling of glacier and runoff evolution in the past and future requires a wide range of different data sets. Past temperature and precipitation time series as well as projections for the future climate are used to force the model (see Sect. 2.4.1). Direct mass balance measurements, decadal ice volume changes derived from topographic maps and areal photographs as well as runoff measurements are used for model calibration (Tab. 2.2). Due to long-term efforts, annual mass balance measurements are available since 1966 for Glacier du Giétro and since 1996 for Glacier de Corbassière (Bauder, 2003; Bauder et al., 2007). Digital elevation models (DEMs) of the glacier surface are available for the years 1934, 1983 and 2009 for all glaciers in the catchment. Additional DEMs of the years 1997/1998 and 2003 exist for Glacier de Corbassière and Glacier du Giétro. DEMs of the year 1934 are based on topographic maps, whereas the others are derived by photogrammetrical analysis of areal photographs. An overview on the used data sets is shown in Table 2.2.

Hydrometric data are available from the hydropower company Mauvoisin since 1982. The data includes water level variations of the Mauvoisin reservoir, its outflow and the input of the water conducting pipelines on the left and right hand side (Fig. 2.1). Inflow and lake level

Table 2.1: Area, ice volume, altitudinal range and main exposition of the glaciers in the Mauvoisin region. Data refer to 2009.

| Glacier | Area $km^2$ | Volume $km^3$ | Alt. range m a.s.l. | Expo |
|---|---|---|---|---|
| Corbassière | 18.26 | 1.379 | 2235–4315 | N |
| Otemma | 15.74 | 1.052 | 2465–3815 | SW |
| Brenay | 8.99 | 0.384 | 2575–3815 | SW |
| Mont Durand | 6.98 | 0.298 | 2360–4160 | NE |
| Giétro | 5.46 | 0.447 | 2620–3815 | NW |
| Tsessette | 3.05 | 0.076 | 2490–4025 | E |
| Petit Combin | 2.53 | 0.023 | 2665–3665 | N |
| Fenêtre | 0.67 | 0.014 | 2575–3150 | NE |
| Crête Sèche | 0.60 | 0.009 | 2645–3150 | NE |
| Tournelon Blanc | 0.39 | 0.004 | 3140–3690 | E |
| Lire Rose | 0.14 | 0.001 | 3095–3225 | SW |

Table 2.2: Availability of different data sets used for this study: mass balance measurements (MB), DEMs, and the length of GPR profiles. Numbers in brackets indicate the fraction of ground-based GPR profiles from the total length of helicopter- and ground-based GPR profiles for each glacier.

| | MB | DEMs | GPR |
|---|---|---|---|
| Corbassière | 1996–2009 | 1934, 1985, 1997, 2003, 2009 | 34 (9) km |
| Giétro | 1966–2009 | 1934, 1983, 1998, 2003, 2009 | 17 (6) km |
| Brenay | – | 1934, 1983, 2009 | 8 km |
| Otemma | – | 1934, 1983, 2009 | 15 km |
| M. Durand | – | 1934, 1983, 2009 | 8 km |
| small gl. | – | 1934, 1983, 2009 | – |

measurements have monthly resolution for the period 1982 to 2000 and daily resolution since 2000. According to the available runoff data, we divided the basin into two sub-catchments, the *Mauvoisin catchment* which correspond to the natural catchment of the reservoir and the *Corbassière/Petit Combin catchment* which represents the area in the west including Glacier de Corbassière and Glacier du Petit Combin (Fig. 2.1). The runoff time series of the Mauvoisin catchment were generated by subtracting the inflow from the two pipelines and the outflow of the reservoir from the lake level changes.

## 2.3 Ice-thickness distribution

### 2.3.1 GPR measurements

In spring 2011, helicopter-based GPR surveys were carried out on the five largest glaciers in the Mauvoisin region (see Table 2.2). 122 km of GPR profiles were recorded whereof 55 % showed clearly detectable reflections, such that they could be incorporated in the ice volume calculation. The data were acquired by the commercial company *Radar Systemtechnik RST GmbH* (Salem, Germany). They employed an acquisition unit operating in a gated stepped mode using frequencies between 50 and 150 MHz (Radar Systemtechnik GmbH, 2012). Additionally, ground-based GPR measurements from previous field campaigns of the years 1988/1998 and 1997 on Glacier de Corbassière and Glacier du Giétro, respectively, were included (Fig. 2.2, VAW 1998).

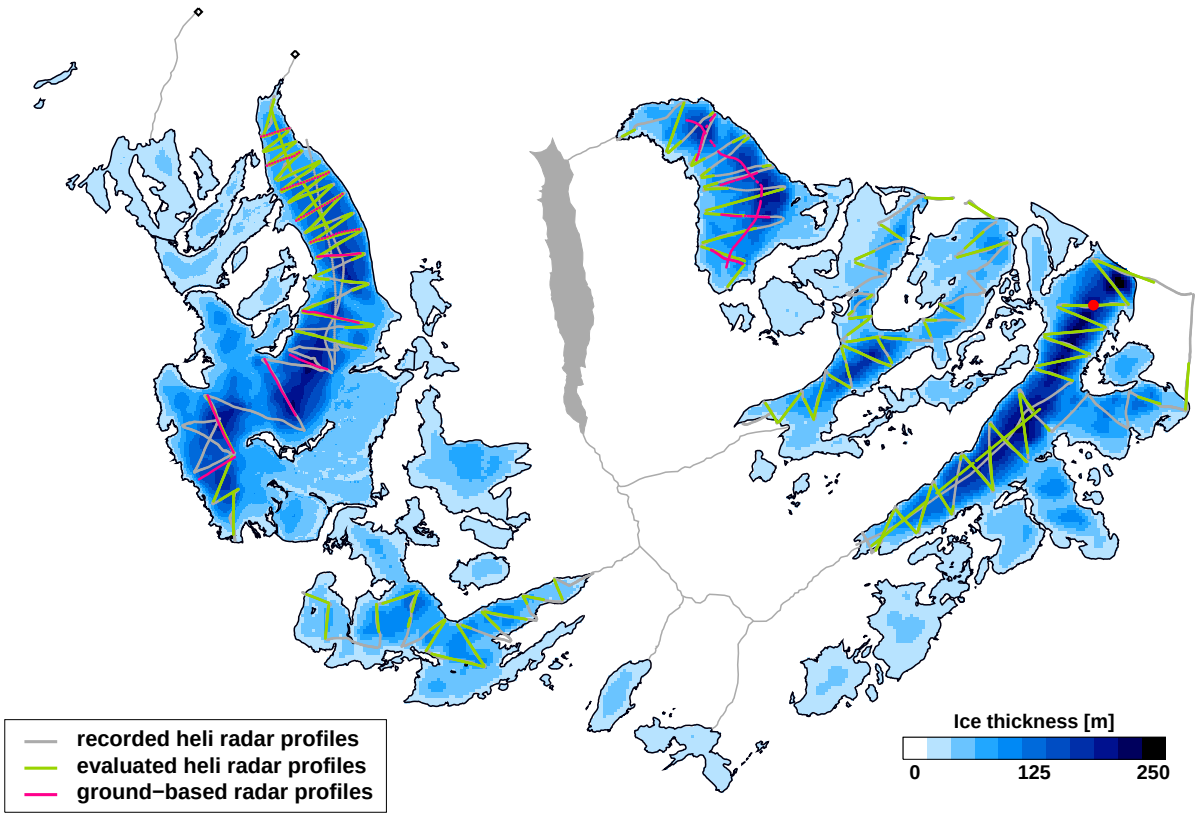


Figure 2.2: Ice-thickness distribution in the Mauvoisin region derived by all available ice-thickness measurements. Glacier outlines refer to 2009. The grey lines show the recorded helicopter-based GPR profiles, the green lines the finally evaluated profiles and the red lines the ground-based GPR profiles from previous field campaigns. The red dot refers to the GPR section shown in Fig. 2.3.

#### GPR processing

Visualization of the bedrock topography in the GPR sections required several processing steps to be applied. The helicopter-borne GPR data were acquired more or less continuously during the flights. In a first step, the positions of the GPR signals of the different traces were projected

on straight profiles which is required for the further processing of the GPR data. In order to remove the inherent system ringing of GPR acquisition systems a singular value decomposition based on multichannel filters has been performed. In a next step, a bandpass filter was applied, which removed signal portions outside of the frequency band radiated by the GPR transmitter antenna. Then, the reflected signals from the glacier surface had to be identified in the GPR sections, which allowed static corrections to be applied. A further critical processing step included application of gain functions for enhancing small amplitudes at later times in the radargrams (e.g. bedrock reflections). The signal-to-noise ratio was further improved by defining discrete bins along the profiles and stacking the traces contained in each bin. Finally, a Kirchhoff Migration was applied for removing artifacts produced by point scatterers (e.g. large boulders) and to correctly position the reflectors in the individual sections. Figure 2.3 shows a finally processed section across the Glacier d'Otemma. The bedrock reflection is clearly visible and reaches its maximum depth of about 250 m at a horizontal distance of 550 m.

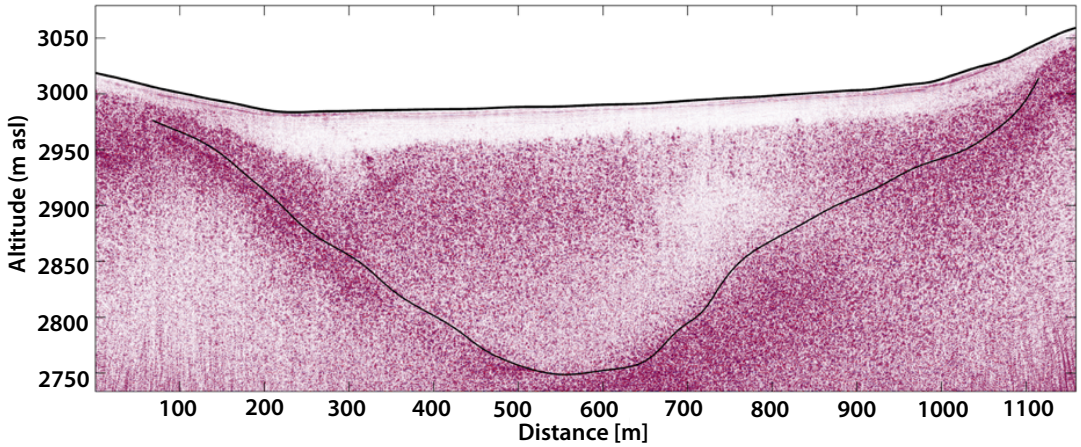


Figure 2.3: Processed GPR section across Glacier d'Otemma. Its position is indicated in Fig. 2.2.

### Uncertainties of GPR measurements

Uncertainties of the ice-thickness measurements origin from different sources of error. The main uncertainty arises due to blurry reflection horizons. Always the upper boundary of the reflection band was picked. By the identification of the bed reflections, care was taken to ensure that no sharp edges of the bed topography result. The uncertainty of this source of error can be assigned to $\pm 5$ m on average. In isolated areas uncertainties of up to $\pm 15$ m can occur due to blurry reflection. Another source of error are uncertainties about the propagation velocity of the electromagnetic wave. The velocity is well known and therefore the effect on the uncertainty of the ice-thickness is negligible small. Further uncertainties are introduced by the projection of the GPR signals on two dimensional profile sections. The uncertainties associated with this kind of error are spatial highly variable and are difficult to quantify. Hence, this error was not included in the uncertainty analysis. According to these considerations, an overall uncertainty of $\pm 5$ m was determined for the GPR measurements.
In order to verify the accuracy of the GPR profiles, a comparison between helicopter- and ground-based GPR measurements was performed. The helicopter-based GPR profiles were arranged in a manner allowing a comparison to ground-based measurements. As shown by

Figure 2.4 the ground-based agree well with helicopter-based GPR measurements. Remaining differences in the ice-thickness are mainly due to slight deviations in the projections of the GPR profiles.

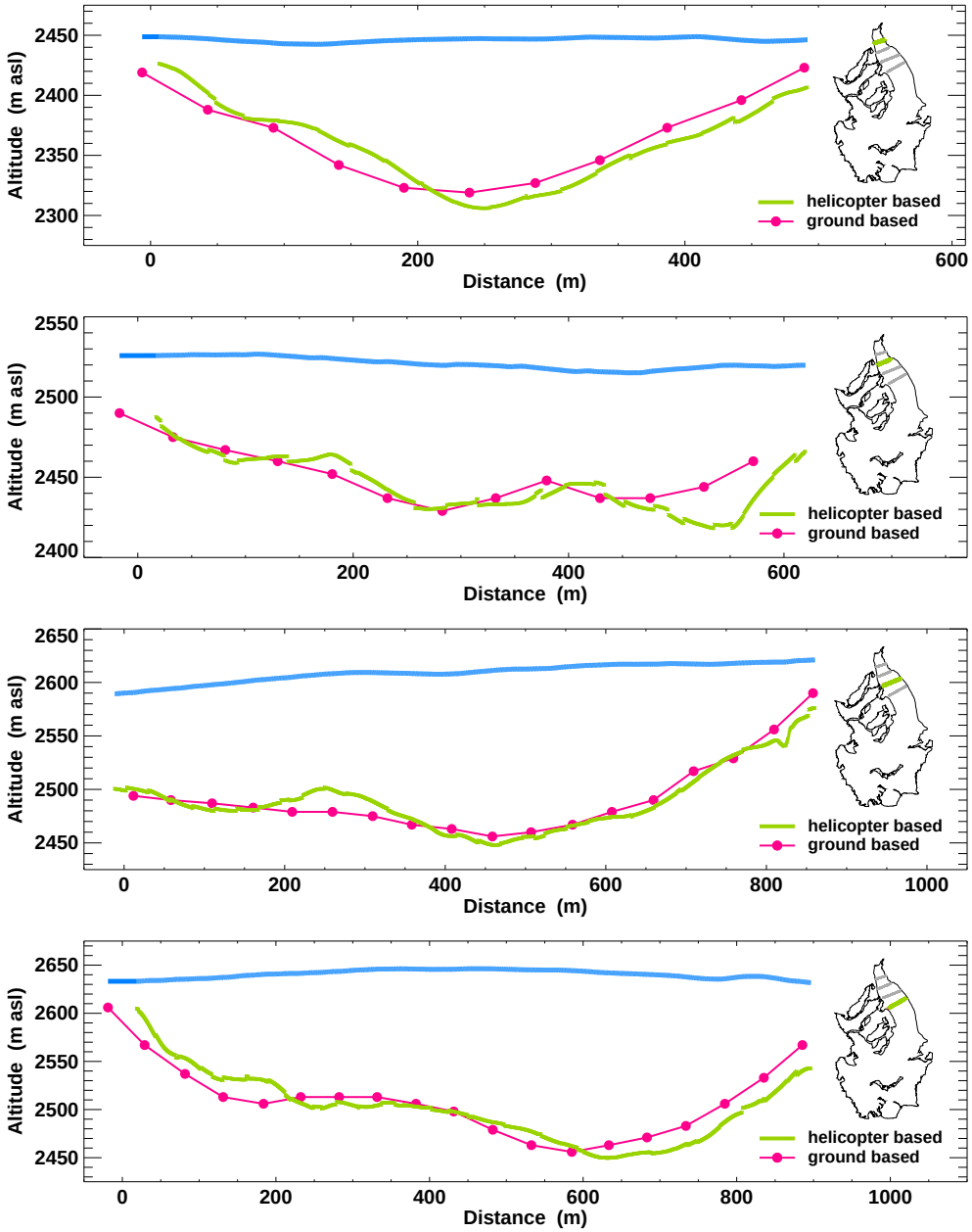


Figure 2.4: Comparison of ground-based and helicopter-based GPR profiles. Four GPR profiles of the lower part of Glacier de Corbassière were selected.

### 2.3.2 Ice-thickness estimation

Since the GPR profiles covered only a relatively small portion of the glacierized area, an extrapolation procedure was required for obtaining estimates over the entire area of interest. The literature describes different ice-thickness estimation approaches of various complexity (e.g. Farinotti et al., 2009b; Fischer, 2009; Paul and Linsbauer, 2012). All of them combine

Table 2.3: Area, maximal ($H_{max}$) and mean ($H_{avg}$) ice thickness, ice volume of (1) ($V_{(1)}$) and standard deviation, ice volume of (5) ($V_{(5)}$), the relative ice volume difference between $V_{(1)}$ and $V_{(5)}$ ($V_{(5:1)}$), and the calibrated apparent mass balance gradients for the ablation ($d\tilde{b}/dz_{abl}$) and accumulation zone ($d\tilde{b}/dz_{acc}$) of the Mauvoisin region.

| Glacier | Area [$km^2$] | $H_{max}$ [m] | $H_{avg}$ [m] | $V_{(1)}$ [$km^3$] | $V_{(5)}$ [$km^3$] | $V_{(5:1)}$ [%] | $d\tilde{b}/dz_{abl}$ [m/100m] | $d\tilde{b}/dz_{acc}$ [m/100m] |
|---|---|---|---|---|---|---|---|---|
| Corbassière | 18.3 | 238 | 76 | $1.38 \pm 0.09$ | 1.96 | +42 | 0.55 | 0.14 |
| Otemma | 15.7 | 291 | 67 | $1.05 \pm 0.08$ | 1.42 | +35 | 0.68 | 0.27 |
| Brenay | 9.0 | 212 | 43 | $0.38 \pm 0.04$ | 0.61 | +61 | 0.66 | 0.38 |
| Mont Durand | 7.0 | 144 | 43 | $0.30 \pm 0.03$ | 0.54 | +80 | 0.59 | 0.65 |
| Giétro | 5.5 | 230 | 82 | $0.45 \pm 0.03$ | 0.42 | -7 | 0.81 | 0.70 |
| small glaciers | 7.3 | 83 | 19 | $0.13 \pm 0.03$ | 0.08 | -38 | 0.66 | 0.43 |
| Mauvoisin | 62.8 | 291 | 59 | $3.69 \pm 0.31$ | 5.03 | +36 | 0.66 | 0.43 |

ice flow mechanics with the information about the surface topography for estimating the depth of the glacier bed.

In this study we applied the Ice-Thickness Estimation Method (ITEM) of Farinotti et al. (2009b). ITEM derives the ice-thickness distribution by calculating the ice flow and ensuring mass continuity. Two gradients for the so called apparent mass balance (i.e. the difference between the actual mass balance and the rate of ice-thickness change), one for the ablation and one for the accumulation zone, have to be assumed. The ice-thickness is derived from inverting Glen's flow law (Glen, 1955). A correction factor $c$ accounts for the valley shape, basal sliding and uncertainties in the chosen flow parameters. This factor has to be calibrated by ice-thickness measurements in order to maximize agreement between GPR measurements and calculated bedrock or has to be estimated from other glaciers.

We have used our GPR measurements to identify suitable correction factors for each profile. In between the profiles, the correction factors were linearly interpolated. On glaciers, where no GPR data were available, a mean correction factor was used. Gradients of the apparent mass balance were derived by the results of the mass balance model and the observed ice-thickness changes (Tab. 2.3).

By interpolation of the GPR profiles uncertainties are introduced in the ice volume estimation. In order to determine the magnitude of this kind of error, the ice-thickness estimation model was run multiple times for a different number of GPR profiles. By each model run a GPR profile was added to the set of ice-thickness measurements leading to a continuous increase in the accuracy of the ice volume estimation. By including the last profiles to the interpolation, the ice volume uncertainty approached to a level of about 1 %. Hence, the uncertainty introduced by the interpolation method is small for glaciers with a comprehensive set of ice-thickness measurements. The uncertainty of the ice volume calculation of glaciers without ice-thickness measurements was assessed taking the performance of the uncalibrated ITEM into account. Uncertainties of the ice volume calculation are shown in Table 2.3.

### 2.3.3 Results

Based on all available ice-thickness measurements a total ice volume of $3.69 \pm 0.31\,km^3$ was determined for the Mauvoisin region for the year 2009 (Tab. 2.3). Glacier de Corbassière is the largest glacier in the area with an ice volume of $1.38 \pm 0.09\,km^3$. Glacier d'Otemma shows a slightly smaller ice volume of $1.05 \pm 0.08\,km^3$. The three other larger glaciers, Glacier du Brenay, Glacier du Mont Durand, and Glacier du Giétro, have clearly lower ice volumes ranging between $0.30 \pm 0.03$ and $0.45 \pm 0.03\,km^3$. All smaller glaciers together account for $0.13 \pm 0.03\,km^3$ corresponding to approximately 4 % of the total ice volume. The largest ice-thickness (291 m) was found on Glacier d'Otemma (Tab. 2.3, Fig. 2.2). The maximum ice-thickness of Glacier de Corbassière is 238 m. Glacier du Brenay and Glacier du Giétro have maximal ice-thicknesses of around 220 m. In comparison, Glacier du Mont Durand shows a lower maximal ice-thickness of 144 m.

## 2.4 Glacier evolution and runoff modelling

### 2.4.1 Glacio-hydrological model

For glacier and runoff projections the glacio-hydrological model GERM was applied (Huss et al., 2008b; Farinotti et al., 2012). The model is fully distributed and consists of five different modules dealing with accumulation and ablation processes, glacier evolution, evaporation and runoff routing. The model was run on a daily basis for the time period 1900 to 2100 with a spatial resolution of 50 m and 25 m for the Mauvoisin and the Corbassière/Petit Combin catchment, respectively. Model and applications to alpine catchments are described by Huss et al. (2008b) and Farinotti et al. (2012) in more detail.

The mass balance model is based on a temperature-index melt model according to the approach by Hock (1999). It calculates the melt on a linear relationship between ablation and air temperature and includes the effect of potential solar radiation, thus accounting for the variability in slope, aspect and topographic shading. The local melt rate M is calculated in daily resolution by:

$$M = \begin{cases} (F_M + r_{ice/snow} I)T & : \quad T > 0\,^\circ C \\ 0 & : \quad T \leq 0\,^\circ C \end{cases} \tag{2.1}$$

where $F_M$ is the melt factor, $r_{ice/snow}$ the radiation factors for ice and snow, respectively, $I$ the potential solar radiation, and $T$ the mean daily air temperature. Below 0 °C no melting occurs. The accumulation model interpolates the amount of precipitation at the reference location to any location in the catchment on the basis of a calibrated precipitation gradient $dP/dz$ and a precipitation correction factor $c_{prec}$. Linear transition within a temperature range of 0.5 - 2.5 °C is used in order to distinguish between snow and rainfall. Further, a spatial depending snow distribution factor, which is constant over time, is implemented and accounts for snow transport processes through wind or gravity (e.g. avalanches).

Glacier surface is updated according to the so called *dh-parameterisation* (Huss et al., 2010). This method relies on the fact, that ice-thickness changes across a longitudinal profile of a glacier show a typical pattern which is approximately constant over time (Jóhannesson et al., 1989). In the parameterisation, the annual ice volume change computed by the mass balance model is distributed over the glacier surface according to a predefined pattern. Thereby, the pattern is obtained analysing historic glacier changes in the region of interest.

The runoff routing model consists of three different reservoirs: an interception, a fast and a slow one. In first instance, the water (sum of liquid precipitation and melt) infiltrates in the *interception reservoir* until it is filled. Afterwards the water is distributed in the *fast* and the *slow reservoir*. The filling rate depends thereby on the actual filling level of the slow reservoir. The fast reservoir indicates the near-surface, fast responding runoff, the slow one the runoff from deeper layers retaining water over a longer period. In case of a snow cover, there is a fourth *snow reservoir*. Part of the outflow from the snow reservoir infiltrates in the soil, the other one contributes directly to runoff. The total runoff is computed by adding the discharge of the slow, the fast and the direct runoff from the snow reservoir. The water loss of the interception reservoir is only controlled by evaporation. The individual reservoirs act as so called *linear reservoirs* where the runoff volume is proportional to the actual filling level of the reservoir. The model distinguishes between five different surface types: ice, snow, rock, low (meadow) and high vegetation (forest). The size of the reservoirs and the corresponding retention constant are dependent on the surface type. For further details on the GERM model, the reader is referred to Farinotti et al. (2012).

### Model forcing

The model is forced with continuous temperature and precipitation time series (1900–2100) with daily evolution. In order to reconstruct the past climate conditions (1900–2009) in the Mauvoisin area, regional temperature and precipitation data from weather stations in the vicinity of the study site are taken into account. Monthly temperature values between 1900 and 2009 were obtained by inverse-distance weighting of the homogenized climate time series of 12 different weather stations maintained by MeteoSwiss (Begert et al., 2005). In order to get temperature time series with daily resolution, daily fluctuations of the weather station in Sion were superimposed on the monthly values. Temperature lapse rates were computed by using data of weather stations closer than 50 km to the study area (Fig. 2.1). The homogenized temperature time series were shifted to the mean altitude of the investigated catchment by using the temperature lapse rate. For precipitation, the time series of the weather station of Bourg-St-Pierre were chosen due to the vicinity to the study site and the long record reaching back to 1900. These daily precipitation time series were scaled in order to match the monthly precipitation values given by the PRISM data set (Schwarb et al., 2001). The data set provides mean monthly precipitation sums for the Swiss Alps on a grid with 2 km resolution and the period 1971–1990. Precipitation lapse rate is determined during the calibration procedure by using the mass balance data. Temperature and precipitation lapse rate were kept constant over time. For further information about the generation of the climate time series of the past see Huss et al. (2008a).

Future climate time series (2010–2100) of the Mauvoisin region are based on scenarios developed in the framework of the European ENSEMBLES project (van der Linden and Mitchell, 2009). Regional climate scenarios of 10 different model chains (combination between general circulation models and regional climate models) based on emission scenario SRES A1B (IPCC, 2000) were used. The data were obtained from the *Center for Climate Systems Modeling (C2SM)* providing daily temperature and precipitation changes for two periods in the future (2021–2050; 2070–2099) in comparison to a period in the past (1980–2009) (CH2011, 2011; Bosshard et al., 2011).

In order to meet the model requirements of continuous climate time series the changes in temperature and precipitation between the different periods are assigned to the middle of each period and are linearly interpolated inbetween. An interannual variability is introduced

by superimposing daily fluctuations of the past on the interpolated time series. We followed the approach of Farinotti et al. (2012) and generated 10 different meteorological time series for each of the ten considered model chains. This results in 100 different time series of daily temperature and precipitation by which the model can be forced and allows to estimate a possible bandwidth for the climate evolution.
According to the climate projections provided by C2SM, the temperature in the Mauvoisin region (weather station at 1840 m a.s.l.) will increase by about $1.2 \pm 0.44\,^{\circ}\mathrm{C}$ on average until 2021-2050 and by about $3.4 \pm 0.63\,^{\circ}\mathrm{C}$ until 2070-2099 compared to the reference period. Mean precipitation will increase by about $1.4 \pm 2.4\,\%$ until the first period, but decreases by about $-2.8 \pm 3.8\,\%$ until the second period. These average changes in temperature and precipitation are not uniformly distributed over the year. Temperature is projected to increase most during summer and precipitation most in spring and autumn.

### Calibration

The calibration of the model parameters was performed by an automated multi-layer iterative procedure as described in Huss et al. (2008b) and Farinotti et al. (2012). In addition to hydrometric data, glacier volume changes and direct mass balance measurements were incorporated in the calibration procedure, which strongly reduce the uncertainties of the model parameters (Jost et al., 2012; Stahl et al., 2008). Optimum calibration is essential in order to ensure reliable glacier and runoff projections. Inappropriate parameter estimation or changes in parameter values in the future may lead to deviations from the predicted glacier and runoff evolution (see Discussion).
In a first step, the parameters of the melt and the accumulation module ($F_M$, $r_{ice/snow}$, $c_{prec}$, $dP/dz$) were calibrated by means of observed ice volume changes and mass balance measurements (Tab. 2.4). Melt and radiation factors were adjusted according to ice volume changes, precipitation gradient and precipitation correction factor according to mass balance measurements. The temperature gradient $dT/dz$ was previously determined by means of climate data from weather stations near the study site as described in Section 2.4.1. In a second step, the parameters of the runoff routing model were iteratively adjusted in order to ensure maximal agreement between observed and modelled runoff (Tab. 2.4). For validation the Nash-Sutcliffe criterion was calculated for daily, monthly, and annual runoff volumes (Nash and Sutcliffe, 1970). The model parameters were cross validated by calibrating the parameters for the period 1934–1983 and validating them for the period 1983–2009 and vice versa. The Nash-Sutcliffe criterion of the monthly runoff values is 0.93 and 0.94 for the Mauvoisin and the Corbassière/Petit Combin catchment, respectively, and of the daily runoff values 0.86 and 0.87, respectively. The bias between the modelled and the measured annual runoff is on average $+1.2\,\mathrm{mio\,m^3\,a^{-1}}$ (+0.6% or $+10.5\,\mathrm{mm\,a^{-1}}$) and $-0.5\,\mathrm{mio\,m^3\,a^{-1}}$ ($-0.9\,\%$ or $-14.5\,\mathrm{mm\,a^{-1}}$) for the Mauvoisin and the Corbassière/Petit Combin catchment, respectively. The parameters of the evaporation module are adopted from Huss et al. (2008b) and Farinotti et al. (2012).

## 2.4.2 Results

### Glacier evolution

Since the beginning of the 20th century, the glaciers in the Mauvoisin region have been in retreat. Between 1900 and 2009 the initial ice volume has decreased by 43 %, from $6.49\,\mathrm{km^3}$ to $3.69\,\mathrm{km^3}$. Almost half of this ice volume loss occurred during the past 30 years. Hence,

Table 2.4: Overview of the calibrated parameter sets of the melt, accumulation and runoff model shown for the two subcatchments Mauvoisin (Mauv) and Corbassière/Petit Combin (Corb). The retention constants for the fast reservoir and the maximal capacity of the slow and the fast reservoir depends on the surfacetype (ice, snow, rock, low and high vegetation, open water).

| Parameter | Explenation | Unit | Mauv | Corb |
|---|---|---|---|---|
| Melt model: | | | | |
| $F_M$ | Melt factor | $[10^{-4}\,\mathrm{m\,h^{-1}\,^\circ C^{-1}}]$ | 1.169 | 1.016 |
| $r_{ice}$ | Radiation factor for ice | $[10^{-6}\,\mathrm{m^3\,W^{-1}\,^\circ C^{-1}}]$ | 0.780 | 0.677 |
| $r_{snow}$ | Radiation factor for snow | $[10^{-6}\,\mathrm{m^3\,W^{-1}\,^\circ C^{-1}}]$ | 0.390 | 0.231 |
| $dT/dz$ | Temperature gradient | $[^\circ\mathrm{C\,m^{-1}}]$ | $-0.0053$ | $-0.0053$ |
| Accumulation model: | | | | |
| $dP/dz$ | Precipitation lapse rate | $[\%\mathrm{m^{-1}}]$ | 0.15 | 0.05 |
| $C_{prec}$ | Precipitation correction factor | [-] | 30.0 | $-10.0$ |
| Runoff model: | | | | |
| $k_{fast}$ | Retention constant fast reservoir | [d] | 2–30 | 2–30 |
| $k_{slow}$ | Retention constant slow reservoir | [d] | 50 | 50 |
| $k_{snow}$ | Retention constant snow reservoir | [d] | 5 | 5 |
| $V_{slow,max}$ | Max. capacity slow reservoir | [mm] | 200–5000 | 200–5000 |
| $V_{int,max}$ | Max. capacity interception reservoir | [mm] | 0–2.5 | 0–2.5 |

the retreat rate has nearly doubled since the beginning of the 1980s (Fig. 2.5). Similar mass balance rates could be also observed between 1943 and 1954. Only a short period of mass gain was observed between 1978 and 1983, when the ice volume increased by about 192 mio $\mathrm{m^3}$ corresponding to an increase of 3.6 % in total ice mass.

According to the applied model, all glaciers in the Mauvoisin region will severely retreat in the future independent of their size. By the end of the 21st century, the entire area will be nearly ice free. Only some ice patches above 3500 m a.s.l., with a total ice volume of 0.11 $\mathrm{km^3}$ ($0.08 \leftrightarrow 0.24\,\mathrm{km^3}$), are expected to remain. Small glaciers will vanish completely.

The amount of retreat of the glaciers in the Mauvoisin region is mainly controlled by the elevation of their accumulation area (Fig. 2.6). Small glaciers or parts of them below 3000 m a.s.l. are expected to disappear by 2020 as in case of Glacier de Fenêtre, Glacier de la Tsessette and, to some extent, also Glacier de Crête Sèche. Small glaciers situated at higher altitudes, such as Glacier de Tournelon Blanc, will persist longer.

Model results revealed that larger glaciers, especially those with large ice volumes and high-altitude accumulation areas, will retreat considerably slower than the smaller ones. Within the next few decades, the larger glaciers will be affected mainly by thinning. Only at a later stage (after 2050) the glaciers are expected to show significant areal wastage. Glacier d'Otemma shows a particularly fast retreat in contrast to the other larger glaciers in the area as indicated by our model. Already around 2070 Glacier d'Otemma will have almost entirely vanished except of some tiny ice patches in the uppermost part. The reason for the rapid retreat of the Glacier d'Otemma despite the large initial ice volume can be associated with its main basin

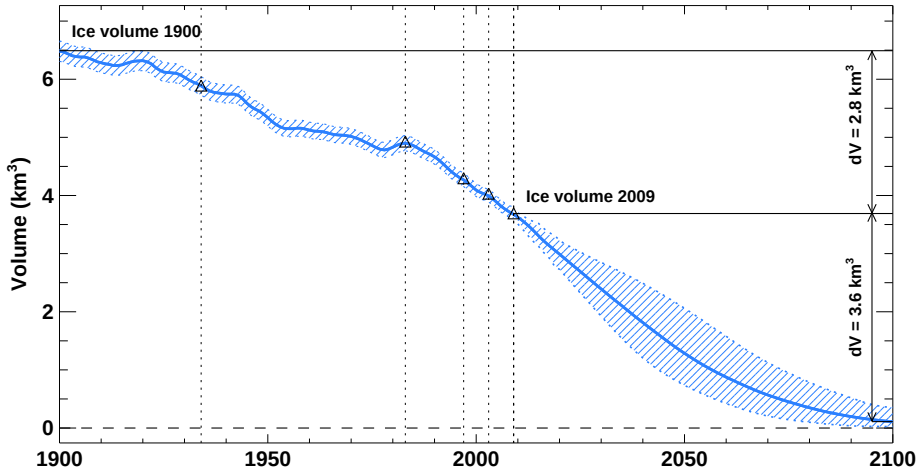


Figure 2.5: Ice volume evolution in the Mauvoisin region between 1900 and 2100. The hatched zone represents the 95 % confidence interval for the past given by the ice volume uncertainty and for the future given by the 100 different model runs. Black triangles and corresponding dotted lines show years in which a DEM is available.

restricted to altitudes below 3100 m a.s.l. In comparison, in 2070 Glacier de Corbassière will cover almost the half of its initial area because of considerable ice masses situated at altitudes above 4000 m a.s.l.

### Hydrology

According to our reconstruction, the annual runoff increased from 216 to 265 mio $m^3 a^{-1}$ (23 %) between 1900 and 2009, but this rise was not constant over time. In two successive periods from 1910 to 1945 and from 1975 to 1995 the annual runoff volume has increased by about 45 mio $m^3\,a^{-1}$ (∼20 %) and has reached maximal runoff of approximately 260 mio $m^3\,a^{-1}$. In between, the annual runoff volume dropped back to values of less than 220 mio $m^3\,a^{-1}$. These fluctuations can be correlated with the glacier evolution as well as with changes in temperature and precipitation (Fig. 2.7). In the next two decades, annual runoff is projected to increase to approximately 275 mio $m^3\,a^{-1}$ (+4 %). Afterwards, a continuous decline is expected until the end of the 21st century. Compared to the maximal runoff volume of 275 mio $m^3\,a^{-1}$ the annual runoff will drop about 25 % to 207 mio $m^3\,a^{-1}$ until 2100. In comparison to a previous study addressing nine selected catchments in the Swiss Alps (Farinotti et al., 2012), the future runoff evolution in the Mauvoisin catchment shows a similar evolution as other strongly glacierized catchments.

The changing climate and the associated glacier wastage will not only affect the amount of annual runoff, but also the individual runoff components, leading to significant changes in the runoff regime. At present, the runoff regime is dominated by ice and snow melt and shows a peak discharge in the months July and August (Fig. 2.8). Modelled runoff projections indicate that in future, the mean daily runoff in summer will strongly diminish, whereas during winter daily runoff will slightly enhance due to higher air temperatures. Currently, a maximum mean daily runoff of 28 $m^3\,s^{-1}$ is attained at the end of July, which will decrease to 18 $m^3\,s^{-1}$ until the year 2100. Beside the reduction of daily runoff, also a shift of peak runoff is expected. According to the model, maximal runoff values will occur one-and-a-half months earlier at the end of the 21st century compared to the reference period. This shift of the peak discharge

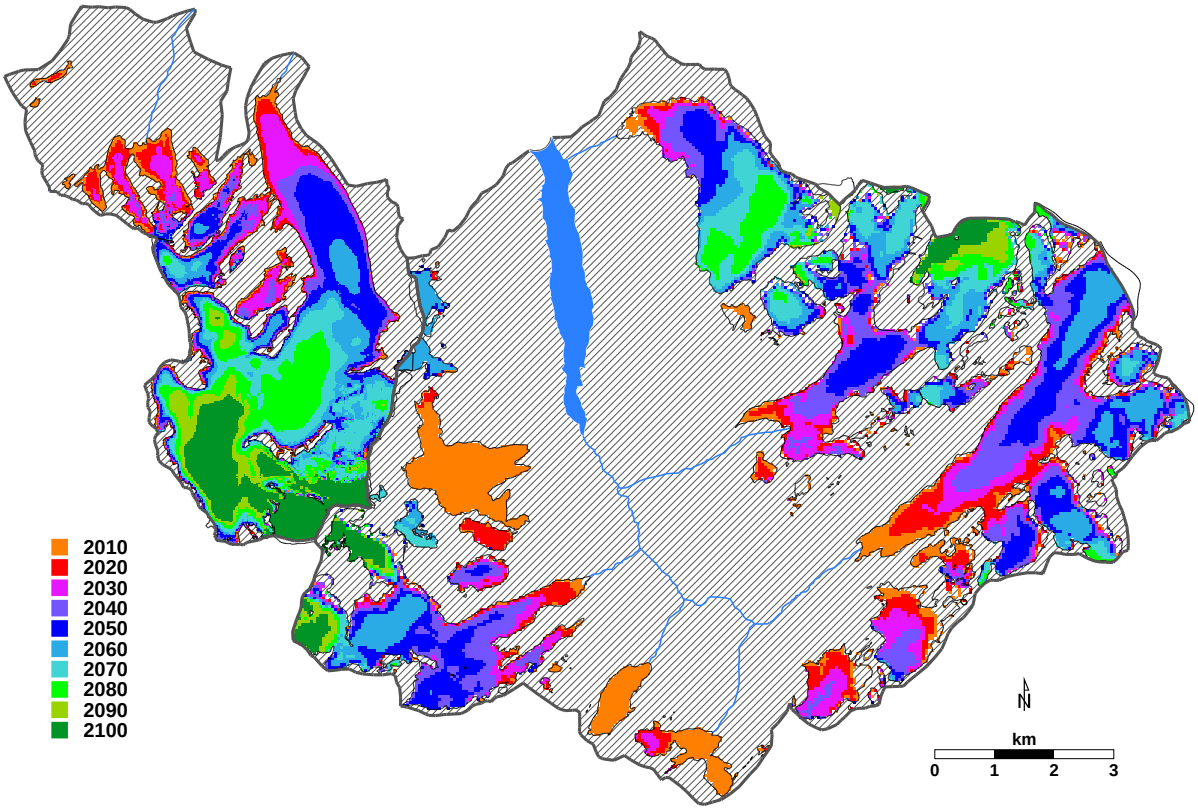


Figure 2.6: Projected glacier retreat in the Mauvoisin region until the end of the 21st century. Glacier area is shown in 10-yr steps. Hatched zones framed by gray thick lines represent the outlines of the two subcatchments Mauvoisin and Corbassière/Petit Combin.

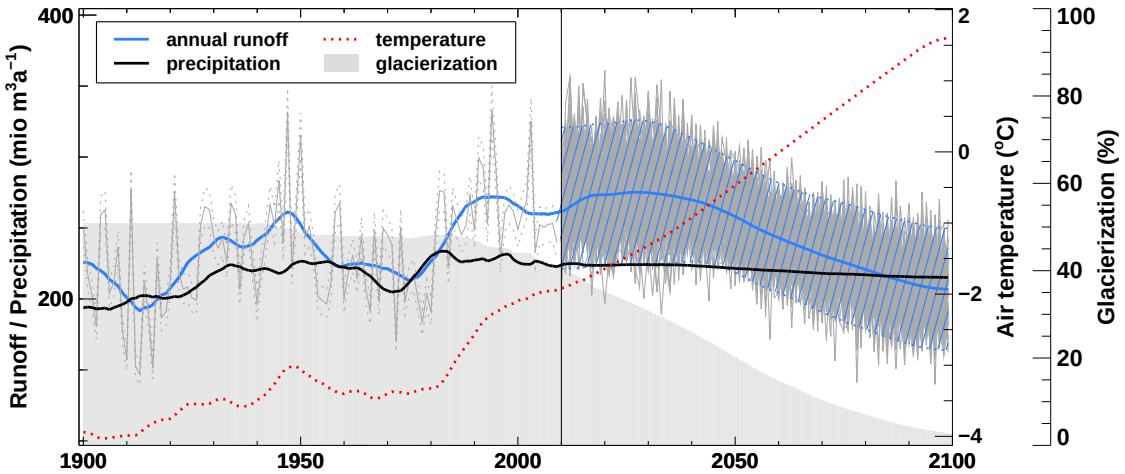


Figure 2.7: Evolution of annual runoff, precipitation, air temperature and glacierization in the Mauvoisin catchment. Bold lines represent running means, the thin gray line the effective evolution of the annual runoff. The blue hatched zone shows the 95% confidence interval of the annual runoff determined from multiple model runs. The grey dotted lines indicate the 95 % confidence interval of the effective annual runoff evolution in the past based on the bias between modelled and measured annual runoff. The gray shaded area refers to the percentage of the ice covered area in the catchment.

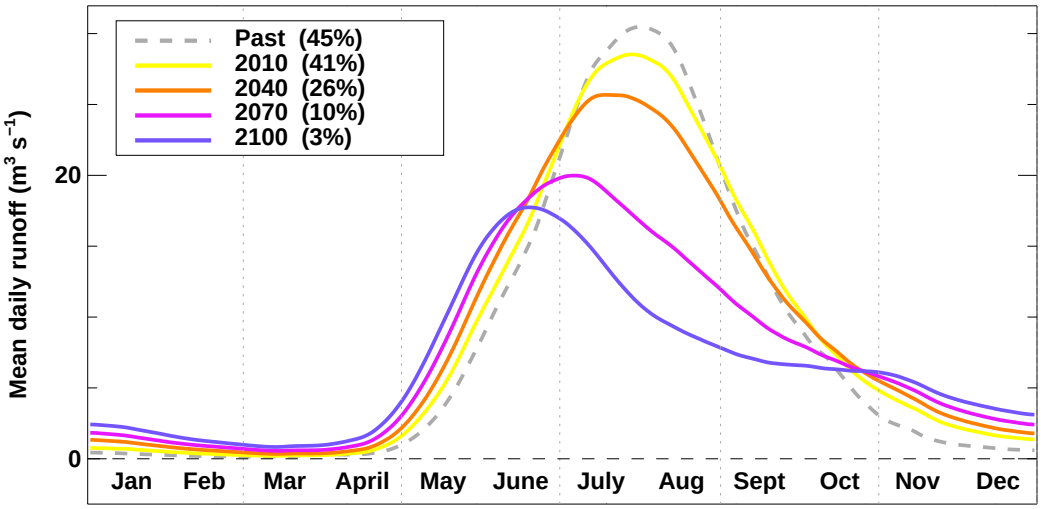


Figure 2.8: Evolution of the runoff regime in the Mauvoisin region for the reference period and four time snapshots in the future averaged over ±5 years. Numbers in brackets refer to the percentage of glacier cover.

from end of July to the mid of June results from the decrease of the runoff volumes in the months July to September by about 44 % compared to the reference period. Furthermore, the runoff projections indicate that daily runoff increases slightly earlier in spring compared to the present situation due to the earlier onset of the snow melt season. The time offset between the beginning of the melt season in the reference period and in 2100 is around three weeks. Similar changes in the runoff regimes of high-alpine basins in the future have been reported by other studies (Horton et al., 2006; Uhlmann et al., 2013).

The reason for these changes in the runoff regime becomes evident by considering the evolution of the different sources of water input to the runoff model with progressing climate change (Fig. 2.9). The model employed distinguishes between: liquid precipitation, snow melt, and ice melt. Firn is counted to ice melt. Between the sum of the three water input components (Fig. 2.9) and the runoff regime (Fig. 2.8) is a slight difference originating from runoff routing. During the reference period (1980-2009), snow melt is the main component and account for 60 % of the water input. At present, snow runoff contribution starts to increase mid of May and reaches a maximum at the beginning of July. The ice melt increases later in the season (at the beginning of June) and its maximum occurs around the end of July. Model projections show that maximum snow melt is shifted to the beginning of June and that the ice melt is reduced and its maximum shifted to mid of August by the end of the 21st century. Hence, the shift of the snow melt peak and the reduction of the ice melt lead to reduced runoff volumes in July and August as shown by the runoff regime evolution.

According to our model, ice melt will decrease about 74 % between 2010 and 2100 and will contribute only by 2 % to total runoff in the year 2100. The remaining runoff will originate in equal parts from snow melt (48 %) and liquid precipitation (50 %). Snow melt will experience a less pronounced decrease than ice melt. From 2010 to 2100 snow melt reduces about 11 %. The reduction of snow melt is caused by less solid precipitation due to the expected temperature rise and generally decreased precipitation amounts. In fact, total precipitation will reduce about 6 % until 2100 compared to the reference period (1980-2009). The results

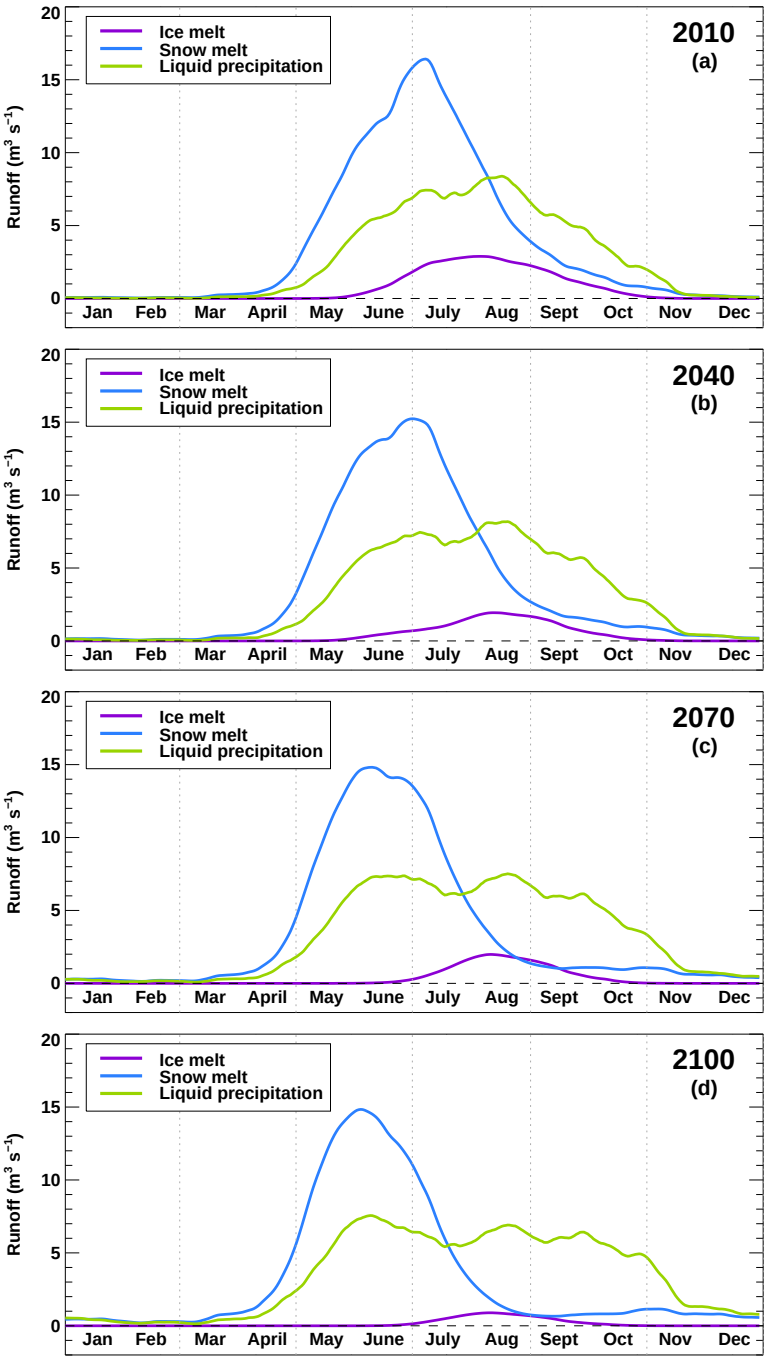


Figure 2.9: Evolution of the three components of the water input to the runoff routing model for the years 2010 (a), 2040 (b), 2070 (c), and 2100 (d). The values are averaged over ±5 years.

Table 2.5: Summary of the main results of this study. The evolution of the ice volume, the glacierized area, the annual runoff and the different components of water input to the runoff routing model (ice melt, snow melt, and liquid precipitation) is shown for the period 1920-2100 in 30-yr steps. Values are averaged over $\pm 5$ years.

| Quantity | Unit | 1920 | 1950 | 1980 | 2010 | 2040 | 2070 | 2100 |
|---|---|---|---|---|---|---|---|---|
| Ice volume | $km^3$ | 6.2 | 5.3 | 4.3 | 2.4 | 1.8 | 0.6 | 0.1 |
| Glacier area | $km^2$ | 75.9 | 72.7 | 71.7 | 61.6 | 38.6 | 15.5 | 4.2 |
| Annual runoff | $10^6\,m^3a^{-1}$ | 207 | 258 | 223 | 260 | 270 | 231 | 206 |
| Ice melt | $10^6\,m^3a^{-1}$ | 19 | 15 | 6 | 19 | 13 | 11 | 5 |
| Snow melt | $10^6\,m^3a^{-1}$ | 103 | 126 | 121 | 119 | 118 | 112 | 105 |
| Liquid precipitation | $10^6\,m^3a^{-1}$ | 51 | 66 | 61 | 85 | 96 | 103 | 109 |

of the runoff analysis are summarized in Table 2.5.

## 2.5 Ice volume sensitivity analysis

Extensive helicopter-borne GPR measurements allowed the ice-thickness distribution in the Mauvoisin area to be determined accurately. If such data sets are not available, simplified models need to be employed. By means of a sensitivity analysis we have quantified the influence of the initial ice-thickness distribution on glacier and runoff projections.
For that purpose, we considered five different ice-thickness distributions (Fig. 2.10).

1. Approach as described in Sect. 3.2. Case (1) refers to the reference ice-thickness distribution based on the measurements.

2. Same ice-thickness distribution pattern as (1) but scaled by +20 %. This case shows the influence of overestimated total ice volumes on runoff projections.

3. Same ice-thickness distribution pattern as (1) scaled by $-20$ %. Case (3) emphasizes the impact of underestimation of the total ice volume on the runoff evolution.

4. Uniform ice-thickness distribution with a mean ice-thickness calculated by the ice volume based on (1) for each glacier. This distribution is the most simple case and is used in most macro-scale hydrological models where ice volume is crudely processed (Fig. 2.10d).

5. Ice-thickness distribution calculated by the ITEM assuming a correction factor $c$ of 0.53 as used in the study by Farinotti et al. (2009a) for unmeasured glaciers. Apparent mass balance gradients are set to $0.9 \times 10^{-2}\,a^{-1}$ for the ablation zone and to $0.5 \times 10^{-2}\,a^{-1}$ for the accumulation zone. This method provides a spatial distribution pattern based on the glacier surface topography. Case (5) shows the performance of ITEM if no ice-thickness measurements are available (Fig. 2.10b).

When assuming a constant correction factor $c = 0.53$ (5), ITEM overestimates the total ice volume of the Mauvoisin region by about 36 % (Tab. 2.3). Especially, for Glacier du Brenay and

Glacier du Mont Durand the ice volume is overestimated by 61 and 80 %, respectively. Glacier du Giétro shows in case of $c = 0.53$ an exceptional small deviation of only $-7$ %. Glacier de Corbassière and Glacier d'Otemma show mainly in the lower area large ice-thickness deviations between the GPR and the ITEM based bed topography of up to 130 m (Figs. 2.10 and 2.11). Glacier du Brenay and Glacier du Mont Durand show deviations in the ice-thickness of the same order, but the largest deviations are located more in the center than on the lower part of the glacier.

### 2.5.1 Impact of initial ice volume distribution on runoff

The different ice volume distributions significantly affect the runoff projections. In case of the GPR derived ice volume (1) annual runoff will slightly increase (about 4 %) from 2010 until about 2030 to a maximal annual runoff volume of 275 mio $m^3\,a^{-1}$. Afterwards, the runoff volume starts to decrease gradually until 2100 (Fig. 2.12). Overestimation of the total ice volume of about 20 % (2) results in a pronounced increase of the annual runoff over a prolongated period of time compared to GPR derived runoff. Peak discharge will occur around 10 yr later with a volume of 279 mio $m^3\,a^{-1}$ (+1 %) compared to (1). Underestimation of the total ice volume (3) leads in the case of the Mauvoisin region to changes in the trend of the runoff evolution in the next decades. Instead of a further runoff increase, annual runoff continuously decreases until the end of the 21st century with general lower runoff volumes compared to GPR derived results. Neglecting a spatial ice volume distribution by assuming uniform ice-thickness distribution (4) leads to an overestimation of the runoff in the next two decades due to too large ice masses in low altitude. Maximal annual runoff will occur around 2020 with a peak discharge of 283 mio $m^3\,a^{-1}$ (3 %). In a later stage, the runoff of the uniform ice volume distribution aligns to the GPR derived runoff curve. The application of ITEM with the uncalibrated and fixed parameter set (5) overestimates the ice volume in the Mauvoisin region about 36 % which results in a similar runoff evolution as in case of the ice volume overestimated by 20 % (2). But, in Case (5) the annual runoff shows a sharper increase of 12 % between 2010 and 2040. A maximum peak runoff of 287 mio $m^3\,a^{-1}$ is expected in this case.

## 2.6 Discussion

The ice volume sensitivity study emphasizes the importance of an accurate ice volume determination for glacier and runoff projections. The incorporation of ice-thickness measurements in the ice volume calculation is crucial in order to receive reliable ice volumes and ice-thickness distributions. Inaccurate estimations of the total ice volume will cause deviations from the predicted general runoff trend. In case of the Mauvoisin region, it could be shown that an overestimated ice volume reveals a sharp runoff increase in the the next few decades, whereas estimations supported by measurements show almost no further increase in annual runoff. The ice-thickness distribution affects the runoff evolution as well, but not as pronounced as in case of an overestimated ice volume. A uniform ice volume distribution entails particularly in the next few decades an overestimation of runoff and is therefore less suitable for short- and mid-term projections. After major ice volume has melted, it only differs slightly from the GPR derived runoff evolution. In absence of ice-thickness measurements a mean parameter set has to be assumed carrying the potential of over- or underestimation of the true ice volume. In case mass balance measurements are available, mass balance gradients can be adjusted leading

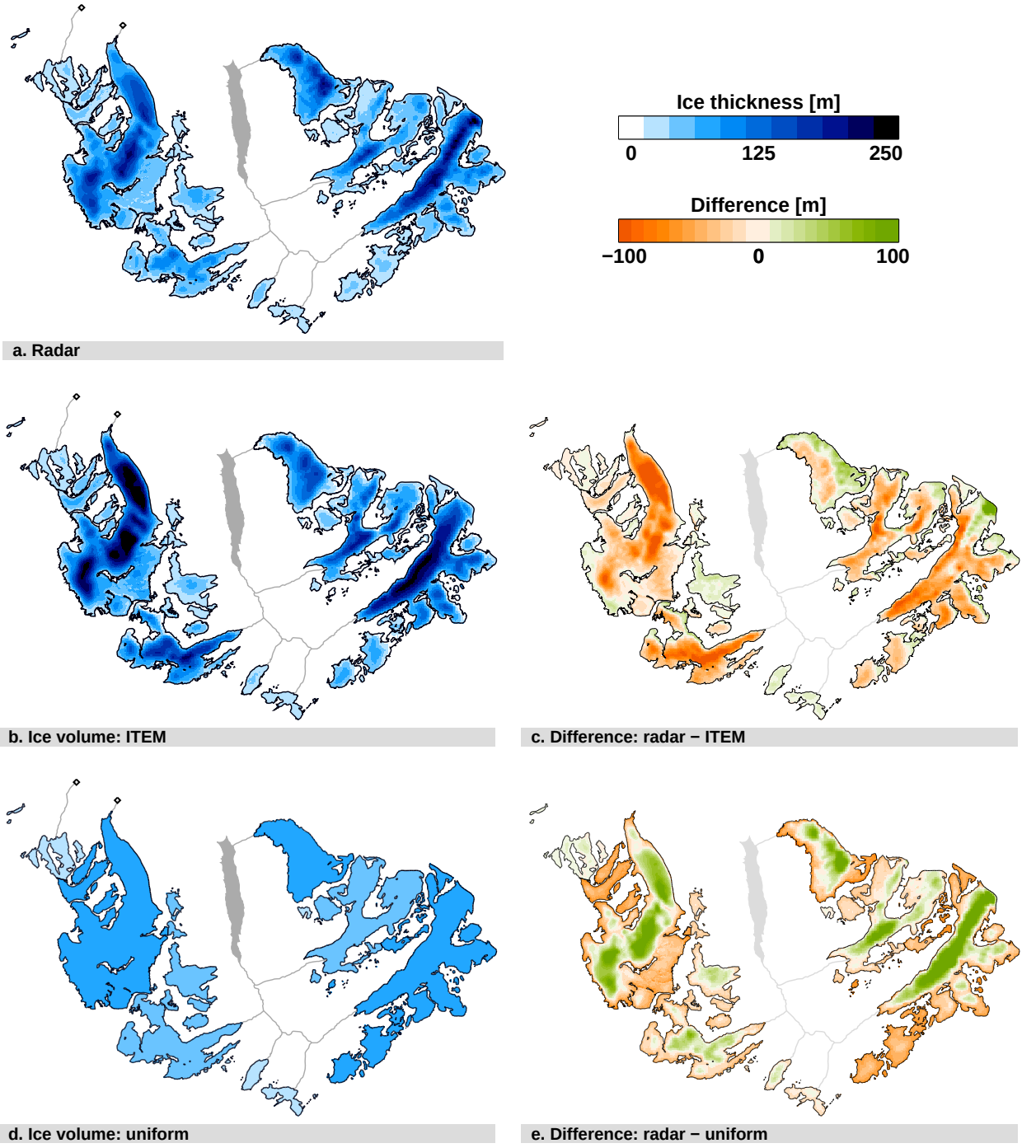


Figure 2.10: The different ice-thickness distributions: (a) the GPR based ice volume distribution, (b) the ice-thickness distribution derived by ITEM, and (d) the uniform ice-thickness distribution. The figures on the right side (c, e) refer to the ice-thickness difference to the reference distribution determined by measurements.

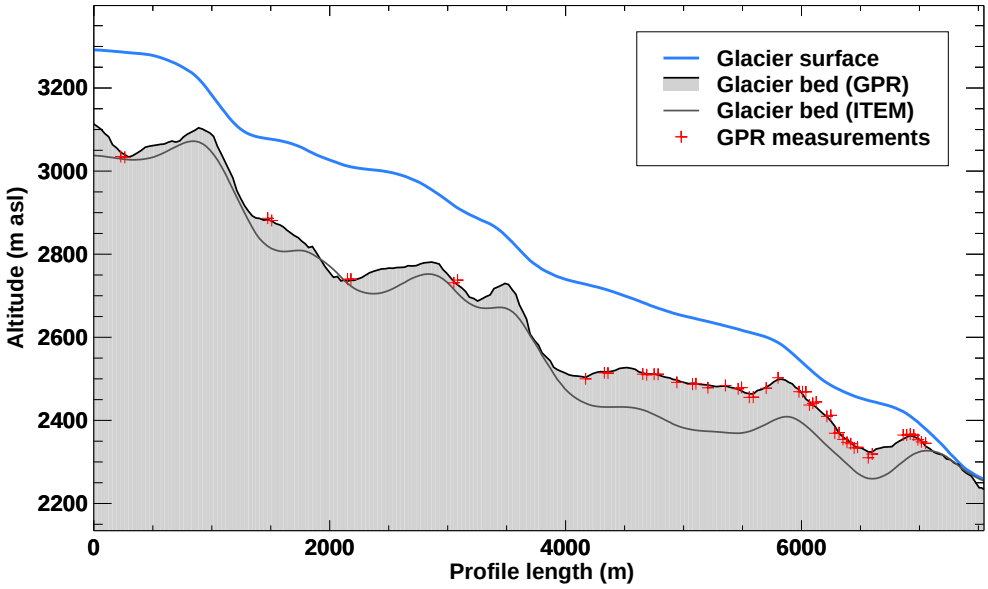


Figure 2.11: Longitudinal profile along the central flow line of Glacier de Corbassière (see Fig. 2.1). The thin black line refers to the glacier bed derived from the GPR measurements, the thin gray line to the bed computed by the ITEM and the blue line to the glacier surface. The red crosses mark the GPR based ice-thickness measurements.

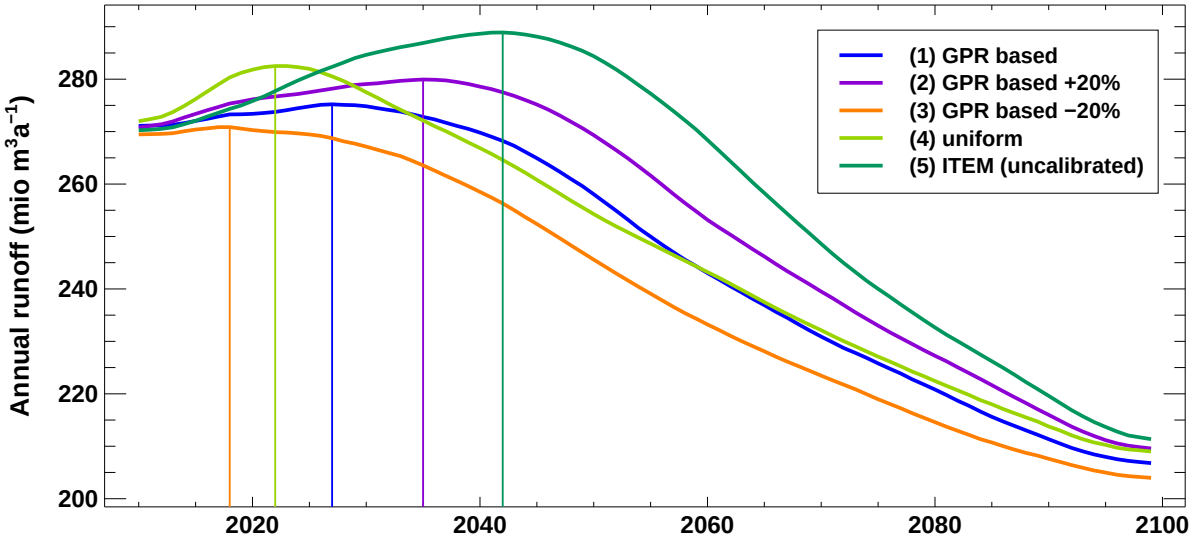


Figure 2.12: Runoff projections based on the different initial ice-thickness distributions. The numbers in brackets refer to the different initial ice volume distributions presented in Section 2.5.

to improvements in the ice volume estimation. Due to the high sensitivity of the ice volume estimation on the correction factor (Farinotti et al., 2009b), the use of an appropriate correction factor is of much higher importance compared to the mass balance gradients. Knowledge about the local ice-thickness enables the calibration of the correction factor resulting in a significantly increased accuracy of the ice volume estimation. New approaches are required for better assessing correction factors for individual glaciers if no ice-thickness measurements are available. Our results suggest that the incorporation of GPR based ice-thickness measurements is of high importance in order to provide reliable runoff projections especially for the next thirty to forty years when profound changes are expected.

Despite the high density of ice-thickness measurements and the application of an ice-thickness estimation method, the true bed topography is not fully known. Uncertainties arise due to uncertainties of the ice-thickness measurements and due to the interpolation method. Taking these two sources of error into account an overall uncertainty of $\pm 8\,\%$ was determined for the total ice volume. This uncertainty leads to the same alterations of the runoff projections as shown by the results of the sensitivity analysis for under- and overestimated ice volume (20 %), but less pronounced.

A simple approach to compute the glacier evolution is the Accumulation Area Ratio (AAR) method as used by several studies (e.g. Schaefli et al., 2007; Paul et al., 2007). This method updates the glacier surface according to the modelled accumulation area and a fixed accumulation area ratio assuming infinite ice volume. Moreover, no mass conservation is provided. Huss et al. (2008b) showed a poor performance of the AAR method compare to an approach with a transient glacier evolution model and an initial ice volume distribution. According to Huss et al. (2008b), the annual runoff volume is up to 30 % underestimated by the AAR approach which is clearly below the performance of all tested ice volume distributions.

The reliability and usefulness of the glacier evolution and runoff projections is also affected by uncertainties in the future climate evolution. The climate scenarios applied are based on the most recent climate study and incorporate different combinations of regional and general circulation models. However, only emission scenario SRES A1B (IPCC, 2007) was considered. Deviations from the chosen emission scenario might entail a different glacier evolution and consequently changes in the projected future runoff regime.

Uncertainties arise also from the chosen model approach. The prediction of the glacier evolution is determined on the basis of a temperature-index melt model in combination with an accumulation model. Due to the low data requirement of this approach, it is well suited for distributed modelling of entire catchments and available for future climate scenarios. But, temperature-index melt models act just as simplified approaches of the true surface energy balance and react only to changes in the temperature and precipitation field. Other factors, such as variations in incoming or outgoing radiation or changes in the wind field, are not incorporated and may lead to different results. In the 1940s, a rise in the global radiation led to higher melting rates compared with today's climate conditions despite of lower air temperatures (Huss et al., 2009b). Such variations of solar radiation are not captured by temperature-index melt models retaining a constant parameter set and might yield discrepancies between projected and real glacier evolution.

Furthermore, uncertainties about the model parameters have the potential to cause deviations from glacier and runoff projections. The study of Farinotti et al. (2012) reveals that runoff projections are particularly sensitive to changes in the temperature gradient and melt parameter values. The study shows that a reduction of the temperature lapse rate by 10 % yields a decrease of the mean annual runoff between 2010 and 2100 of about 25 % and that an increase of the melt parameters of 10 % lead to an increase of the mean annual runoff of 11 to 20 % in

the same period. The temperature distribution has a big impact on runoff projections because it controls the snow and ice melt and additionally also the phase of precipitation. Under- or overestimation of the total ice volumes leads to deviations in the mean glacier melt of the same order. In case of the ITEM-derived glacier bed topography, the total ice volume is overestimated by 36 % leading to a reduction of the mean glacier-induced runoff between 2010 and 2100 of about 31 %. This corresponds to a mean annual runoff reduction of about 4 % in the period 2010 to 2100, what is less than the effect of the temperature gradient and the melt parameters, because the ice volume affects the ice melt component only. But, the discrepancy between the two runoff evolutions is higher for individual years, as around 2050, where the annual runoff based on the ITEM-derived ice volume distribution is overestimated by about 10 %. For glacierized catchments the incorporation of glacier specific data for the calibration procedure is crucial in order to reduce the uncertainty of the model parameters and to provide reliable projections (Stahl et al., 2008; Jost et al., 2012). For this reason we are confident that the calibrated parameters are despite the simple calibration method appropriate for modelling the glacier and runoff evolution. Further improvements in the parameter estimation might be achieved by applying a more sophisticated optimization algorithm. But, uncertainty about the validity and potential variations of the parameters in the future will remain.

Enlargement of the debris covered area of a glacier might yield attenuation of the glacier retreat in future. Glacier d'Otemma and Glacier du Brenay show already an extended debris cover in the ablation zones. During the last decades, especially small glaciers in the Mauvoisin area have shown a strong increase in debris cover. Similar observations have been reported from other mountain regions (Kellerer-Pirklbauer, 2008; Popovnin and Rozova, 2002; Stokes et al., 2009). In contrast, an increase in dust cover reduces the albedo and leads to an intensification of the melt process (Oerlemans et al., 2009). Insufficient understanding of the processes yielding changes in debris or dust cover and lack of data inhibit the implementation of debris cover evolution in melt models (Reid and Brock, 2010).

Moreover, the glacier evolution also involves uncertainties arising from the accumulation model. The spatial distribution of precipitation and the distinction between liquid and solid precipitation is complex. Variable redistribution of snow by wind and avalanches further increases the complexity of the accumulation pattern (Lehning et al., 2008). The applied model includes a simplified snow redistribution approach but assumes constant snow redistribution patterns in time. Further effort is required to increase the accuracy in modelling the snow distribution on glaciers (Dadic et al., 2010).

Projections of the annual runoff volume and the runoff regime were compared to the results of the study by Schaefli et al. (2007) which investigated the influence of the climate change on the hydropower production in the Mauvoisin region by a more simplified approach. Our results show higher annual runoff volumes by the end of the 21st century compared to Schaefli et al. (2007). Changes in the daily runoff regime as the reduction of the peak discharge and the shift toward earlier in season are ascertained by both studies. However, a direct comparison is not possible, because (1) different climate scenarios were used, and (2) the investigated catchments differ in their extent.

## 2.7 Conclusions

In this study we combined results from extensive GPR measurements with an ice-thickness estimation approach (Farinotti et al., 2009b), for determining the present ice volume in the Mauvoisin area. A total ice volume of $3.69 \pm 0.31\,\mathrm{km}^3$ was calculated by including all available

measurements and a maximal ice-thickness of 291 m was found. The derived ice volume distribution served as input for a combined glacio-hydrological model (Huss et al., 2008b; Farinotti et al., 2012), by which glacier and runoff projections were determined. By means of a sensitivity analysis we could demonstrate that an under- or overestimation of the total ice volume may lead to severe distortions of the runoff projections and potentially even to deviations from the projected general runoff trend. Particularly for projections for the next 20 to 30 yr an accurate ice volume determination and an appropriate ice-thickness distribution is crucial. The study emphasizes the importance of the incorporation or GPR measurements in order to get reliable ice-thickness distributions. Including ice-thickness measurements clearly increases the accuracy of the ice volume estimation and hence, the runoff projections.
According to our model, the annual runoff will rise about 4 % to a maximum of 275 mio $m^3\,a^{-1}$ until around 2030 and will drop in the subsequent period to 207 mio $m^3\,a^{-1}$ by 2100. The runoff regime is expected to change from an ice-melt to a snow-melt dominated regime. Maximum mean daily runoff will decrease from 28 $m^3 s^{-1}$ to 18 $m^3\,s^{-1}$ from 2010 to 2100 and will occur one and a half month earlier by 2100 than in the reference period.
Application of helicopter-based radar measurements on further alpine catchments, will lead to a more profound knowledge about the ice volume and the ice-thickness distribution in the Alps. According to an improved knowledge about the ice volume distribution, glacio-hydrological projections will become more accurately. Progress in model approaches (e.g. knowledge of the long-term behavior of model parameters) and the development of improved climate scenarios may further reduce the uncertainty about the future evolution.

**Acknowledgements**

Our particular thanks go to the *Forces Motrices de Mauvoisin SA* which has enabled and supported different data acquisitions in the Mauvoisin region. They have also provided long-term measurement series of the inflow to the reservoir. Further, we thank the *Center for Climate Systems Modeling (C2SM)* which provided regional climate scenarios of FUGE project. Constructive comments of two anonymous reviewers helped to improve the manuscript. Finally, we would like to acknowledge Bruno Nendela and Hermann Bösch for topographic and photogrammetrical analysis. This study is a contribution to NRP 61.

# Chapter 3

# A comparison of empirical and physically based glacier surface melt models for long-term simulations of glacier response

J. Gabbi[1], M. Carenzo[2], F. Pellicciotti[2], A. Bauder[1] and M. Funk[1]

[1]Laboratory of Hydraulics, Hydrology and Glaciology (VAW), ETH Zürich, Zürich, Switzerland
[2]Institute of Environmental Engineering, ETH Zürich, Zürich, Switzerland

Published, Journal of Glaciology

**Citation** Gabbi J., M. Carenzo, F. Pellicciotti, A. Bauder, and M. Funk (2014). A comparison of empirical and physically based glacier surface melt models for long-term simulations of glacier response. *Journal of Glaciology*, 60(224), 1140-1154.

**Abstract**

We investigate the performance of five glacier melt models over a multi-decadal period in order to assess their ability to model future glacier response. The models range from a simple degree-day model based solely on air temperature to more sophisticated models including the full shortwave radiation balance. In addition to the empirical models, the performance of a physically-based energy-balance model (EB) is examined. The melt models are coupled to an accumulation and a surface evolution model and applied in a distributed manner to Rhonegletscher (Switzerland) over the period 1929-2012 at hourly resolution. For calibration, seasonal mass balance measurements (2006-2012) are used. Decadal ice volume changes for six periods in the years 1929-2012 serve for model validation. Over the period 2006-2012, almost no differences in performance among the models are evident except for EB, which is less consistent with observations likely due to lack of meteorological in-situ data. However, simulations over the long-term (1929-2012) reveal that models which include a separate term for shortwave radiation agree best with the observed ice volume changes, indicating that their melt relationships are robust in time and thus suitable for long-term modelling in contrast to more empirical approaches that are over-sensitive to temperature fluctuations.

## 3.1 Introduction

Several studies have demonstrated the impact of the expected 21st century climate change on glaciers mass balance at the regional and global scale (Le Meur et al., 2007; Huss et al., 2008b; Farinotti et al., 2012; Radic et al., 2014). Model simulations however depend on the type of models used (Pellicciotti et al., 2013; Huss et al., 2014). Approaches to compute melt range from empirical models such as simple temperature-index models to more sophisticated physically based energy-balance models. Temperature-index models require only temperature as input and are based on an assumed linear relationship between this variable and melt rates, whereas energy-balance models are based on the computation of all relevant energy fluxes at the glacier surface and thus require extrapolation of numerous meteorological and surface input variables at the glacier scale. There is a large variety in the degree of sophistication of the approaches incorporating more or less meteorological input variables (Johannesson et al., 1995; Cazorzi and Fontana, 1996; Hock, 1999; Hock and Holmgren, 2005; Anslow et al., 2008). Advancements over the simple dependence of melt on air temperature by addition of radiation terms have been recently suggested (Cazorzi and Fontana, 1996; Hock, 1999; Pellicciotti et al., 2005), and named enhanced temperature-index models. In contrast to simple temperature-index models, enhanced temperature-index models provide a better representation of the spatial and temporal variability of melt controlled by solar radiation. Some of these approaches also cope better with the physical character of the melt process and provide a promising approach to model melt at the glacier-wide scale with fewer input data than energy-balance models, but with a higher accuracy than standard temperature-index models. Pellicciotti et al. (2005) presented such an enhanced temperature-index melt model and showed that the performance compared to conventional temperature-index models was significantly higher. The authors suggested that simpler models that are directly dependent on air temperature might be oversensitive to temperature fluctuations. The model comparison was performed at the point scale with measured input data from five automatic weather stations operated over one ablation season at Haut Glacier d'Arolla (Switzerland). Carenzo et al. (2009) tested the transferability of the enhanced temperature-index model and showed that model parameters calibrated over one season could be applied to another year or another site with only a small decrease in model performance. The stronger physical basis might imply that the model parameters are less dependent on meteorological conditions and thus more robust in time. In contrast, there are indications that the parameters of simple temperature-index models are not stable over decadal periods and thus require recalibration for individual subperiods (Huss et al., 2009b), which question their suitability for future glacier projections. Physically based energy-balance models provide accurate point melt rates when high quality, in-situ records of meteorological variables are available (Pellicciotti et al., 2013). However, their performance decreases when forced with data recorded outside of the glacier boundary layer, where the equations of the energy fluxes are valid. As a result, it might be questioned whether they still represent the best model approach for spatially distributed simulations and long term modelling, when meteorological input variables need to be extrapolated from off-glacier stations. Despite this, several studies have applied distributed energy-balance models forced with data of off-glacier weather stations (e.g. Klok and Oerlemans, 2002; Gerbaux et al., 2005).

The aim of this study is to examine the performance of five different melt models, (1) a *classical temperature-index model* (TI), (2) the *temperature-index model of Hock (1999)* (HTI), (3) an *enhanced temperature-index model* (ETI), (4) a *simplified energy-balance model* (SEB), and (5) an *energy-balance model* (EB) over multiple decades (1929-2012) to study the

performance of the different approaches for long-term modelling studies. The selected models range from the most simple (empirical) to the most complex (physically-based) form of melt equation and are well established and widely used melt models commonly applied for mass balance studies. The robustness of the parameters of the empirical models (TI, HTI, ETI, SEB) over a period of several years (2006-2012) is investigated using repeated mass balance measurements. In order to test the multi-seasonal glacier mass balance evolution, the melt models are coupled to an accumulation and a mass balance redistribution model and are applied to Rhonegletscher, Swiss Alps, in a distributed manner. Meteorological data from the nearby weather station at Grimsel Hospiz operated by MeteoSwiss are used to force the models. The simple TI model is based on few input data and requires only air temperature and precipitation while the HTI model needs in addition an index of potential, clear-sky solar radiation. The ETI and the SEB models require instead of the potential radiation the full shortwave radiation balance, i.e. the actual incoming and outgoing shortwave radiation, the latter being defined by the surface albedo. Solar radiation is calculated on the basis of a radiation model for clear-sky conditions and a cloud factor. The EB model is the most data demanding approach, as it requires beside air temperature, precipitation and incoming and reflected shortwave radiation also the longwave radiation flux, wind speed and relative humidity, as well as knowledge of surface characteristics such as surface roughness.
Rhonegletscher has been intensively investigated, in particular in the recent years. A comprehensive set of subseasonal mass balance and accumulation measurements for the period 2006-2012 provides extensive mass balance data and serves as basis for the calibration of the model parameters. For each year of the period 2006-2012 individual model parameters are calibrated by minimizing the difference between simulated and observed subseasonal mass balance measurements. Furthermore, a mean parameter set calculated from all available mass balance measurements of the years 2006-2012 is determined and adopted for the long-term modelling (1929-2012). The performance of the five models is validated against decadal ice volume changes derived by seven digital elevation models covering the period 1929-2012. Based on the insights gained, we attempt to determine which model is most suited for mass balance modelling over decadal periods and for glacier projections in the 21st century.

## 3.2 Study site & Data

The study site is located in the central Swiss Alps and forms the headwaters of the Rhone river (Fig. 3.1a). Rhonegletscher is a medium-sized valley glacier and covers an area of about 16 $km^2$. The glacier has approximately north-south orientation and ranges in altitude between 2200 and 3600 m asl. Rhonegletscher has a long history of measurements and was particularly in the last decade intensively investigated.
Meteorological data are taken from the weather station *Grimsel Hospiz* (1980 m asl) operated by MeteoSwiss which is the nearest weather station located about 4 km west of the glacier tongue of Rhonegletscher (Fig. 3.1a). The weather station records air temperature, precipitation, global radiation, humidity, wind speed and wind direction in daily resolution since the beginning of 1959 and in hourly resolution since spring 1989. Air temperature measured at the weather station Grimsel is extrapolated by means of seasonal temperature lapse rates with a daily cycle. Recent studies have shown that temperature lapse rates in high elevation catchments exhibit a distinct variability during the day (Carenzo et al., 2009; Petersen and Pellicciotti, 2011) and that this needs to be taken into account when forcing melt models to avoid modelling errors (Petersen and Pellicciotti, 2011; Immerzeel et al., 2014). Neglecting

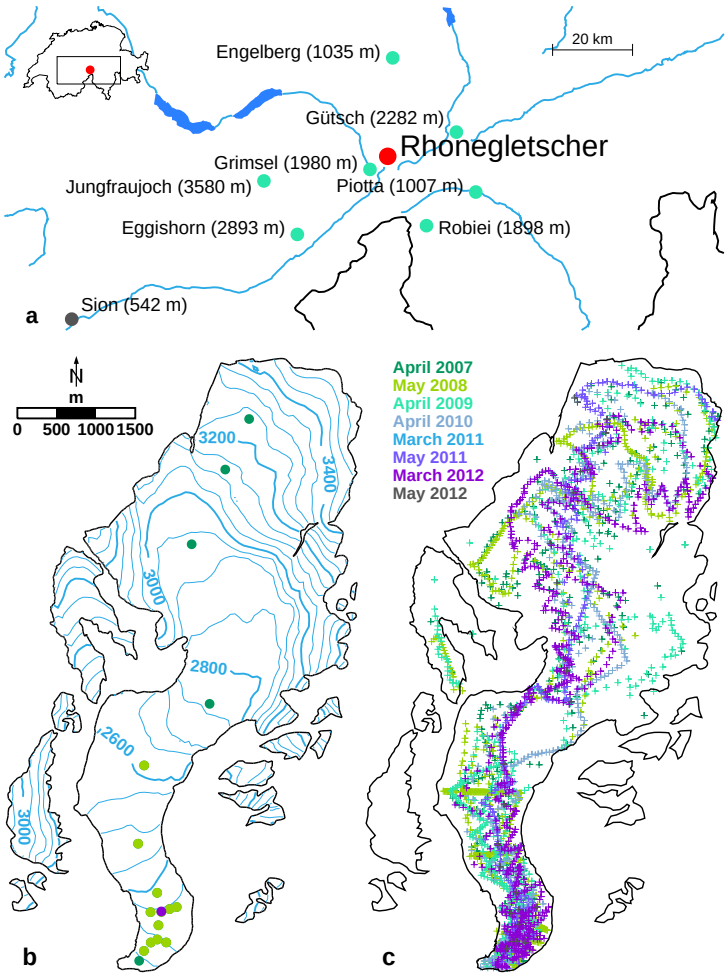


Figure 3.1: (a) The location of Rhonegletscher (red dot) and of the weather station Grimsel Hospiz and the six additional weather stations used to derive temperature lapse rates (green dots). The numbers refer to the elevation of the weather stations. (b) Overview of the study site with the location of the ablation stakes (dots) and of the fixed pyranometer (violet dot). Light green dots show the location of the albedo measurements carried out every second to third week in summer 2011. (c) Position of the snow depth measurements of the years 2007-2012.

a daily cycle could result in an overestimation of air temperatures during the central hours of the day and lower temperatures during night. Air temperature data of seven weather stations within a radius of 32 km from Rhonegletscher ranging between 1007 and 3580 m asl (Grimsel, Gütsch, Robiei, Piotta, Engelberg, Eggishorn and Jungfraujoch) covering the period 1994-2012 are used to derive hourly lapse rates (Fig. 3.1a). Data of the weather station Ulrichen are not considered, because air temperatures at Ulrichen are strongly affect by cold air drainage particularly during winter months (Scherrer, 2014). Air temperature lapse rates show a persistent daily cycle with maximum absolute values around noon (Fig. 3.2). Steepest temperature lapse rates of $-0.0063\,^{\circ}\mathrm{C\,m^{-1}}$ occur in spring and summer and shallower gradients ($-0.0045\,^{\circ}\mathrm{C\,m^{-1}}$) in winter probably due to inversion of air temperatures during the cold season (Rolland, 2003). Coefficients of determination for the temperature gradient analysis are overall high ($r^2 > 0.96$).

The mass balance model is run on an hourly basis. For this reason, the daily temperature

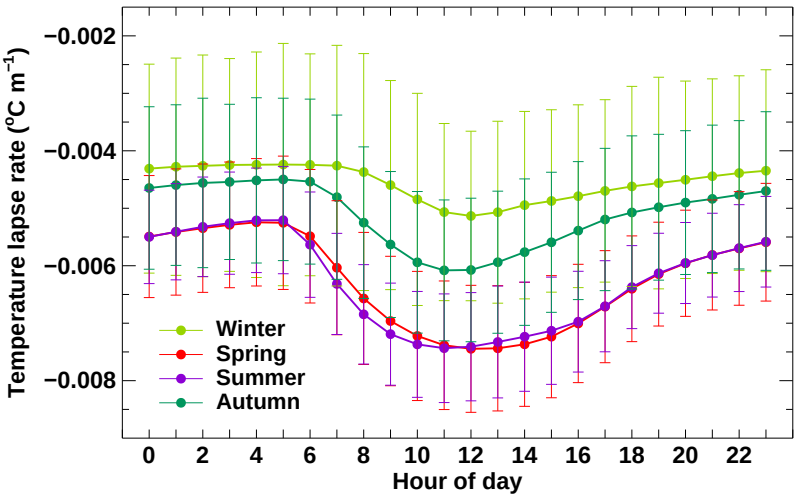


Figure 3.2: Hourly temperature lapse rates and the corresponding standard deviations for each season computed by linear regression of hourly temperatures of the period 1994-2012 recorded at seven weather stations in the surrounding of Rhonegletscher against altitude.

records of the period 1959-1989 are converted into hourly data by superimposing diurnal variations on the mean daily temperatures. Measured minimum and maximum daily temperatures are employed to constrain daily temperature fluctuations. In an iterative procedure, hourly temperature values are generated by taking the daily temperature fluctuations within a day in the period 1989-2012 which exhibited as similar as possible distribution of minimum, maximum and average temperature. Only days of the same month are considered. Hourly precipitation time series were derived in a similar manner except that only information about the total daily precipitation and not about peak values were available.

For the period 1929-1959 no climate records exist for the weather station Grimsel. Hence, air temperature from Jungfraujoch (operating since the beginning of the year 1933) is used, because the station shows the highest correlation with temperature measured at Grimsel compared to other stations in the surrounding with a long recording history ($r^2 = 0.92$). The temperature measured at Jungfraujoch is extrapolated to the altitude of the weather station Grimsel by seasonal lapse rates determined by evaluating temperature deviations between the two stations in the overlapping measuring period (1959-2012). For the first three years, 1930-1932, temperatures measured at Sion are used. In the case of precipitation, data of the weather station Sion are employed and shifted according to seasonal lapse rates to the location of Grimsel. Then, the daily values are converted to hourly values as described in the previous section. The generation of distributed precipitation fields from station measurements is described in Section *Accumulation model*.

Repeated mass balance measurements were carried out in the period 2006-2012 (01.10.2006-30.09.2012). Between 11 and 17 stakes were installed in the ablation and accumulation area of Rhonegletscher (Fig. 3.1b). In 2010 and 2011 additional stakes were installed in the tongue area. The mass balance was usually measured at the beginning and end of the accumulation period and several times (9-14 times) during the ablation period. In total, more than 1000 stake readings are available. The uncertainty of mass balances measurements is estimated as $\pm 0.2$ m w.e. $a^{-1}$ (Dyurgerov, 2002). Snow depth measurements were carried out at the end of the accumulation season of each year in the period 2007-2012 (Fig. 3.1c). Two additional surveys were performed in 2011 and 2012 at the beginning of March. Simultaneously, snow

density profiles were measured at one up to five locations during the snow depth surveys. Six digital elevation models (DEMs) derived from a historic topographic map and aerial photographs of the years 1929, 1959, 1980, 1991, 2000, and 2007 with a spatial resolution of 25 m exist for Rhonegletscher (Bauder et al., 2007). For the year 2012 a partial DEM of the ablation area of Rhonegletscher exists. The DEM of the year 1929 serves as input for the modelling; the other six DEMs are used for validation of the model outputs by deriving decadal ice volume changes. Geodetically determined ice volume changes are affected by an error of about $\pm 5\%$ (Bauder et al., 2007). The total volume change of the period 2007-2012 is obtained by scaling the observed ice volume change of the partial DEM according to the proportion of ice volume changes of previous periods which fall within this zone (47 - 61%). In summer 2011 and 2012, the albedo of the glacier surface was recorded continuously at one site and in 2011 also every second to third week at 12 additional locations within the ablation area (see Fig. 3.1b), providing the mean ice albedo ($\alpha_{\text{ice}} = 0.24 \pm 0.06$) for Rhonegletscher. The topography of the glacier bed and hence the ice volume distribution is known (Farinotti et al., 2009b).

## 3.3 Methods

For the melt model comparison, five distributed melt models with varying complexity are considered which are described in the following subsections.

### 3.3.1 Classical temperature-index melt model

The classical temperature-index melt model is solely based on air temperature and relates linearly melt rates to air temperature by a melt factor differing for snow and ice surfaces:

$$M = \begin{cases} \frac{1}{n} DDF_{\text{ice/snow}}\, T_{\text{a}} & : \quad T_{\text{a}} > T_{\text{T}} \\ 0 & : \quad T_{\text{a}} \leq T_{\text{T}} \end{cases} \tag{3.1}$$

where $DDF_{\text{ice/snow}}$ is the degree-day factor for ice and snow, respectively ($\text{mm}\,\text{d}^{-1}\,^{\circ}\text{C}^{-1}$), $T_{\text{a}}$ the air temperature (°C), $n$ the number of time steps per day (here $n = 24$) and $T_{\text{T}}$ the threshold temperature distinguishing between melt and no melt ($T_{\text{T}} = 1\,^{\circ}\text{C}$, Pellicciotti et al., 2005). $T_{\text{T}}$ accounts for the fact that melt is controlled by the energy budget at the surface and can also occur at air temperatures below and above the melting point of snow and ice (Kuhn, 1987). The model keeps track of the snow water equivalent in each grid cell of the modelling domain, and when this is zero ice melt is calculated.

### 3.3.2 Temperature-index melt model of Hock (1999)

In contrast to the classical temperature-index model where melt varies in space only as a function of elevation (given by temperature lapse rates), the temperature-index model by Hock (1999) includes a term for clear-sky potential solar radiation in order to account for topographic effects such as exposition, slope and shading on the spatial distribution of melt, but without the need of additional meteorological variables such as radiation and cloud data. Melt rates ($\text{mm}\,\text{h}^{-1}$) are obtained as:

$$M = \begin{cases} (MF + R_{\text{ice/snow}}\, I_{\text{pot}})\, T_{\text{a}} & : \quad T_{\text{a}} > T_{\text{T}} \\ 0 & : \quad T_{\text{a}} \leq T_{\text{T}} \end{cases} \tag{3.2}$$

where $MF$ is the melt factor ($\mathrm{mm\,h^{-1}\,{}^{\circ}C^{-1}}$), $R_{\mathrm{ice/snow}}$ the radiation factors for ice and snow ($\mathrm{mm\,m^2\,h^{-1}\,W^{-1}\,{}^{\circ}C^{-1}}$) and $I_{\mathrm{pot}}$ the potential clear-sky direct solar radiation ($\mathrm{W\,m^{-2}}$). Radiation factors are different for snow and ice surface in order to account for differences in the surface characteristics such as the albedo. The potential, clear-sky direct solar radiation is calculated following Hock (1999) as a function of solar geometry, topography and atmospheric transmissivity assuming a constant clear-sky atmospheric transmissivity in space and time:

$$I_{\mathrm{pot}} = I_0 \left(\frac{R_{\mathrm{m}}}{R}\right)^2 \psi_{\mathrm{a}}^{\left(\frac{P}{P_0 \cos Z}\right)} \cos\theta \tag{3.3}$$

where $I_0$ is the solar constant, $R_{\mathrm{m}}$ and $R$ the mean and actual sun-earth distance, $\psi_{\mathrm{a}}$ the atmospheric transmissivity, $P$ the atmospheric pressure and $P_0$ the pressure at sea level, $Z$ is the solar zenith angle and $\theta$ the incidence angle of the sun on the surface.

### 3.3.3 Enhanced temperature-index melt model

The enhanced temperature-index melt model by Pellicciotti et al. (2005) has a more physical basis through the inclusion of the shortwave radiation balance and distinguishes between melt induced by solar radiation and melt induced by other heat fluxes (temperature induced melt). Melt is calculated according to:

$$M = \begin{cases} TF\,T_{\mathrm{a}} + SRF(1-\alpha)\,I & : \quad T_{\mathrm{a}} > T_{\mathrm{T}} \\ 0 & : \quad T_{\mathrm{a}} \leq T_{\mathrm{T}} \end{cases} \tag{3.4}$$

where $TF$ is the temperature factor ($\mathrm{mm\,h^{-1}\,{}^{\circ}C^{-1}}$), $SRF$ the shortwave radiation factor ($\mathrm{mm\,m^2\,h^{-1}\,W^{-1}}$), $\alpha$ the surface albedo and $I$ the incoming shortwave radiation ($\mathrm{W\,m^{-2}}$).
The actual incoming shortwave radiation ($I$) is computed as a product of clear-sky incoming shortwave radiation according to Iqbal (1983) and Corripio (2003) and a cloud transmission factor ($cf$) representing the attenuation of solar radiation by clouds. The clear-sky incoming shortwave radiation is calculated as the sum of direct, diffuse and reflected shortwave radiation and requires the exact position of the sun and its interaction with the surface topography as well as knowledge about the transmissivity of the atmosphere. The transmittance of Rayleigh scattering, ozone, uniformly mixed gases, water vapor and aerosols as well as the altitude dependency is accounted for and is computed on the basis of the concept of the relative optical air mass (Bird and Hulstrom, 1981). Cloud transmissivity factors (i.e. the ratio of observed to simulated clear-sky incoming shortwave radiation) are derived according to Pellicciotti et al. (2011) as a function of daily temperature ranges. The cloud factor parameterisation is recalibrated against measured global radiation and daily temperature ranges ($\Delta T$) at the weather station Grimsel, resulting in the following relationship:

$$cf = 0.084\,\Delta T + 0.120 \qquad (r^2 = 0.522). \tag{3.5}$$

For the ice albedo a value of 0.24 is assumed. The albedo of snow is calculated according to Brock et al. (2000) as a function of the accumulated daily maximum positive air temperature since the last snowfall ($T_{\mathrm{acc}}$). The associated parameters are adopted from Pellicciotti et al. (2005):

$$\alpha_{\mathrm{snow}} = a_1 - a_2 \log_{10} T_{\mathrm{acc}}, \tag{3.6}$$

where $a_1 = 0.86$ and $a_2 = 0.155$. The recalibration of the parameterisation against the albedo measurements during summer snow fall events by the pyranometer on the tongue of Rhonegletscher (summer 2011 and 2012), yields the same value for parameter $a_2$ describing the decline of the albedo after a snow fall event as proposed by Pellicciotti et al. (2005). For $a_1$ a different value is obtained, likely due to the fact that after a summer snow fall event the albedo drops back rapidly to the albedo of the underlying ice, which is lower than the albedo of snow.

### 3.3.4 Simplified energy-balance melt model

The simplified energy-balance model by Oerlemans (2001) is very close the the enhanced temperature-index model by Pellicciotti et al. (2005), but instead of using a threshold temperature for the onset of melt, the available melt energy is calculated and converted to melt rates by the latent heat of fusion. The melt energy $Q_M$ ($W\,m^{-2}$) is obtained as:

$$Q_M = (1 - \alpha)I + C_0 + C_1 T_a, \tag{3.7}$$

where $C_0$ ($W\,m^{-2}$) and $C_1$ ($W\,m^{-2}\,K^{-1}$) are empirical factors which describe the temperature dependent energy fluxes. The incoming shortwave radiation $I$ and the albedo $\alpha$ are calculated as in the ETI model. Melt rates $M$ ($m\,s^{-1}$) are obtained by dividing the melt energy by the latent heat of fusion $L_f$ (333'700 $J\,kg^{-1}$) and the density of water $\rho_w$ (1'000 $kg\,m^{-3}$):

$$M = \frac{Q_M \Delta t}{L_f \rho_w}. \tag{3.8}$$

where $\Delta t$ (s) is the time step. Melt occurs only when the melt energy is larger than zero.

### 3.3.5 Energy-balance melt model

The energy-balance model used in this work is described in detail in Carenzo (2012) and the reader is referred to that publication for details. Here we only recall its main characteristics. The energy balance at the glacier-atmosphere interface is given by:

$$Q_M = (1 - \alpha)\, SW{\downarrow} + LW{\downarrow} - LW{\uparrow} + Q_H + Q_L + Q_S, \tag{3.9}$$

where $Q_M$ is the melt energy, $\alpha$ the albedo, $SW{\downarrow}$ the incoming shortwave radiation, $LW{\downarrow}$ and $LW{\uparrow}$ the incoming and outgoing longwave radiation, $Q_H$ the turbulent sensible heat flux, $Q_L$ the turbulent latent heat flux and $Q_S$ the heat conduction into the snow/icepack. Melt rates are computed by Equation 3.8. Ablation is the sum of melt and sublimation minus resublimation. Sublimation $S$ ($m\,s^{-1}$) is computed as:

$$S = \frac{Q_L \Delta t}{L_s \rho_w}, \tag{3.10}$$

where $L_s$ is the latent heat of sublimation (2'834'000 $J\,kg^{-1}$).
The measured incoming shortwave radiation is distributed over the glacier based on the spatially varying incident sun angle, the sky view fraction and the surface property (i.e. albedo, Corripio, 2002). Albedo of snow and ice is modelled in the same way as in ETI.
The incoming longwave radiation $LW{\downarrow}$ is calculated according to the Stefan-Boltzmann relationship and depends on the absolute air temperature, the percentage of cloud coverage and the cloud type (Brock and Arnold, 2000). The outgoing longwave radiation $LW{\uparrow}$ is computed

following the Stefan-Boltzmann relationship as a function of surface temperature (calculated each time step as a function of the energy penetrating into the snow/icepack with a heat conduction scheme, see Pellicciotti et al. (2009) and surface emissivity (snow and ice surface emissivity is set to 1, assuming that the surface radiates as a black body (Oke, 1987)).

The turbulent sensible and latent heat fluxes are calculated according to the bulk aerodynamic method as a function of air temperature, humidity and wind speed (e.g. Munro, 1989). In contrast to the profile aerodynamic method, the meteorological variables are required only for one height above ground level. In addition, the scaling lengths for aerodynamic roughness $z_0$, temperature $z_t$ and humidity $z_e$, the stability-correction factors for momentum, the heat and humidity and the Monin-Obukhov length scale have to be known. Different values for $z_0$ are assigned to fresh snow ($z_0 = 0.1$ mm), snow after snowfall when melting has taken place ($z_0 = 1.0$ mm) and ice ($z_0 = 2.0$ mm) as proposed by Pellicciotti et al. (2005). $z_t$ and $z_e$ are calculated from the roughness Reynolds number and $z_0$. Due to a lack of additional measurements and the complexity of wind and humidity fields, wind speed and relative humidity are assumed to be constant in space over the modelling domain and equal to those measured at Grimsel weather station (located 4 km from the glacier tongue, see Fig. 3.1a).

### 3.3.6 Accumulation model

The repeated snow depth measurements are utilized to derive precipitation fields. In a first step, precipitation fields were calculated using valley precipitation lapse rates determined from precipitation data of six weather stations located in the Rhone valley and of weather station Grimsel. However, comparisons with snow depth measurements showed that, particularly at high altitudes, snow water equivalents are underestimated, revealing that valley lapse rates are too flat. The snow depth measurements show a consistent pattern of moderate, nearly constant snow depths below 2600-2700 m asl and a stronger increase in the upper area (Fig. 3.3). The uniform snow depths in the lower part of the glacier might be a result of enhanced wind redistribution due to a wind tunnel effect in the narrow valley at the glacier tongue. To account for the observed increase with altitude, elevation dependent lapse rates are determined for elevation bands of 100 m by comparing measured snow water equivalents (corrected for snow melt and snow redistribution) with snow water equivalents at the weather station Grimsel inferred from precipitation measurements by applying a threshold temperature of 1 °C to distinguish between solid and liquid precipitation. For the years 2007-2012, for which snow depth surveys are available, individual lapse rates are derived whereas for the other years a mean set of lapse rates is used. Annual elevation dependent lapse rates range between 0.024 and 0.096 % $m^{-1}$ and mean gradients of the period 2007-2012 between 0.038 and 0.069 % $m^{-1}$. The correlation between modelled and measured snow water equivalents of all years reveals a coefficient of determination $r^2$ of 0.71. For individual years $r^2$ ranges between 0.51 and 0.85 (Fig. 3.3).

Precipitation fields are computed by applying these precipitation lapse rates to the hourly precipitation sums measured at the weather station Grimsel. A threshold temperature set to 1 °C is used to distinguish between liquid and solid precipitation (MacDougall and Flowers, 2011). The spatial redistribution of snow by snow drift and avalanches is accounted for with the approach proposed by Huss et al. (2008a) in which accumulation is redistributed according to the terrain parameters curvature and slope.

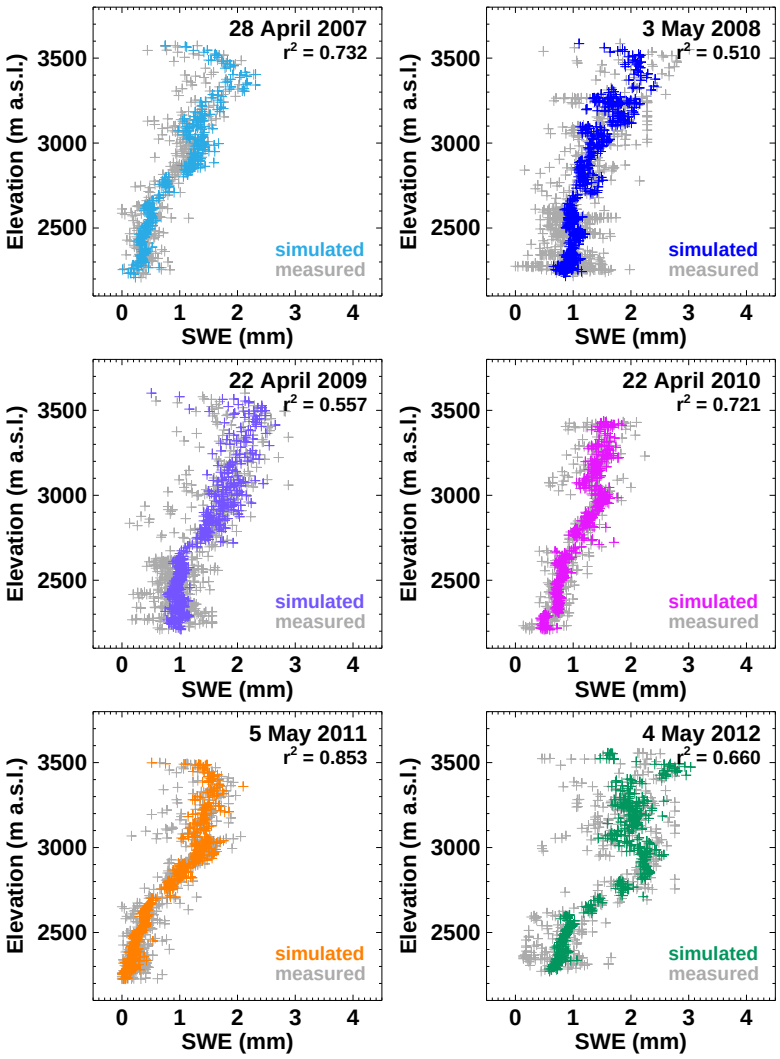


Figure 3.3: Measured and simulated snow water equivalents (SWE) versus elevation for each snow depth survey (at the end of the accumulation period). The coefficients of determination ($r^2$) of measured and modelled snow water equivalents are indicated.

### 3.3.7 Mass balance redistribution model

The melt and accumulation models are forced by hourly temperature and precipitation data for the period 01.10.1929-31.12.2012. The mass balance is evaluated on a DEM with an extent of $7.5 \times 12.5$ km and a grid spacing of 25 m. The mass balance model is coupled to a mass balance redistribution model which updates the geometry of the glacier surface in annual time steps. A simplified approach which redistributes the annual mass balance according to the pattern of historic ice-thickness changes with elevation is used (Huss et al., 2010). For this purpose the relationship between altitude and ice volume changes of Rhonegletscher (given by the six DEMs) is determined and employed for updating the surface topography. In comparison to an ice flow model, this approach requires less computational time. In order to test the influence of the chosen parameterisation for glacier surface geometry changes, we force the five mass balance models with prescribed glacier surface geometries which are obtained by linear interpolation of the glacier surface between two successive DEMs (Huss et al., 2008a) ensuring consistency in glacier elevation and extent among the five models. Results of this test showed that the employed approach only marginally affects model results.

Table 3.1: Parameter ranges and the corresponding increments (Δ) employed for the model calibration of the four empirical models.

| Parameter | Unit | Range | Δ |
|---|---|---|---|
| **TI** | | | |
| $DDF_{ice}$ | $mm\,d^{-1}\,°C^{-1}$ | $3.00 \leftrightarrow 10.00$ | 0.01 |
| $DDF_{snow}$ | $mm\,d^{-1}\,°C^{-1}$ | $3.00 \leftrightarrow 7.00$ | 0.01 |
| **HTI** | | | |
| $MF$ | $mm\,h^{-1}\,°C^{-1}$ | $0.00 \leftrightarrow 0.15$ | 0.01 |
| $R_{ice}$ | $mm\,m^2\,h^{-1}\,W^{-1}\,°C^{-1}$ | $0.000 \leftrightarrow 0.0011$ | 0.0001 |
| $R_{snow}$ | $mm\,m^2\,h^{-1}\,W^{-1}\,°C^{-1}$ | $0.000 \leftrightarrow 0.0011$ | 0.0001 |
| **ETI** | | | |
| $TF$ | $mm\,h^{-1}\,°C^{-1}$ | $0.00 \leftrightarrow 0.31$ | 0.01 |
| $SRF$ | $mm\,m^2\,h^{-1}\,W^{-1}$ | $0.000 \leftrightarrow 0.012$ | 0.0002 |
| **SEB** | | | |
| $C_0$ | $W\,m^{-2}$ | $-5 \leftrightarrow -225$ | 5 |
| $C_1$ | $W\,m^{-2}\,K^{-1}$ | $1 \leftrightarrow 33$ | 1 |

### 3.3.8 Model calibration and validation

The empirical character of the temperature-index models and the simplified energy-balance model requires calibration of the model parameters. The two coefficients of TI ($DDF_{ice}$, $DDF_{snow}$), ETI ($TF$, $SRF$) and SEB model ($C_0$, $C_1$) and the three coefficients of the HTI model ($MF$, $R_{snow}$, $R_{ice}$) are calibrated by means of the weekly to monthly mass balance measurements of the period 2006-2012. Only measurements during the ablation period are considered (April-October). In a first step, the optimal parameter sets are systematically searched in parameter ranges determined from previous studies (e.g. Pellicciotti et al., 2012; Farinotti et al., 2012) and in a later step parameter ranges are extended where needed in order to find the optimum. The parameter ranges and increments employed for the calibration of the different models are listed in Table 4.1. Model performance is determined by calculating the efficiency criteria $R^2$ according to Nash and Sutcliffe (1970) of observed and simulated mass balances ($MB_{obs/sim}$):

$$R^2 = 1 - \frac{\Sigma(MB_{obs} - MB_{sim})^2}{\Sigma(MB_{obs} - \overline{MB_{obs}})^2} \qquad [-\infty, 1]. \tag{3.11}$$

An $R^2$ of 1 indicates perfect fit, an $R^2$ lower than zero that the average value of all observations is a better predictor than the model itself. The parameter combinations with the highest $R^2$ are chosen. Different parameter sets with highest Nash-Sutcliffe efficiency are determined (1) for each individual year of the period 2006-2012 (*yearly calibrated*), taking only ablation measurements of the current year and (2) for the entire period (*multi-yearly calibrated*), incorporating all measurements of the years 2006-2012, in order to analyse the variability of the model parameters over several years and to investigate the difference in performance between yearly and multi-yearly calibrated parameter sets.

For model validation, simulated and observed ice volume changes of the six subperiods (1929-1959, 1959-1980, 1980-1991, 1991-2000, 2000-2007, 2007-2012) and the entire period 1929-2012 are compared. For calibration and validation two independent data sets were used approving the overlap of the calibration period with the validation period.
Multi-yearly calibrated parameters are used to force the models over the long-term period. Observed ice volume changes ($10^6\,m^3$) are converted to cumulative mass balances (m w.e.) assuming an ice density of $900\,kg\,m^{-3}$. As a measure for model performance the absolute and percentage differences of modelled versus measured cumulative mass balances are employed.

## 3.4 Results

### 3.4.1 Parameter variability

The yearly calibrated parameters of the ETI and HTI model vary from year to year (Figs. 3.4, 3.5a). The temperature factors of ETI fluctuate in a range of 0.00 and 0.25 and the shortwave radiation factors between 0.0012 and 0.0100. The melt factors of HTI range between 0.02 and 0.14 and the radiation factors for snow and ice between 0.0002-0.0006 and 0.0004-0.0008, respectively (Tab. 3.2). Variations in the yearly calibrated parameter values are for both melt models of similar magnitude. The temperature factors of ETI and HTI ($TF$, $MF$) vary in a range of about $\pm$100% compared to the mean over all years. The variations in the radiation factors ($SRF$, $R_{snow/ice}$) are smaller and range between –80 and +60% for $SRF$ and between –50 and +50% for $R_{snow/ice}$. In the case of SEB, variations are also high, with coefficients of variation of –0.64 and 0.42, but the parameters seem to be more robust for the years 2009-2012, for which they are identical or very close to the multi-yearly calibrated parameter values of $C_0 = -75$ and $C_1 = 15$. In 2007, a higher $C_1$ compensates for a lower $C_0$ value compared to the mean and in 2008 the opposite is true, with a lower $C_1$ balanced by a higher $C_0$. Due to the two deviating years, the variations of $C_0$ and $C_1$ are in the order of –80 to 115% ($C_0$: –80$\leftrightarrow$115%; $C_1$: –79$\leftrightarrow$50%) comparable to the variations of the parameters of ETI and HTI. The yearly calibrated degree-day factors of the TI model demonstrate clearly lower variations i.e. the coefficient of variations are 0.09 and 0.16 for $DDF_{ice}$ and $DDF_{snow}$, as there is no possibility for compensation.
The multi-yearly calibrated parameters of TI, ETI and SEB are close to the mean of all yearly calibrated parameters (Fig. 3.4). In the case of HTI, the multi-yearly calibrated temperature factor $MF$ is higher and the radiation factors $R_{snow}$ and $R_{ice}$ are lower than the mean. In general, years with high temperature factors are accompanied by low radiation factors and vice versa.
Meteorological conditions of the multi-year period are listed in Table 3.3. Years with high temperature factors (e.g. 2010, see Fig. 3.5a) are correlated with low incoming solar radiation and thus predominately overcast conditions whereas years with low temperature factors (e.g. 2007) are related to clear-sky conditions. This observation is in accordance with the results obtained by Carenzo et al. (2009) who concluded that parameter variations are induced by the changing contribution of the individual fluxes to the energy balance i.e. on cloudy days the shortwave radiation flux is reduced whereas the longwave radiation flux and the turbulent heat fluxes are enhanced leading to higher temperature factors and lower radiation factors. Furthermore, we can observe that years with low temperature factors (e.g. 2007) are generally associated with an earlier depletion of the snow cover whereas years with a long lasting winter snow cover (e.g. 2010) correspond to high temperature factors (Tab. 3.3).

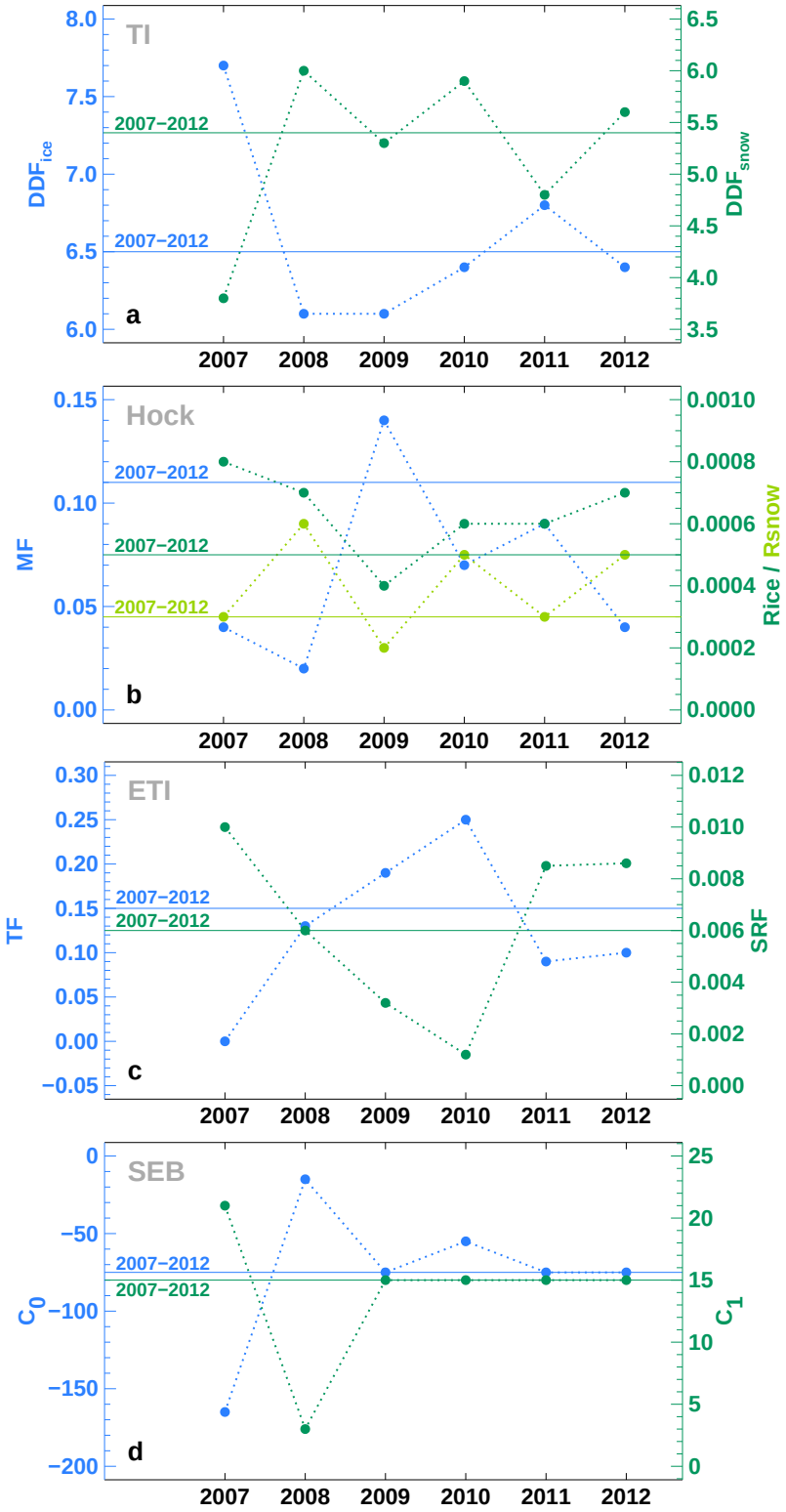


Figure 3.4: The yearly calibrated model parameters of (a) the TI , (b) HTI, (c) ETI and (d) SEB model for the years 2007-2012. The horizontal lines show the multi-yearly calibrated parameter values.

Table 3.2: Yearly and multi-yearly calibrated parameters of TI, HTI, ETI and SEB models and the corresponding coefficient of variation ($c_v$) which is defined as the ratio of the standard deviation to the mean and indicates the variability of the model parameters.

| | TI | | | HTI | | ETI | | SEB | |
|---|---|---|---|---|---|---|---|---|---|
| Year | $DDF_{ice}$ | $DDF_{snow}$ | $MF$ | $R_{snow}$ | $R_{ice}$ | $TF$ | $SRF$ | $C_0$ | $C_1$ |
| | $\left[\frac{mm}{d\,°C}\right]$ | $\left[\frac{mm}{d\,°C}\right]$ | $\left[\frac{mm}{h\,°C}\right]$ | $\left[\frac{mm}{m^2hW\,°C}\right]$ | $\left[\frac{mm}{m^2hW\,°C}\right]$ | $\left[\frac{mm}{h\,°C}\right]$ | $\left[\frac{mm}{m^2hW}\right]$ | $\left[\frac{W}{m^2}\right]$ | $\left[\frac{W}{m^2K}\right]$ |
| 2007 | 7.7 | 3.8 | 0.04 | 0.0003 | 0.0008 | 0.00 | 0.0100 | –165 | 21 |
| 2008 | 6.1 | 6.0 | 0.02 | 0.0006 | 0.0007 | 0.13 | 0.0060 | –15 | 3 |
| 2009 | 6.1 | 5.3 | 0.14 | 0.0002 | 0.0004 | 0.19 | 0.0032 | –75 | 15 |
| 2010 | 6.4 | 5.9 | 0.07 | 0.0005 | 0.0006 | 0.25 | 0.0012 | –55 | 15 |
| 2011 | 6.8 | 4.8 | 0.09 | 0.0003 | 0.0006 | 0.09 | 0.0085 | –75 | 15 |
| 2012 | 6.4 | 5.6 | 0.04 | 0.0005 | 0.0007 | 0.10 | 0.0086 | –75 | 15 |
| 2007-2012 | 6.5 | 5.4 | 0.11 | 0.0003 | 0.0005 | 0.15 | 0.0060 | –75 | 15 |
| $c_v$ | 0.09 | 0.16 | 0.65 | 0.39 | 0.22 | 0.68 | 0.55 | –0.64 | 0.42 |

The calibration of the melt models reveals a strong correlation between the temperature factor and the radiation factor of the ETI model as well as between $C_0$ and $C_1$ of SEB, indicated by the elongated area with similarly high efficiency criteria (Fig. 3.5a, shown for the example of ETI). This has been termed an equifinality problem, by which several combinations of model parameters result in the same model performance (see e.g. Finger et al., 2011). However, the difference among the parameter combinations is evident in the diurnal variations of melt rates (Fig. 3.5b, shown for the example of ETI) whereby higher temperature factors yield shallower daily melt cycles than higher solar radiation factors. Daily fluctuations of air temperature and solar radiation only secondarily influence the daily melt cycle (Fig. 3.5c, d). The coarse temporal resolution of the mass balance measurements (available at intervals of several days) does not allow to determine the true proportion of temperature and solar radiation induced melt and data of higher time resolution (hourly data) would be required to obtain more realistic daily melt cycles. Particularly with regard to the climate change related temperature increase, it is important to assess the effective ratio between temperature and solar radiation induced melt.

The threshold temperature for melt to occur ($T_T$) is kept constant and not recalibrated, following a commonly used approach (e.g. Hock, 1999; Pellicciotti et al., 2005). This parameter might also vary from year to year, but Pellicciotti et al. (2012) have shown that for a number of sites and seasons in the Swiss Alps the recalibrated $T_T$ of the ETI model did not vary much indicating that parameter values around 0 or 1 °C (values commonly assumed) are reasonable.

### 3.4.2 Multi-year modelling: 2006-2012

#### Melt model comparison

The yearly calibration of the model parameters reveals a very similar performance of the four empirical melt models, TI, HTI, ETI and SEB (Fig. 3.6). The Nash-Sutcliffe efficiency criteria

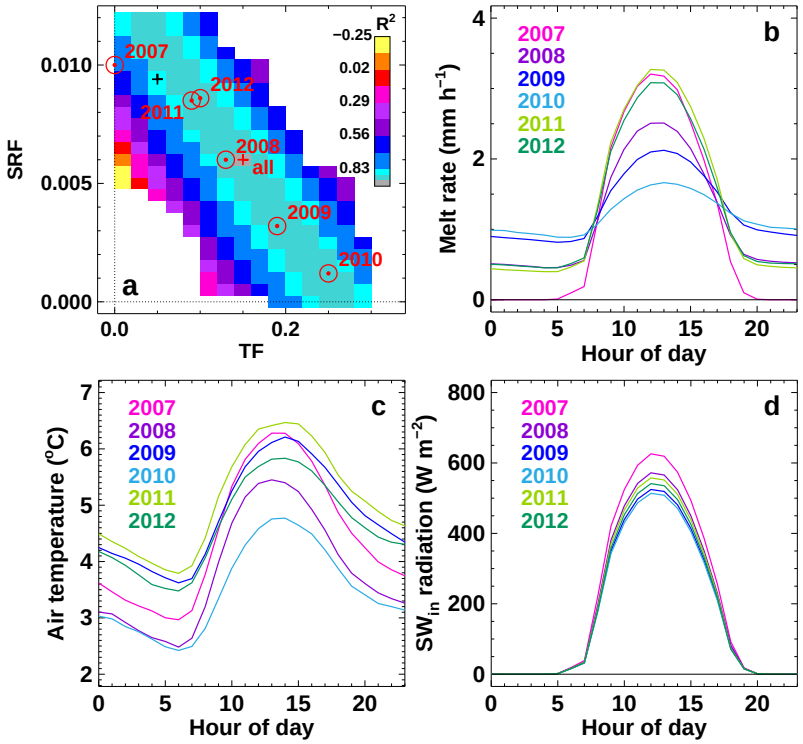


Figure 3.5: (a) The Nash-Sutcliffe efficiency criteria corresponding to the combinations of the two parameters *TF* and *SRF* of the ETI model around the optimum. The colors indicate the magnitude of the efficiency criteria of the calibration over the 6-year period. The red circles and the red cross show the optimal parameter set for the individual years and the entire period 2007-2012. The black cross refers to the parameter set proposed by Pellicciotti et al. (2005). Figures (b), (c) and (d) show the mean daily cycle of surface melt, air temperature and incoming solar radiation over the ablation seasons of the individual years obtained by yearly calibrated parameter values.

Table 3.3: Mean air temperature ($T_a$), mean incoming shortwave radiation (SW↓), mean albedo ($\alpha$), mean cloud coverage (cf), the date when the glacier surface becomes snow free ($dt_{ice}$), numbers of days with ice melt ($d_{ice}$), total solid precipitation ($P_{sol}$) and total melt (M) in the ablation periods 2007-2012 at the central stake (indicated by the violet dot in Fig. 3.1b).

| Year | $T_a$ [°C] | SW↓ [$\frac{W}{m^2}$] | $\alpha$ [-] | cf [-] | $dt_{ice}$ [-] | $d_{ice}$ [%] | $P_{sol}$ [mm] | M [m] |
|---|---|---|---|---|---|---|---|---|
| 2007 | 4.4 | 124 | 0.41 | 0.65 | 29.04 | 64 | 595 | 7.3 |
| 2008 | 3.8 | 104 | 0.47 | 0.60 | 21.06 | 54 | 607 | 6.5 |
| 2009 | 4.8 | 97 | 0.44 | 0.54 | 15.06 | 54 | 338 | 6.9 |
| 2010 | 3.5 | 84 | 0.52 | 0.53 | 27.06 | 43 | 811 | 5.7 |
| 2011 | 5.1 | 113 | 0.38 | 0.58 | 12.05 | 70 | 346 | 7.4 |
| 2012 | 4.6 | 101 | 0.42 | 0.56 | 15.06 | 62 | 319 | 7.0 |
| 2007-12 | 4.4 | 104 | 0.44 | 0.58 | 05.06 | 58 | 503 | 6.8 |

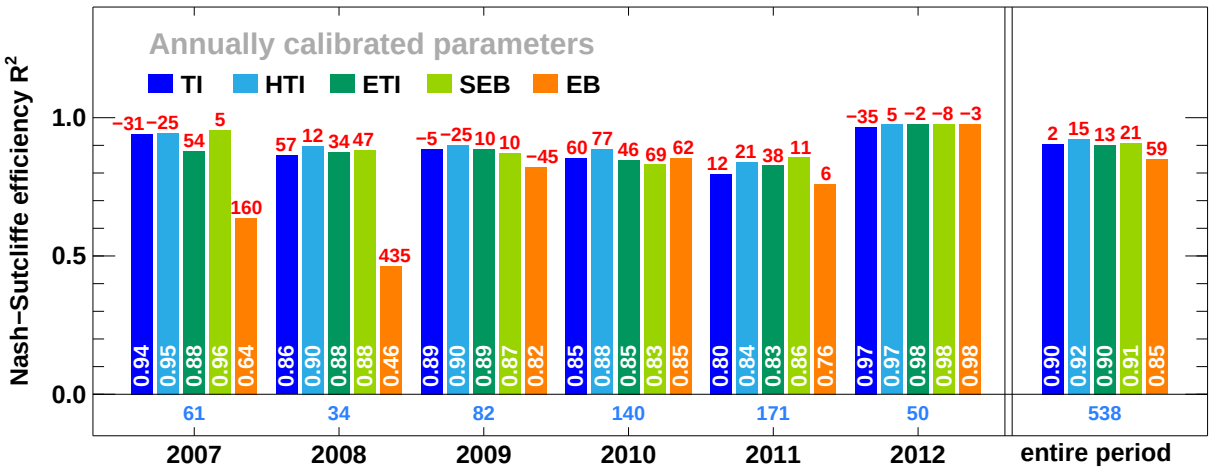


Figure 3.6: Comparison of the model performance of the five melt approach. The Nash-Sutcliffe efficiency criteria of observed and simulated mass balances of the ablation period for each year and the entire period are shown. Blue bars represent the efficiency criteria of TI and HTI, green bars of ETI and SEB and orange bars of EB. White numbers refer to the corresponding efficiency criteria, red numbers to the bias in mm and blue numbers to the number of stake measurements available.

of the observed and simulated mass balances calculated with the yearly calibrated parameters vary between 0.80 and 0.98 for all four models. In contrast, the energy-balance model shows a weaker performance, particularly in the years 2007 and 2008. The corresponding Nash-Sutcliffe efficiency criteria range from 0.46 to 0.98. In 2010 and 2012, the EB model shows higher performance similar to that of the other melt models. Exceptionally high performance and almost no variations among the different melt models is obtained for the year 2012, with $R^2$ of 0.97-0.98. Reasons for the good agreement with measurements of 2012 might be related to the fact that the ablation season was not affected by summer snow fall events until mid of September. A sustained period of ice melt favors high performance, as models have been shown to perform worse during periods of transition from snow to ice or of frequent snow falls (Pellicciotti et al., 2005).

The modelling over the entire period 2006-2012 with the best parameters for each year reveals no significant differences between TI, HTI, ETI and SEB ($R^2 = 0.90$-$0.92$) and a lower performance of the energy-balance model, with a Nash-Sutcliffe efficiency criterion of 0.85. In general, HTI has the highest Nash-Sutcliffe efficiency criterion in the different years and over the entire period, although the differences are negligibly small (except for EB). The same conclusion can be also drawn for the calibration of the period 2006-2012 (Fig. 3.7).

The analysis of the model performances over several years indicates that all four models, TI, HTI, ETI and SEB, are appropriate for melt simulations when parameters are calibrated every year or over a period of several years. Despite their simplicity, the TI and HTI approaches compare well with other melt models. In contrast to the empirical melt models, the energy-balance model was not calibrated. It does not achieve the same high performance as the other approaches and a possible reason for this might be the forcing of the EB with data from an off-glacier weather station (see Discussion).

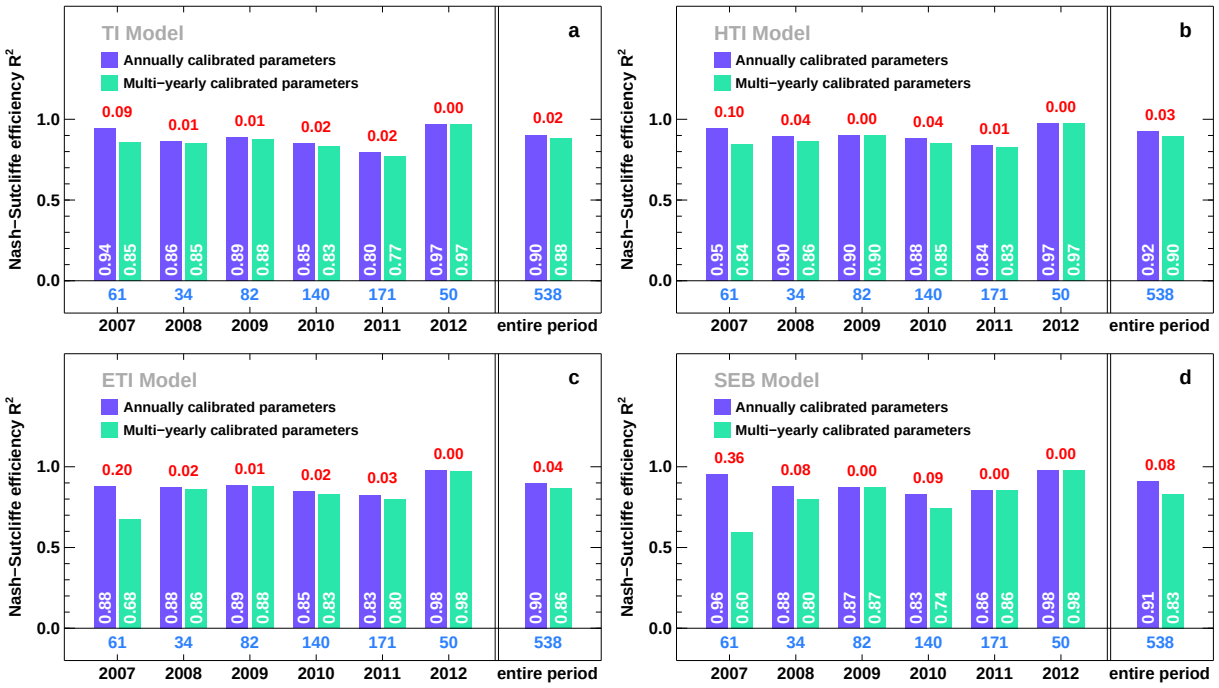


Figure 3.7: Differences in model performance when using annually and multi-yearly calibrated model parameters separately for (a) TI, (b) HTI, (c) ETI and (d) SEB model. The Nash-Sutcliffe efficiency criteria of observed and simulated mass balances of the ablation period for each year and the entire period are shown. Violet bars represent the efficiency criteria of annually and green bars of multi-yearly calibrated model parameters. White numbers refer to the corresponding efficiency criteria, blue numbers to the number of stake measurements available and red numbers to the differences in $R^2$ between annually and multi-yearly calibrated parameters.

### Annually vs multi-yearly calibrated parameters

In general, the performance of TI, HTI, ETI and SEB with multi-yearly calibrated parameters is slightly lower than when using yearly calibrated parameters (Fig. 3.7). However, differences in the efficiency criteria are generally low ($\Delta R^2 \leq 0.04$). An exception is the year 2007 in which the decline of performance is substantial ($\Delta R^2 = 0.09$-$0.36$), especially for SEB and ETI. Another significant performance drop is observed in the case of SEB in the years 2008 and 2010 (dominated by low air temperatures and long lasting snow covers, see Tab. 3.3) with a decrease in model efficiency of 0.08 and 0.09, respectively. Over the entire period, the differences are below 0.04 for TI, HTI and ETI and not significant. In the case of SEB, the difference in $R^2$ is larger, $\Delta R^2 = 0.08$, and thus not negligible. Hence, despite the large variability of the model parameters from year to year (Fig. 3.4), it seems that only a small decrease in model performance is associated with the use of multi-yearly calibrated parameters.

## 3.4.3 Multi-decadal modelling: 1929-2012

In order to validate the long-term performance of the different melt models and to assess differences in their reaction to variable climatic conditions, simulated ice volume changes are compared against observations. Differencing of DEMs of the historical glacier surface provides ice volume changes of six subperiods within 1929-2012. The absolute difference

between modelled and measured ice volume changes and the difference in percentage are chosen to compare observed and simulated values. The DEMs provide an integrated picture of past glacier changes over that period. The first period (1929-1959) is characterized by a general ice volume loss (Fig. 3.8a). The climate over the period of analysis showed both higher and lower air temperatures compared to the mean (results not shown). In the second period (1959-1980), the ice volume has stabilized and in total even a slight increase in the ice volume is observed, likely resulting from decreasing air temperatures towards the early 80s and augmented precipitation amounts. The last four DEM-periods are characterized by a persistent ice mass loss as a consequence of raising air temperatures towards present and decreasing precipitation in the last decade.

The validation of the simulated ice volume changes over the long-term period reveals that the TI and the HTI model have poor performance in comparison to ETI and SEB and clearly differ from the general trend of ice volume evolution indicated by the DEMs (Fig. 3.8). Instead of a glacier retreat, the TI and HTI yield an almost continuous ice volume increase of 116 and $297 \times 10^6\,m^3$ in the period 1929-2012, respectively, in contrast to an actual ice volume loss of $-563 \times 10^6\,m^3$. Particularly in the first and second period, they deviate from the common trend by predicting a strong mass gain. In the former period (1929-1959), the models simulate a substantial volume growth of 101 and $153 \times 10^6\,m^3$ compared to an observed ice volume loss of $-186 \times 10^6\,m^3$ of the same period. In the latter period, measurements show indeed an ice mass gain, but the increase of TI and HTI is 4-5 times larger than observations show. During the subsequent two periods, they show an almost constant ice volume whereas measurements indicate a total ice volume decrease by more than $200 \times 10^6\,m^3$. The only period in which TI and HTI modelled volume changes are very close to measurements are the calibration period and the six following years, with differences of about 0-10% (Fig. 3.8b, c).

In contrast to TI and HTI, the enhanced temperature-index and simple energy-balance model are able to reproduce the general trend of past ice volume changes. Looking at the entire period (1929-2012), ETI results in a total ice volume loss of $-714 \times 10^6\,m^3$ which corresponds, in comparison to a measured volume loss of $-563 \times 10^6\,m^3$, to a misfit of 27%. SEB is closer to the observations with a total modelled volume decrease of $-555 \times 10^6\,m^3$ which is equivalent to a difference of only 1%. However, when considering the individual subperiods, it is evident that deviations from observations are generally smaller for ETI than SEB and that the SEB agreement with observations over the entire period results partly from compensations of over- and underestimations (Fig. 3.8b). Percentage differences for ETI are smaller than 18% with the exception of the period 1959-1980 (where ETI underestimates the glacier growth (–105%)) and the 2000-2007 period, where ETI predicts an enhanced ice volume loss (+45%). SEB leads in general to larger deviations from periodic observations than ETI ranging between 15 and 152%. Only in the second last period, 2000-2007, the ice volume change modelled by SEB is closer to measurements than ETI and differs only by about 15%.

The marked differences between the persistent positive mass balances of the TI and HTI model and the mostly negative or only partly positive mass balances of the ETI/SEB model over the first and second DEM-subperiods are a result of a different model structure. While melt rates of the TI and HTI model are dominated by air temperature fluctuations and experience a decrease of about 20–25% under the colder climate of the first and second DEM-subperiod compared to the calibration period, the melt rates of the ETI model are only reduced by about 12–16%. The reason for the weaker reduction of melt rates in the case of ETI/SEB model is that in these models melt is controlled in about equal shares by temperature and incoming solar radiation. While the mean air temperatures of the first two subperiods are about 0.9-1.0°C lower compared to the calibration period, the mean net shortwave radiation fluxes are

approximately the same ($\pm 5\,W\,m^{-2}$). As a result, the temperature induced melt component of ETI decreases by about 22-25% (as in the case of TI/HTI model) whereas the radiation induced melt component is comparable ($\pm 2\%$) to the values of the calibration period and thus leads to generally higher melt rates under colder climate conditions compared to the TI and HTI model and thus to more negative mass balances.
The performance of the energy-balance model could only be investigated in the period 1991-2012, because the data intense character of the EB approach requires hourly data of numerous meteorological input data in addition to temperature and precipitation which could not be reconstructed for the years prior to 1989. In comparison to the other approaches, the energy-balance model performs significantly worse and yields an ice volume loss of only $-76 \times 10^6\,m^3$ between 1991-2012 which corresponds to 27% of the observed ice volume change of $-286 \times 10^6\,m^3$ (Fig. 3.8). This misfit originates particularly from the first subperiod (1991-2000), where EB simulates an ice volume increase of $76 \times 10^6\,m^3$ while observations show an ice volume loss of $-67 \times 10^6\,m^3$. In the second period, 2000-2007, the EB agrees quite well with the observed ice volume changes (misfit 11%) whereas in the last subperiod, the EB model again underestimates melt (misfit -46%). The lower melt rates of the first and last subperiod are primarily a result of less intense turbulent heat fluxes due to generally lower wind speeds compared to the intermediate period. The largest differences between EB and the other melt models are found in the accumulation area where EB simulates a more positive mass balance due to lower melt rates compared to the empirical models, as the elevation distribution of the mass balance shows (results not shown).

### 3.4.4 Temperature sensitivity

In a future climate an increase in the average global air temperature is expected (IPCC, 2013). Depending on the region and the season, an average temperature increase of $3.4 \pm 0.7\,°C$ by the end of the ongoing century is projected for Switzerland under the A1B emission scenario (CH2011, 2011). In order to test the temperature sensitivity of the different melt models we forced them with a fictive raise in air temperature of 2°C linearly increasing in the period 1929-2012. Results show that the simple and Hock's temperature-index models, directly relating melt rate to temperature through a proportionality factor, react in the strongest manner to a temperature increase (Tab. 3.4). This oversensitivity to temperature had been suggested earlier, but only a the point scale (Pellicciotti et al., 2005). The simple TI model yields a 2.3 larger ice volume change between 1929 and 2012 compared to the observed ice volume change as a response to the changed temperature regime, whereas HTI shows a 2.5 larger ice volume change. ETI and SEB show less strong reactions to the temperature alterations, with volume losses that are higher than the present by 1.8 times. However, the temperature sensitivity of ETI and SEB depends on the choice of the melt model parameters controlling the proportion of temperature and solar radiation induced melt.

## 3.5 Discussion

### 3.5.1 Model performance over the multi-year period

During the six years of the calibration period, all models perform in a similar manner in comparison with the mass balance measurements. The HTI has marginally higher efficiency criteria than TI, ETI and SEB. In contrast to the other models, the HTI model contains three adjustable parameters which might favor its performance compared to the other models. These

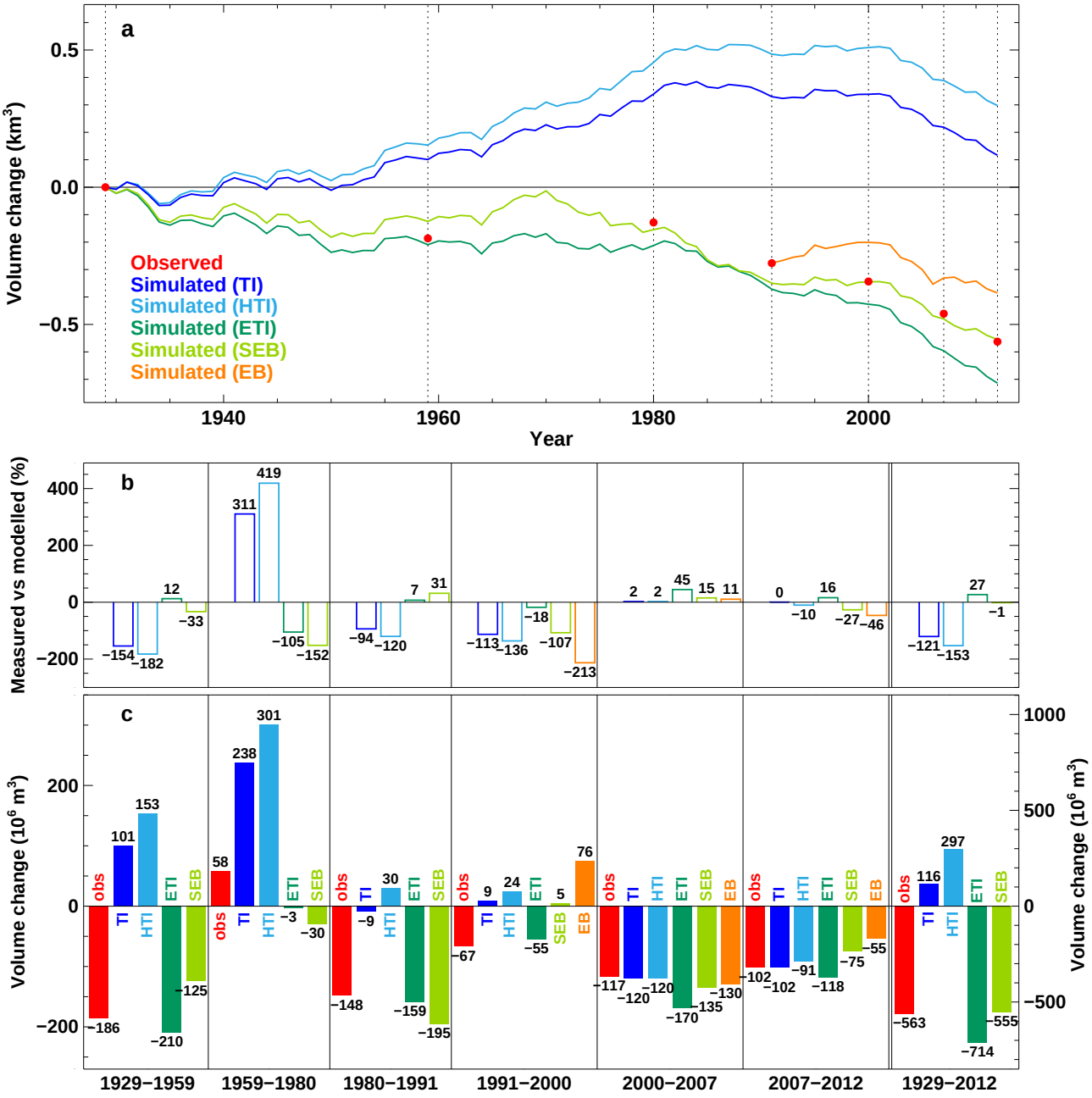


Figure 3.8: Figure (a) shows the evolution of the ice volume changes in the course of the years 1929-2012. The solid blue and green curves refer to the simulated volume changes derived by TI, HTI, ETI and SEB. The medium and light green dotted lines correspond to the ice volume changes of ETI and SEB with the original parameter values (see Discussion). The red dots indicate the inferred ice volume changes from available DEMs. Figure (c) shows the observed and modelled ice volume changes of the six DEM-subperiods and the entire period 1929-2012 by the red and blue/green bars. Black numbers indicate the ice volume change in $10^6$ m$^3$. The axis on the right extends over a larger range and refers to the ice volume change over the entire period 1929-2012. Differences in percentage of modelled compared to measured ice volume changes are displayed in Figure (b). The orange line and bars refer to the ice volume changes derived by EB limited to last three subperiods.

Table 3.4: The ice volume changes over the period 1929-2012 for the different melt models with (i) an unaltered temperature forcing ($\Delta V$) and (ii) superimposing a temperature rise of 2 °C ($\Delta V_{+2°C}$), and the absolute and relative difference compared to the observed ice volume change ($\Delta V - \Delta V_{+2°C}$).

| Model | $\Delta V$ [$10^6$ m$^3$] | $\Delta V_{+2°C}$ [$10^6$ m$^3$] | $\Delta V - \Delta V_{+2°C}$ [$10^6$ m$^3$] | $\Delta V - \Delta V_{+2°C}$ [%] |
|---|---|---|---|---|
| TI | 116.3 | -1199.6 | 1315.9 | -234 |
| HTI | 297.5 | -1113.0 | 1410.5 | -251 |
| ETI | -713.8 | -1753.5 | 1039.7 | -185 |
| SEB | -554.6 | -1576.5 | 1021.9 | -182 |

findings contradict the results of Pellicciotti et al. (2005) who obtained better performance of the enhanced compared to the temperature-index model. The reason for this disagreement might be found in the different model setups. While Pellicciotti et al. (2005) performed the analysis at the point scale with measured meteorological data and compared model results against hourly melt rates, we used extrapolated data from a weather station outside the glacier and calibrated to weakly to monthly mass balance measurements. Hence, uncertainties in the model input data and the coarser resolution of calibration data might blur differences in performance between HTI and ETI over the multi-year period.

Choosing multi-yearly calibrated to yearly calibrated parameter values entails only a small drop in model performance over the multi-year period except in 2007, in particular for ETI and SEB. A possible reason for these discrepancies might be a failure of the cloud factor parameterisation. According to our model, days with clear-sky conditions ($cf > 0.8$) prevail in 2007 compared to the other years. If modelled incoming solar radiation is compared to measurements it is evident that the cloud factor parameterisation results in erroneous high incoming solar radiation. Consequently, smaller melt coefficients are obtained in order to compensate the overestimated radiation flux and thus, the application of multi-yearly calibrated parameters leads to too high melt rates and therefore to a larger disagreement.

The analysis of the climatic conditions shows that parameter variations over the 6-year period are not arbitrary, but are controlled by the characteristics of the ablation season. The 6-year period cover a wide range of climatic conditions and provide us with a selection of distinct climate conditions. Hence, it seems to be important that the calibration of melt parameters is based on several years of mass balance data in order to balance the characteristics of single years and get reasonable simulations for long-term modelling.

### 3.5.2 Model performance over decadal periods

There is general agreement that physically based energy-balance models represent best melt processes and thus should provide the best simulations of melt rates. While this has been established at the point scale (Pellicciotti et al., 2005, 2008; Andreassen et al., 2008), it is less clear for application at the glacier and catchment scale. Our study has shown that the EB model performance is inferior to that of the simpler ETI and SEB models when validated against mass balance observations over several years. The model performs well against ice volume changes in the years 2000-2007, but not in the period 1991-2000. The reason for

the poor results of the EB model over the long-term, despite the physical basis of the model, might be found in the type of input data. The EB model was forced with data of an off-glacier weather station due to lack of on-glacier data. However, fluxes at the glacier-atmosphere interface refer to the exchange of heat in the glacier boundary layer, i.e. the layer of atmosphere affected by the presence of a cold surface at zero degrees and presence of katabatic flow. Air temperature, wind speed and relative humidity measured at an off-glacier site might therefore not be appropriate to represent those in the glacier boundary layer. In our study, the different components of the energy balance are either extrapolated from the weather station or parameterized. Air temperature in particular was extrapolated from the off-glacier Grimsel weather station. Recent studies have suggested that the temperature regime over glaciers may substantially differ from that on-glacier (e.g. Petersen et al., 2013), so that such extrapolation might not be accurate enough for energy balance modelling. In the same way, the TI and HTI model, being strongly and only dependent on air temperature, might be more affected by errors in this variable.

The difficulties experienced by TI and HTI to model the long-term glacier evolution indicate that the relationship between temperature and melt is not constant in time and depends on the prevailing climate conditions. Particularly, the positive ice volume changes of the first two periods (1929-1959 and 1959-1980), where air temperatures were lower compared to the subsequent periods, demonstrate that the parameters calibrated to present conditions are not valid in a colder climate. This is further supported by the fact that TI and HTI lead to reliable ice volume changes only in the two very recent periods (2000-2007 and 2007-2012), one being the calibration period. Our findings are in accordance with the results of Huss et al. (2009b) which showed that degree-day factors are not stable for long-term and were clearly higher in the 1920-70s compared to present values. These results confirm that recalibration of model parameters to individual subperiods is essential as already shown in Huss et al. (2009a) to reconstruct long-term mass balance time series and support our findings of too positive mass budget in the first two periods.

The separation of temperature and solar radiation induced melt leads to major improvements in terms of the stability of the model parameters. This is reflected by the considerably better performance of ETI and SEB over the long-term period. Our results seem to suggest that the relationship between air temperature/solar radiation and melt rates remains constant over time in the face of climate variations. Nonetheless, certain deviations from measurements remain. While the SEB model fits better to the overall ice volume change over the period 1929-2012, ETI comes closer to the ice volume changes of the individual subperiods.

A main difference between the TI and SEB models (and the only one between the ETI and SEB models) is the use of a threshold temperature for melt to occur: while the TI models employ a threshold temperature, in the SEB melt occurs only when the sum of the terms is positive. This leads to situations in which the SEB model simulates melt at air temperature below the threshold temperature, which occurs particularly during days in winter or spring with high incident solar radiation. In contrast to this, in other cases the SEB model simulates no melt while air temperatures are above the threshold, which is generally observed during warm nights in summer. The effect of these two phenomena on total melt is in the range of a few percent, with the latter effect slightly overweighting the former one. Thus, this difference in model structure does not seem to have a significant impact on the mass balance. It is rather the separation of solar radiation and temperature-induced melt that leads to an improvements in long-term simulations by reducing the oversensitivity to temperature.

### 3.5.3 Parameters robustness

The poor performance of ETI with the original parameter values (see Fig. 3.5) proposed by Pellicciotti et al. (2005) indicates that site-specific recalibration of model parameters is required for applications over several decades. Despite a relatively small drop in model performance over the multi-year period ($\Delta R^2 = 0.06$, results not shown), the effect on the long-term modelling is not negligible and results in a misfit between simulated and observed ice volume changes of 59% (Fig. 3.8a). Similar considerations apply to the SEB model. Assuming the parameter $C_1$ equal to $10\,\mathrm{Wm^{-2}\,K^{-1}}$ as suggested by Oerlemans (2001) and adjusting only parameter $C_0$ by means of the mass balance measurements of the multi-year period ($C_0 = -39\,\mathrm{Wm^{-2}}$) reveals that a parameter combination with a fixed $C_1$ value leads to too negative mass mass balances on average, with a difference in the total ice volume change (1929-2012) of 87% compared to observations (Fig. 3.8a). Hence, our results suggest that recalibration of both the ETI and SEB model parameters to local conditions is required in order to reproduce correctly the observed ice volume evolution over multi-decadal periods. However, once the parameters are recalibrated for the specific site they seem to be robust over the long-term. These results do not rule out the possibility that for settings where meteorological conditions are better known (data of a weather station on-glacier) the original parameters might lead to greater agreement with observed glacier changes even over the long-term.

### 3.5.4 Other model comparison studies

Few studies have compared the performance of melt models of different complexity and assessed their transferability in space and time. The analyses are generally carried out at the point scale and are, to our knowledge, all limited to a few ablation seasons. Pellicciotti et al. (2005) compared the performance of the enhanced temperature-index model with three temperature-index models at the point scale and showed that the enhanced temperature-index model had a better performance compared to the other models. The study of Essery et al. (2013), which applies a snow model in 1701 different configurations to a well-instrumented site over four ablation seasons, support this finding by concluding that well-established empirical models achieve similarly good performance as more physically based models. At the glacier-scale results are less clear. Pellicciotti et al. (2013) showed that there were small differences in performance between the enhanced temperature-index (ETI) model and an energy-balance model when applied in a distributed manner to a glacier in the Chilean Andes in the ablation area. However, differences were substantial in the upper sections of the glacier, where lack of data prevented a sound assessment of which model best reproduced ablation rates. The analysis of MacDougall et al. (2011) applying a distributed energy-balance model and four empirical models to two glaciers and two seasons in the St. Elias Mountains (Canada) came to a similar conclusion, but in addition showed that energy-balance models have highest transferability in time. Our study is the first attempt at evaluating the long-term performance of several melt model approaches with different complexities and compared their performance over a period of more than 80 years. We have shown that comparison over short periods might not provide insight enough into reasons of model failures such as parameters instability. Particularly with regard to glacier projections into the future, the presented results might be important since recent studies have shown that the type of melt model affects runoff projections (Huss et al., 2014; Kobierska et al., 2013).

## 3.6 Conclusions

This study has examined the long-term performance of five well-established melt models: (1) a classical temperature-index melt model, (2) the temperature-index melt model by Hock (1999), (3) an enhanced temperature-index model, (4) a simplified energy-balance model and (5) a full energy-balance model. The melt models were coupled to an accumulation model and a model for the evolution of the glacier surface geometry in order to simulate in a distributed manner the ice volume evolution of Rhonegletscher (Switzerland) in the period 1929-2012. Meteorological time series of a nearby weather station were used to force the mass balance models. Subseasonal mass balance measurements of the years 2006-2012 were used for the calibration of the parameters of the empirical melt models. Observed ice volume changes of six subperiods between 1929-2012 served for model validation.
From our comparative study the following conclusions can be drawn:

1. The performance of the different melt models over the multi-year period (2006-2012) is very similar when parameters are calibrated to the prevailing climate settings and the local conditions except for the energy-balance model, which shows less consistency with the stake readings compared to the other approaches.

2. The calibration of model parameters to each single year of the multi-year period showed that the parameters strongly fluctuate from year to year independently from the model type (except TI). These variations originate from an equifinality problem, i.e. different parameter sets leading to equally good model performance. Discrepancies among the parameter combinations emerge only in the daily cycle of melt rates. However, despite the high parameter variability from year to year, the performance with multi-yearly calibrated parameter values entails only a small decrease in model performance over the multi-year period in comparison to yearly calibrated parameters.

3. Model results over the multi-decade period (1929-2012) suggest that only the enhanced temperature-index and the simplified energy-balance model can reproduce the observed ice volume changes. This implies that the melt relationship of those two models remain stable over time. It is interesting to notice that under the conditions of our study the models of intermediate sophistication seem to have the best performance over the long-term and to be best suited for long-term simulations in comparison to both the energy-balance model and the conceptual temperature-index model.

4. The classical and Hock's temperature-index model are only able to reproduce the ice volume changes of the most recent (calibration) subperiods with sufficient accuracy. In the preceding periods, the models simulate too positive mass balances and a sustained glacier growth. This result indicates that the relationship between melt and temperature changes over time, in response to changes in the magnitude of the energy fluxes that temperature can only partially account for. This implies that the parameters of the temperature-index models are not robust in time and require recalibration for distinct climate conditions (Huss et al., 2009b).

5. The energy-balance model shows the poorest performance among all melt models despite its physical character. It predicts a too positive mass budget. The reason for the failure might be found in the forcing of the model with data of an off-glacier weather station, while the energy balance is based on knowledge of heat fluxes exchanged in the glacier boundary layer that are therefore likely to be poorly predicted by variables measured far

away on non-glacierised ground. Inadequate input data could thus result in erroneous melt simulations.

The separation of temperature and solar radiation induced melt seems to lead to rather stable model parameters over time and to make those models suitable for long-term modelling in the future. Particularly with regard to future projections, the use of appropriate melt approaches is crucial to provide reliable glacier projections. The results obtained for Rhonegletscher should be confirmed with a comparable study on other glaciers for which the necessary data are available.

**Acknowledgements**

Many thanks go to all those who helped to collect the numerous mass balance and snow depth measurements at Rhonegletscher in various field campaigns. Meteorological data were provided by MeteoSwiss and topographic maps by Swisstopo. H. Boesch extracted digital elevations models from aerial photographs and B. Nedela digitalized a topographic map. We sincerely thank Matthias Huss for the constructive comments. We also thank the chief and scientific editor, J. Jacka and B. Kulessa, and the two reviewers for their helpful comments and suggestions. This work was supported by the NRP61 project.

# Chapter 4

# The impact of Saharan dust and black carbon on albedo and long-term mass balance of an Alpine glacier

J. Gabbi[1], M. Huss[1,2], A. Bauder[1], F. Cao[3,4] and M. Schwikowski[3]

[1]Laboratory of Hydraulics, Hydrology and Glaciology (VAW), ETH Zürich, Zürich, Switzerland.
[2]Department of Geosciences, University of Fribourg, Fribourg, Switzerland
[3]Paul Scherrer Institute (PSI), Villigen PSI, Switzerland
[4]Guangzhou Institute of Geochemistry, Chinese Academy of Sciences, Guangzhou, China

Published, The Cryosphere Discussions

**Citation** Gabbi J., M. Huss, A. Bauder, F. Cao and M. Schwikowski (2015). The impact of Saharan dust and black carbon on albedo and long-term mass balance of an Alpine glacier. *The Cryosphere Discussions*, 9(1), 1133–1175.

**Abstract**

Light-absorbing impurities in snow and ice control glacier melt as shortwave radiation represents the main component of the surface energy balance. Here, we investigate the long-term effect of snow impurities, i.e. mineral dust and black carbon (BC), on albedo and glacier mass balance. The analysis was performed over the period 1914–2014 for two sites on Claridenfirn, Swiss Alps, where an outstanding 100-year record of seasonal mass balance measurements is available. Information on atmospheric deposition of mineral dust and BC over the last century was retrieved from two firn/ice cores of high-alpine sites. A combined mass balance and snow/firn layer model was employed to assess the effects of melt and accumulation processes on the impurity concentration at the surface and thus on albedo and glacier mass balance. Compared to pure snow conditions, the presence of Saharan dust and BC lowered the mean annual albedo by 0.04–0.06 depending on the location on the glacier. Consequently, annual melt was increased by 15–19% and the mean annual mass balance was reduced by about 280–490 mm w.e. BC clearly dominated absorption which is about three times higher than that of mineral dust. The upper site has experienced mainly positive mass balances and impurity layers were continuously buried, whereas at the lower site, surface albedo was more strongly influenced by re-exposure of dust and BC-enriched layers due to frequent years with negative mass balances.

## 4.1 Introduction

Deposition of mineral dust and BC have a fundamental impact on the energy balance of glaciers and snow-covered areas by increasing the absorption of solar radiation. Along with the enhanced melting due to the darkening of the snow surface, the growth of snow grains is accelerated, which further reinforces snow melt rates (Painter et al., 2007). While light-absorbing impurities control the snow albedo mainly in the visible wavelengths, the snow grain size affects the albedo in the near-infrared. Shortwave radiation is the dominant energy source for melting of snow, firn and ice, and consequently the surface albedo has an important influence on the mass budget of glaciers (Oerlemans et al., 2009).
Repeated years with negative glacier mass balances lead to a shift in the equilibrium line to higher elevations and to the re-exposure of dust and BC-enriched firn layers at the surface. Snow impurities are mainly retained at the surface during conditions of melt and surface concentrations might be enhanced by up to one order of magnitude resulting in a pronounced melt amplification (Sterle et al., 2013).
Absorptive impurities consist of mineral dust, carbonaceous particles and coloured organic matter (Warren, 1984). Advection of dust-loaded air masses from the Saharan desert leads to episodic deposition of large amounts of mineral dust in the Alps. Analyses of firn cores from high-alpine sites, resolving the signal of the continental background aerosols, indicated that long-range transported crustal impurities account for about two thirds and local impurities for about one third of the total mineral dust deposited (Wagenbach and Geis, 1989). One single Saharan dust deposition event may even supply 30% of the total annual dust budget at high-altitude mountain glaciers (Schwikowski et al., 1995). Most prominent Saharan dust episodes in the Alpine region occurred in the years 1936/37, 1977, 1990 and 2000 leaving marked dust horizons in firn/ice cores (Schwikowski et al., 1995; Jenk et al., 2009; Sigl, 2009).
BC refers to the strongly light-absorbing component of soot and is emitted naturally and anthropogenically by incomplete combustion of fossil fuels and by biomass burning. BC has become a focus of interest as it has been identified recently as one of the major contributors to global climate change (Ramanathan and Carmichael, 2008; Bond et al., 2013). BC contributes to global warming by absorption of sunlight, firstly when it is suspended in the atmosphere, and secondarily when it is deposited on snow and ice by reducing the albedo and hence accelerating melting. Along with the beginning of the industrialisation, global BC emissions sharply increased and continued to rise into the 21th century. In the European region, BC concentrations started to decrease since mid-20th century and have stabilised over the last few decades (Bond et al., 2007).
Recently different studies investigated the impact of light-absorbing impurities on snow albedo and melting of snow. Based on a 10-year record of mineral dust and BC concentrations, retrieved from an ice core at Mera Peak, Nepalese Himalaya, Ginot et al. (2014) found that light-absorbing particulates cause up to 26% of the total annual surface melting. Another study performed at Mera Peak shows that mineral dust dominates absorption and may reduce the albedo of snow by up to 40% (Kaspari et al., 2014). Investigations for the Colorado River Basin, Western US, show that the radiative forcing of mineral dust deposition may shorten the duration of snow cover by several weeks (Skiles et al., 2012) and also affects the timing and magnitude of runoff (Painter et al., 2010). It was suggested that increasing anthropogenic emissions of black carbon during the Industrial Revolution have forced the end of the Little Ice Age in the Alps (Painter et al., 2013).
In this study we assess the significance of natural mineral dust and anthropogenic BC particles in snow and firn on the mass balance of a high-mountain glacier over a centennial period

(1914–2014). Using a unique 100-year record of seasonal glacier mass balances, ice core records of past atmospheric deposition of Saharan dust/BC and a sophisticated modelling approach, we examined the contribution of light-absorbing impurities to glacier melt for (1) a site with accumulation conditions over the entire period, where dust is predominately buried by winter snow, and (2) a site at the glacier's equilibrium line involving a re-exposure of buried dust and BC layers at the surface in years with negative mass balance. We have chosen Claridenfirn (Swiss Alps) for which the worldwide longest data series of seasonal glacier mass balance exist. This comprehensive data set enables an accurate and field data-based simulation of ablation and accumulation processes. In order to simulate the feedback between melt, accumulation and snow impurities, a mass balance model was coupled with a snow density model, which tracks the position and the thickness of deposited snow layers and impurities. The mass balance model incorporates an enhanced temperature-index melt model including the shortwave radiation balance and a parameterisation for albedo, which is based on the specific surface area of snow and the impurity concentration in the surface snow.

## 4.2 Study site & Data

Claridenfirn is a mountain glacier with an area of approximately 5 $km^2$ and is located on the northern Alpine Ridge of the Swiss Alps. The glacier is exposed to the southeast and covered an elevation range of 2540 to 3267 m a.s.l. in 2003 (Fig. 4.1).

First mass balance measurements date back to 1914 and provide a unique data set covering a period of 100 years. At two different sites, at a *lower* stake (2680 m a.s.l.) and an *upper* stake (2890 m a.s.l.), winter, summer and annual mass balance have been measured every year using stakes and snow pits in mid-May and end of September, respectively. Simultaneously snow density measurements in snow pits have been carried out. The measurements at Claridenfirn are the longest continuous glacier mass balance observations worldwide. More details about the monitoring programme on Claridenfirn are provided by Müller and Kappenberger (1991) and Huss and Bauder (2009).

The forcing of the mass balance model requires daily air temperature and precipitation data for 1914–2014. We used air temperature recorded by the MeteoSwiss weather station Säntis (2490 m a.s.l.), the closest station with long-term records and homogenized time series (Fig. 4.1, Begert et al., 2005). Monthly air temperature lapse rates were derived by comparison of nearby weather stations to transpose the temperature to the elevation of the study sites. Time series of daily precipitation were taken from a local weather station, Elm (965 m a.s.l.), situated at a distance of 22 km from Claridenfirn (Fig. 4.1).

Furthermore, our model requires daily time series of incoming shortwave radiation that were derived from a simple parameterisation based on daily temperature ranges (see *Methods*). Daily maximum and minimum temperature were provided from the MeteoSwiss weather station at Davos over the period 1914–2014 (Fig. 4.1). For calibrating the parameterisation, daily values of incoming solar radiation of 1981–2014 recorded at the same station were used. In addition, a unique data set of monthly means of global solar radiation for Davos, covering the period 1936–2014, is provided by the Global Energy Balance Archive (GEBA; Ohmura et al., 1989), and was employed to improve the performance of the cloud factor parameterisation.

A firn/ice core from the cold glacier saddle of Colle Gnifetti (4455 m a.s.l., Monte Rosa, Switzerland), retrieved in 2003, provides a continuous record of annual iron (Fe) concentrations over 1914–1997 (Sigl, 2009), which was used to infer the mineral dust concentration in precipitation (Fig. 4.2a). For the years 1998–2007, which are not covered by the Fe data,

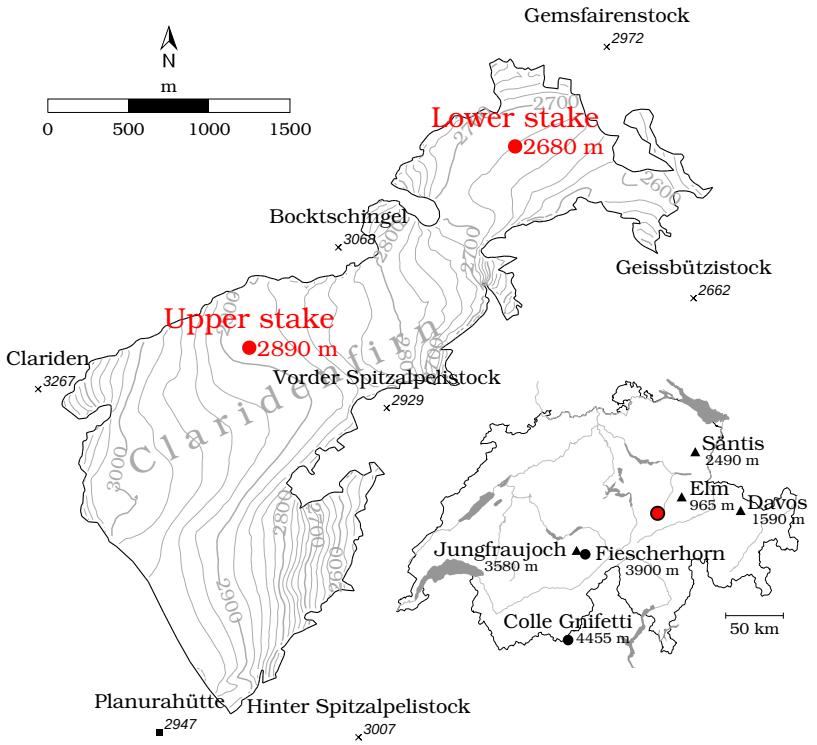


Figure 4.1: Study site overview. The red dots on Claridenfirn indicate the lower and the upper stake. The inset shows the location of the study site within Switzerland (red point), of the ice core sites Colle Gnifetti and Fiescherhorn (black dot). The aerosol measurement station Jungfraujoch and the weather stations used to derive meteorological time series (black triangles) are indicated.

the Fe concentration was derived from the calcium record, extending the 2003 data set with a shallow core collected at the same site in 2008 (Sigl, 2009), taking advantage of the high correlation between the two dust tracers. Concentrations of BC were obtained from a firn/ice core from Fiescherhorn (3900 m a.s.l., Bernese Alps, Switzerland) drilled in 2002 (Fig. 4.2a; Jenk et al., 2006). This core provides mean yearly concentrations of elemental carbon (EC) over the period 1914–2002, which can be used as proxy for BC, as EC and BC are constituted of the same fraction of carbonaceous particles (Lavanchy et al., 1999). For BC and mineral dust concentrations of the years 2002-2014 and 2007-2014, respectively, which are not covered by the ice core data, a mean concentration averaged over the entire period was assigned (Fig. 4.2a). Furthermore, daily BC aerosol measurements of Jungfraujoch (3580 m a.s.l., Fig. 4.1) conducted in the frame of the Global Atmosphere Watch (GAW) monitoring programme, covering the period 1995–2000, were used to derive an annual cycle of BC concentrations in the atmosphere.

## 4.3 Methods

In order to determine the impact of Saharan dust events on surface albedo and glacier melt, a mass balance model including a parameterisation for snow, firn and ice albedo was coupled with a snow/firn density model to track the position and thickness of the snow layers and dust. The physical albedo parameterisation is based on the evolution of the specific surface

area of snow grains and includes the option to simulate the effect of snow impurities on pure snow albedo. Atmospheric input of mineral dust and BC was derived based on the ice/firn core data. The mass balance model was forced by daily time series of air temperature, precipitation and incoming shortwave radiation and was run over a 100-year period (1 October 1914 to 30 September 2014). Hereafter, the data series of mineral dust and BC and the individual components of the employed mass balance and snow density model are described in detail.

### 4.3.1 Input of mineral dust & black carbon

#### Mineral dust

The absorption of mineral dust in the visible spectrum is highly sensitive to the content of iron oxides. Kaspari et al. (2014) determined light-absorption of mineral dust in snow and ice of a Himalayan glacier based on gravimetrically determined Fe concentrations. Accordingly, we used records of iron (Fe), provided by the ice core, to infer mineral dust concentrations. Iron oxides mainly consist of the minerals goethite and haematite (Sokolik and Toon, 1999; Lafon et al., 2006). Since they have different light absorption spectra (e.g. Lafon et al., 2006) their relative proportion has to be known for calculating the radiative properties of dust. According to Shi et al. (2011) the mass ratio of the mineral haematite to the minerals haematite plus goethite for Saharan dust is 0.42 on average. Based on the assumption that about 45–64% of the total Fe is encompassed in light-absorbing oxides (Lafon et al., 2004), the mass of goethite and haematite is calculated following Kaspari et al. (2014) and used as proxy for the absorption of mineral dust.

Most of the dust peaks can be related to long-range transported crustal impurities, which account for about 70% of the total deposited mineral dust (Wagenbach et al., 1996). This is a conservative assumption since local dust contains a lower portion of Fe-oxides. We therefore assume that all mineral dust is made up by Saharan dust.

Errors in the annual layer counting of the ice cores might involve uncertainties of $\pm$1-2 years (Eichler et al., 2000). However, we consider this having a minor impact on mass balance simulations since dates of intense Saharan dust events are well known and smaller events might have a minor effect on average mass balance over a 100-year period.

The annual amount of mineral dust (i.e. Fe-oxide) was distributed over the year according to the Saharan dust climatology reported by Collaud Coen et al. (2004). They analysed the number and duration of Saharan dust events per month based on measurements of the aerosol scattering coefficient performed at Jungfraujoch in the years 2001 and 2002. Higher probability of occurrence was observed in the March–June and the October–November period. Extended time series of the years 2001–2012 confirm this distribution (MeteoSwiss, 2014a). Three different classes of Saharan dust events were defined: Saharan dust events lasting between 4 and 10 h, between 10 and 24 h and longer than 24 h. The inferred average distribution of the number of events per month and the mean duration of each class were scaled by the annual dust concentrations obtained from the ice core analysis in order to derive daily atmospheric deposition rates of Saharan dust.

Days within a month were randomly selected except for extraordinarily large events of the years 1936, 1977, 1990 and 2000 for which the date of deposition is exactly known from literature (SMA-Annalen, 2014; Prodi and Fea, 1979; Schwikowski et al., 1995). We assigned 30% of the total annual dust amount to these extraordinary large events according to Schwikowski et al. (1995).

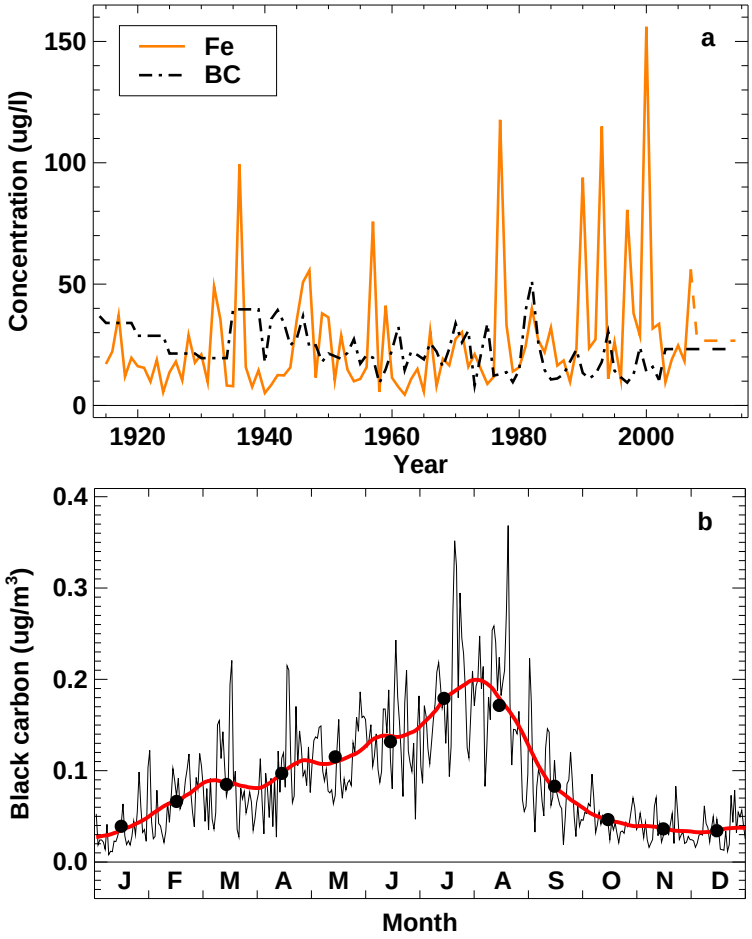


Figure 4.2: (a) Concentrations of Fe (Sigl, 2009) and BC (inferred from EC; Jenk et al., 2006) over the period 1914–2014 retrieved from the Colle Gnifetti and Fiescherhorn ice core, respectively (Fig. 4.1). (b) Mean annual cycle of BC concentrations in the atmosphere measured by GAW at Jungfraujoch averaged over the years 1995–2000. Dots refer to the monthly means and the solid red line refers to the running mean.

### Black carbon

While Saharan dust transport has an episodic character, deposition of BC is controlled by seasonal variations in atmospheric stability, which is higher in winter than in summer. In order to mimic the yearly cycle of BC input, daily ambient BC measurements at Jungfraujoch, performed in the frame of the GAW monitoring programme, were used. Based on these measurements, daily anomalies averaged over the period 2002–2013 were derived and applied to the annual BC concentrations provided by the firn/ice core in order to infer daily atmospheric deposition rates of BC (Fig. 4.2b).

### Scaling to study site

Several studies performed detailed investigations of the regional and altitudinal distribution of major ions in the high Alpine region (e.g. Nickus et al., 1997; Rogora et al., 2006). They found a marked regional variability but no clear trends, neither in distance nor in altitude. Due to a lack of clear indication, we assumed that Fe/BC concentrations at Claridenfirn are in a similar range as the concentrations observed on Colle Gnifetti and Fiescherhorn, respectively,

and employed measured Fe/BC concentrations directly without a transfer function. In order to estimate the influence of potential differences in their input concentration we performed a sensitivity analysis (see *Discussion*).

### 4.3.2 Mass balance model

For simulating snow and ice melt, the enhanced temperature-index (ETI) model (Pellicciotti et al., 2005) was employed. This model computes melt as a function of air temperature and shortwave radiation and accounts for the effects of albedo and cloudiness on melting:

$$M = \begin{cases} \mathrm{TF}\, T_\mathrm{a} + \mathrm{SRF}(1-\alpha)\, G & : \quad T_\mathrm{a} > T_\text{ø} \\ 0 & : \quad T_\mathrm{a} \leq T_\text{ø} \end{cases} \tag{4.1}$$

where $T_\mathrm{a}$ is the air temperature, TF ($\mathrm{mm\,d^{-1}\,{}^\circ C^{-1}}$) and SRF ($\mathrm{mm\,m^2\,d^{-1}\,W^{-1}}$) are the tuning parameters, $\alpha$ the surface albedo and $G$ the global incoming shortwave radiation ($\mathrm{W\,m^{-2}}$). $T_\text{ø}$, the threshold temperature above which melt occurs, is set to 0 °C. $G$ is calculated from a cloud transmissivity factor, cf, and the clear-sky incoming solar radiation, the latter based on the approaches by Iqbal (1983) and Corripio (2003).
Snow accumulation was computed by the station precipitation and a correction factor, $c_\mathrm{prec}$, accounting for the elevation difference between the station and the glacier and gauge undercatch. A threshold temperature of 1.5°C with a linear transition range of ±1.0°C was applied to calculate the occurrence of solid and/or liquid precipitation.

#### Cloud factor parameterisation

The cloud transmissivity factor, cf, accounts for the attenuation of solar radiation by clouds and is derived as a function of daily temperature ranges ($\Delta T$, Pellicciotti et al., 2011):

$$\mathrm{cf} = d_1\, \Delta T + d_2. \tag{4.2}$$

The two coefficients, $d_1$ and $d_2$, were derived by linear regression of the daily air temperature range and the difference between actual and potential clear-sky incoming solar radiation. Using the weather station data from Davos (Fig. 4.1), parameters were calibrated over the period 1981–2013. Monthly means of global solar radiation of 1936–2014 allowed verifying the performance of the cloud factor parameterisation over decadal periods. Despite the simplicity of the approach, simulated shortwave radiation agreed well with observations (Fig. 4.3). During the 1940s, when very high incoming solar radiation was recorded, the cloud factor parameterisation, however, exhibited difficulties in reproducing the observations. In order to obtain as reliable as possible radiation values in daily resolution, the monthly averages of daily incoming shortwave radiation derived from the cloud factor parameterisation were adjusted to match the monthly means measured at Davos for the years with data (i.e. 78% of the study period, Fig. 4.3).

### 4.3.3 Albedo model

Snow albedo was derived according to the physical snow albedo parameterisation by Gardner and Sharp (2010) as the sum of pure snow albedo and its change due to impurities. The albedo of ice was kept constant at 0.2 (Pellicciotti et al., 2005). Pure snow albedo, $\alpha_\mathrm{SSA}$, is calculated as a function of the specific surface area, SSA, of snow as

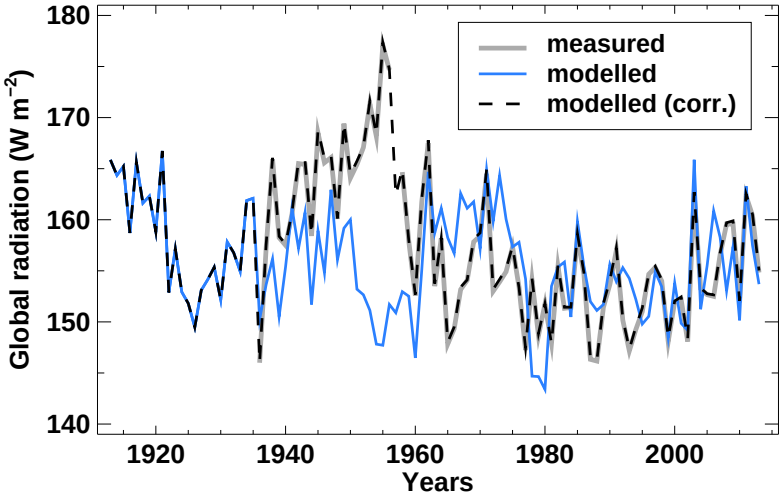


Figure 4.3: Comparison of mean annual global radiation measured at Davos (bold grey, 1936–2014) and global radiation modelled by the cloud factor parameterisation (blue). The dashed black line shows annual averages of modelled daily radiation adjusted by the measurements to fit measured monthly means which are used to force the mass balance model.

$$\alpha_{\mathrm{SSA}} = 1.48 - \mathrm{SSA}^{-0.07}. \tag{4.3}$$

Details on the calculation of SSA are given below. The change in pure snow albedo due to loading of light-absorbing impurities is derived according to

$$d\alpha_{\mathrm{C}} = \max\Big(0.04 - \alpha_{\mathrm{SSA}}, \frac{-C^{0.55}}{0.16 + 0.6\mathrm{SSA}^{0.5} + 1.8C^{0.6}\mathrm{SSA}^{-0.25}}\Big), \tag{4.4}$$

where $C$ is the concentration of BC in mg kg$^{-1}$ (Gardner and Sharp, 2010). In order to model the effect of mineral dust on snow albedo, the mineral dust (i.e. Fe oxides) was converted to optically equivalent concentrations of light-absorbing carbon using mass absorption coefficients (MACs) of BC and Fe oxides of 6.8 m$^2$ g$^{-1}$ and 0.56 m$^2$ g$^{-1}$, respectively (Alfaro et al., 2004; Kaspari et al., 2014). The direct-beam albedo of the impurity-loaded snow is then obtained as $\alpha = \alpha_{\mathrm{SSA}} + d\alpha_{\mathrm{C}}$. The effect of the solar zenith angle on the albedo is not considered as the model runs on daily basis.

### SSA model

The specific surface area of the snow grains was calculated relying on the approach by Roy et al. (2013) that considers both dry and wet snow metamorphism. In the case of dry snow conditions, the evolution of SSA is computed according to Taillandier et al. (2007), as a logarithmic function of snow age and snow temperature, $T_{\mathrm{snow}}$, as

$$\begin{aligned}\mathrm{SSA}(t) = {} & [0.629 \cdot \mathrm{SSA}_{\mathrm{initial}} - 15.0 \cdot (T_{\mathrm{snow}} - 11.2)] \\ & -[0.076 \cdot \mathrm{SSA}_{\mathrm{initial}} - 1.76 \cdot (T_{\mathrm{snow}} - 2.96)] \\ & \cdot \ln\Big\{t + e^{\frac{-0.371 \cdot \mathrm{SSA}_{\mathrm{initial}} - 15.0 \cdot (T_{\mathrm{snow}} - 11.2)}{0.076 \cdot \mathrm{SSA}_{\mathrm{initial}} - 1.76 \cdot (T_{\mathrm{snow}} - 2.96)}}\Big\}.\end{aligned} \tag{4.5}$$

The approximation by Brun (1989) is used to simulate the evolution of snow grains under wet conditions with respect to the liquid water content of the snowpack. The growth of the optical radius of snow, $\Delta R_{\text{opt}}$ ($\text{mm}\,\text{d}^{-1}$), is calculated as

$$\Delta R_{\text{opt}} = \frac{C_1 + C_2 \cdot \theta^3}{R_{\text{opt}}^2 \cdot 4\pi}, \tag{4.6}$$

where $C_1 = 1.1 \times 10^{-3}\,\text{mm}^3\,\text{d}^{-1}$ and $C_2 = 3.7 \times 10^{-5}\,\text{mm}^3\,\text{d}^{-1}$ are empirical coefficients and $\theta$ is the liquid water content in mass percentage. The SSA decrease is more pronounced when $\theta$ increases. If the liquid water content is greater than zero, the model-derived SSA value is converted into its equivalent optical radius, $R_{\text{opt}}$, with

$$R_{\text{opt}} = \frac{3}{\rho_{\text{ice}} \cdot \text{SSA}}, \tag{4.7}$$

where $\rho_{\text{ice}}$ is the density of ice. Then, Eq. (4.6) is applied and $R_{\text{opt}}$ is reconverted to SSA using Eq. (4.7). The initial SSA was set to $73.0\,\text{m}^2\,\text{kg}^{-1}$ (Domine et al., 2007). Following Taillandier et al. (2007), a minimal SSA value of $8.0\,\text{m}^2\,\text{kg}^{-1}$ was used to avoid unrealistically low values. The liquid water content of the snowpack is provided by a snow density model (see below).

**Snow density model**

A snow densification model is required to determine the position and the thickness of each snow layer. The simple point model by De Michele et al. (2013) for bulk snow density and snow depth was employed and applied to each snow layer. The two-constituent model solves mass balance equations for the dry and liquid mass of the snow pack, as well as momentum balance and rheological equations for the dry part. It results in a system of three differential equations for depth and density of the dry part of the snowpack, and the depth of liquid water. Sublimation and evaporation are not considered. The main characteristics of the model are shortly described in the following. For more detailed information see De Michele et al. (2013). A simplified energetic description of the snowpack assuming thermal equilibrium between constituents is used. The temperature profile, $T_{\text{snow}}(z)$, is calculated according to Kondo and Yamazaki (1990) as a bilinear function with snow depth, $h_{\text{s}}$:

$$T_{\text{snow}}(z) = \begin{cases} T_{\text{a}} - a_{\text{t}} \cdot (z - h_{\text{s}}) & : \quad h_{\text{s}} \geq z \geq z_0 \\ 0\,^{\circ}\text{C} & : \quad z_0 \geq z \geq 0 \end{cases} \tag{4.8}$$

where $z$ is the snow depth, $z_0$ the maximum value of $z$ where the snow temperature reaches $0\,^{\circ}\text{C}$ and $a_{\text{t}} \approx 0.033\,^{\circ}\text{C}\,\text{mm}^{-1}$ the temperature gradient in the surface-near layer.
The change in snow depth, $\text{d}h_{\text{s}}/\text{d}t$, is calculated by considering the effects of snow density changes, fresh snow and melt $M$:

$$\frac{\text{d}h_{\text{s}}}{\text{d}t} = -\frac{h_{\text{s}}}{\rho_{\text{d}}}\frac{\text{d}\rho_{\text{d}}}{\text{d}t} + \frac{\rho_{\text{f}}}{\rho_{\text{d}}}s - M, \tag{4.9}$$

where $\rho_{\text{d}}$ is the density of dry snow, $\rho_{\text{f}}$ the density of fresh snow, and $s$ the snow precipitation rate. The fresh snow density is derived as a sole function of air temperature following Anderson (1976).
The height of liquid water, $h_{\text{w}}$, is controlled by the amount of liquid precipitation, melt and outflow of the snow pack. Water outflow is calculated according to Nomura (1994) and Singh (2001) by a kinematic wave approximation. If the liquid water content, $\theta$, is larger than

the residual water content, $\theta_r$, then the outflow $O$ is obtained as $O = c\rho_w\theta h_w^d$ with $c$ and $d$ as constants and $\rho_w$ as the density of water. The residual water content is computed as $\theta_r = F_c\rho_d/\rho_w$ with $F_c$ = 0.02 (Tarboton and Luce, 1996; Kelleners et al., 2009) the mass of water retained per mass of dry snow. The exponent $d$ is set to $d = 1.25$ as proposed by Nomura (1994) and the site-specific coefficient $c$ is assumed to be equal to $1\,\mathrm{m}^{-1}\,\mathrm{h}^{-(d-1)}$ (De Michele et al., 2013). The change in liquid water height, $\mathrm{d}h_w/\mathrm{d}t$, is calculated with

$$\frac{\mathrm{d}h_w}{\mathrm{d}t} = p + \frac{\rho_d}{\rho_w}M - c\theta h_w^d, \tag{4.10}$$

where $p$ is the liquid precipitation rate.
The momentum balance equation, $\sigma - \rho_d g h_s$, and the rheological equation, $\eta = \sigma/\dot{\epsilon}$, are used to infer snow density changes, where $\sigma$ is the vertical stress, $g$ the gravitational acceleration, $\dot{\epsilon}$ the vertical strain rate, and $\eta$ the coefficient of viscosity computed as an exponential function of snow density and snow temperature. Accordingly, snow density changes are calculated as

$$\frac{d\rho_d}{dt} = c_1 h_s \rho_d^2 e^{(k_1(T_{snow}-T_\tau)-k_0\rho_d)}, \tag{4.11}$$

where $c_1$, $k_1$ and $k_0$ are constants set to $0.001\,\mathrm{m}^2\,\mathrm{h}^{-2}\,\mathrm{kg}^{-1}$, $0.08\,^\circ\mathrm{C}^{-1}$ and $0.021\,\mathrm{m}^3\,\mathrm{kg}^{-1}$, respectively (Kongoli and Bland, 2000; Ohara and Kavvas, 2006; Zhang et al., 2008). Equation (4.11) describes the change in density due to compaction and temperature change, and is calculated as an exponential function of snow density and snow temperature following Kojima (1967) and Mellor (1975).

#### Snow layer model

Each precipitation event was considered as a single snow layer which is stacked atop of the snow pack. Snow layers with a thickness of less than 1 cm were merged with the underlying layer in order to reduce computational efforts and to avoid arithmetic errors. If snow density exceeded the pore close-off density ($830\,\mathrm{kg\,m}^{-3}$), snow was treated as ice, and the corresponding snow layers were removed from the system.

### 4.3.4 Snow impurity model

Mineral dust and BC entered the system by liquid or solid precipitation, as wet deposition is expected to be the predominant mechanism (Raes et al., 2000; Koch, 2001). Particulate impurities were supposed to be evenly distributed in precipitation and consequently also in the snow layers. Particulates remained in the corresponding snow layer as long as there was no melt. When melt occurred, impurities of the melted snow were accumulated in the top 2 cm of the remaining snow layers (e.g. Flanner et al., 2007). When a snow fall event occurred, the dust and BC-enriched top layer became an independent snow layer and was buried by fresh snow. We assumed constant ice albedo and no dust reservoir for ice since the effects of snow impurities on the ice albedo and the removal of snow impurities by melt water on ice are only poorly understood and subject to a high spatial variability. Hence, when firn turned into ice, the dust and BC of the corresponding layer was removed from the system.
Melt water percolation may lead to vertical redistribution of snow impurities. Different studies have investigated the removal of particulate impurities by melt water (e.g. Conway et al., 1996; Flanner et al., 2007). They found that larger particles (>5μm) remain mostly in the snow and are not efficiently removed by percolation of melt water (Conway et al., 1996), whereas smaller

snow impurities (∼0.2 μm) are washed out by about 10–30% per mass of melt (Doherty et al., 2013). According to these results, we assumed that mineral dust (particle size 2.5–4.5μm) is not affected by wash-out due to melt water, whereas for BC (particle size 0.2–0.3μm) a removal efficiency (the amount of BC which is removed by melt water with each increment of melt) of 20% was assumed (Flanner et al., 2007).

### 4.3.5 Calibration

The melt parameters, TF and SRF, and the accumulation parameter, $c_{\text{prec}}$, were calibrated for each year individually by means of the seasonal balance measurements. This annual calibration ensures that simulated mass balances coincide with observations in order to extract an accurate sequence of melt and accumulation events controlling the surface concentrations of light-absorbing impurities. In a first step, $c_{\text{prec}}$ was adjusted according to the measured winter accumulation, then TF and SRF were tuned to the annual mass balance records. This procedure is repeated until the difference between simulated and observed mass balance was less than 10 mm water equivalent (w.e.). The ratio between TF and SRF was kept constant over the entire period in order to reduce the degrees of freedom and to avoid changes in air temperature/radiation sensitivity of the model among individual years. The ratio was set to 0.04 according to extensive testing for another Alpine glacier (Gabbi et al., 2014). During calibration the complete snow impurity and snow density model was used.

## 4.4 Results

### 4.4.1 Snow impurity concentration

#### Saharan dust

At the upper measurement site, located in the accumulation area of Claridenfirn, the mean annual Fe-oxide concentration in the surface layer was $0.92 \pm 1.04\,\text{mg}\,\text{kg}^{-1}$ on average. Exceptionally high surface loads were observed in years with increased deposition of Saharan dust, particularly in 1936, 1977, 1990 and 2000 (Fig. 4.4a). Annual Fe-oxide concentrations of up to $6.3\,\text{mg}\,\text{kg}^{-1}$ occurred at the upper stake. Concentrations of similar magnitude as in years with high Saharan dust input were reached in the late 1940s. Periods of intense solar radiation, such as in the 1940s, led on the one hand to increased melting due to higher transmissivity of the atmosphere (Huss et al., 2009b) and on the other hand to an enhanced re-exposure of snow impurities, and thus to a distinct darkening of the glacier surface which further reinforced ablation.

At the lower measurement site, located near the glacier's equilibrium line altitude (ELA), the mean Fe-oxide concentration was more than twice as high as at the upper stake and was $2.24 \pm 3.33\ \text{mg}\,\text{kg}^{-1}$ on average. Consistent with the upper site, increased mineral dust amounts were observed during years with high Saharan dust activity and during periods with intense melting (Fig. 4.4b). In addition to the 1940s, a second period with pronounced accumulation of mineral dust due to enhanced melting occurred in the 2000s. In 2007, the mean Fe-oxide concentration reached a maximum value of $26.8\,\text{mg}\,\text{kg}^{-1}$ as a result of the almost complete melting of the firn layers and thus, the re-exposure of heavily dust-loaded layers (e.g. extraordinarily large Saharan dust events of 2000). From 2008 onwards, surface Fe-oxide concentrations at the lower stake declined sharply as all firn layers have been depleted

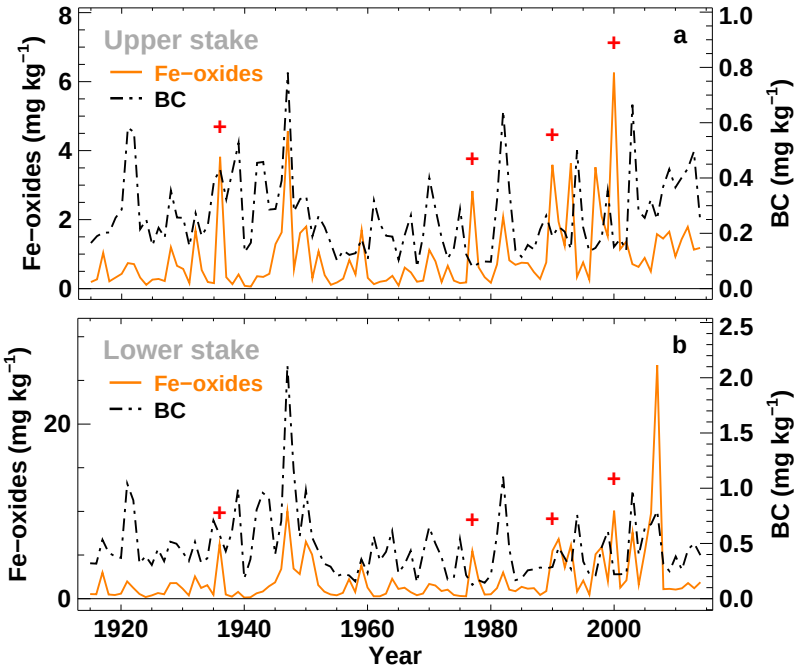


Figure 4.4: Average Fe-oxide and BC concentrations in the surface snow at the upper and lower measurement site on Claridenfirn for the period 1914–2014. The crosses mark years with exceptionally high Saharan dust activity. Note that the scales for upper and lower stake are different.

and the bare ice surface was exposed. Thus, due to the prescribed constant ice albedo, the remaining dust did not have an influence on albedo and was assumed to be washed out at the impermeable ice surface.

In the accumulation area (upper stake) most of the mineral dust exposed at the surface originated from deposition occurring during the same year. Only in the few years with negative mass balances mineral dust of previous years reappeared and reinforced the darkening of the glacier surface. In specific years (e.g. 1947 and 1991), mineral dust of previous years accounted for 45–65% of the total mineral dust at the surface (Fig. 4.5a). On average, however, the fraction of mineral dust of preceding years becoming albedo-relevant was small and made up only 8% of the total surface dust budget. At the ELA (lower stake) mineral dust of previous years more effectively influenced surface dust concentrations and accounted for about 30% of the total exposed mineral dust. Particularly in the 1940s and 2000s, but also in the early 1960s and the 1990s, large quantities of previously buried dust were re-exposed at the surface. Up to 97% of the total surface dust in 2006 and 2007 originated from deposition in preceding years (Fig. 4.5b). Accordingly, mineral dust of much older layers was re-exposed at the surface of the lower measurement site in comparison to the upper stake. While at the stake in the accumulation area, surface dust had a maximum age of three years, mineral dust at the lower stake was found to have an age of up to 21 years (Fig. 4.5c, d).

### Black carbon

Mean surface concentrations of BC showed a distinctly different pattern than mineral dust concentrations. BC concentrations at the glacier surface were mainly controlled by the melt regime and were less influenced by episodic deposition compared to Saharan dust (Fig. 4.4).

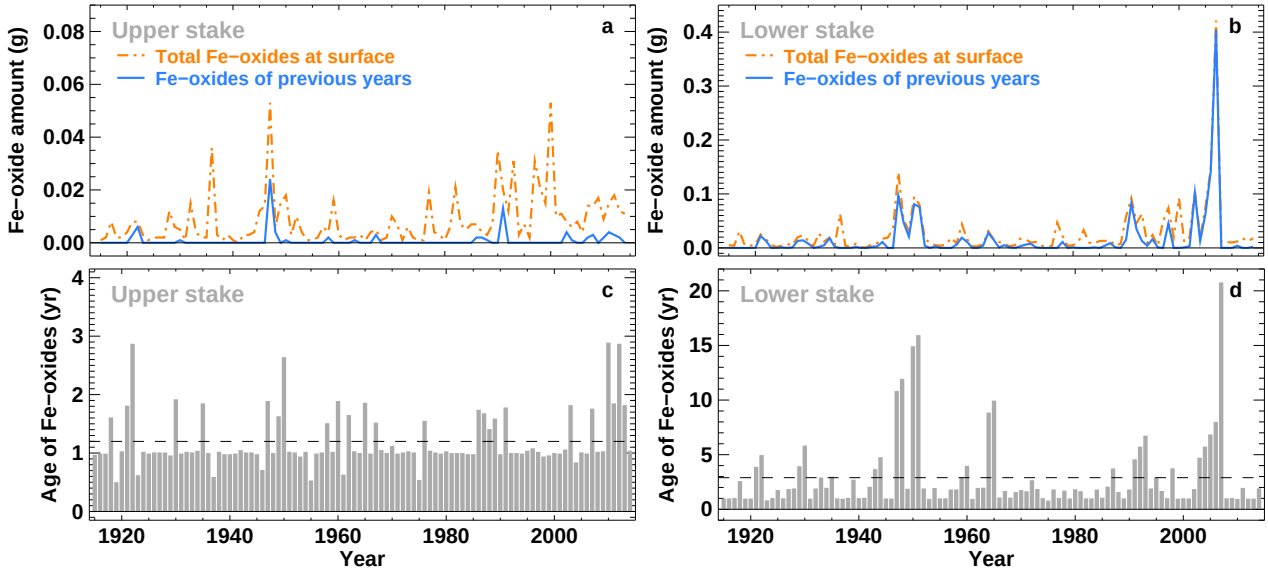


Figure 4.5: Total Fe-oxide amount of the surface snow layer of each year and the amount of Fe-oxides of previous years emerging at the surface through melt-out over the period 1914–2014 for (a) the upper and (b) the lower stake. (c) and (d) illustrate the age of the oldest mineral dust present at the glacier surface for each year for both sites. Note that the scales for the upper and lower site are different.

An exception was the year 1982, when exceptionally high deposition of BC were recorded (see Fig. 4.2a). Mean concentrations of BC over the entire period were $0.26 \pm 0.14\,\mathrm{mg\,kg^{-1}}$ and $0.46 \pm 0.29\,\mathrm{mg\,kg^{-1}}$ on average for the upper and lower stake, respectively. For both locations, highest BC concentrations were observed in the melt-intense years around 1947 and the deposition-intense year 1982 (Fig. 4.4). BC concentrations of up to $0.78\,\mathrm{mg\,kg^{-1}}$ (upper stake) and $2.12\,\mathrm{mg\,kg^{-1}}$ (lower stake) were found.

### Absorption of mineral dust vs black carbon

In contrast to BC, mineral dust concentrations at the surface were up to five times larger. However, as BC is much more absorptive than mineral dust (mass absorption coefficient about 10 times higher), the overall absorption by BC and dust are in a similar range. In individual years with extraordinarily high Saharan dust input, such as in 1936, 1977, 1990 and 2000, mineral dust dominated the absorption of solar radiation (Fig. 4.6). In all other years, the absorption of BC outweighed the absorption of mineral dust, and over the entire period BC was clearly the dominant absorber. While at the upper stake, the absorption due to BC was 3.3 times higher on average compared to mineral dust, at the lower stake BC resulted in a 2.2 times higher absorption. These statements are based on the assumption that BC is more efficiently removed by melt water than mineral dust and therefore depend on the chosen removal efficiency. If removal rates of BC and mineral dust would be in a similar range, the influence of BC on the absorption would be even larger.

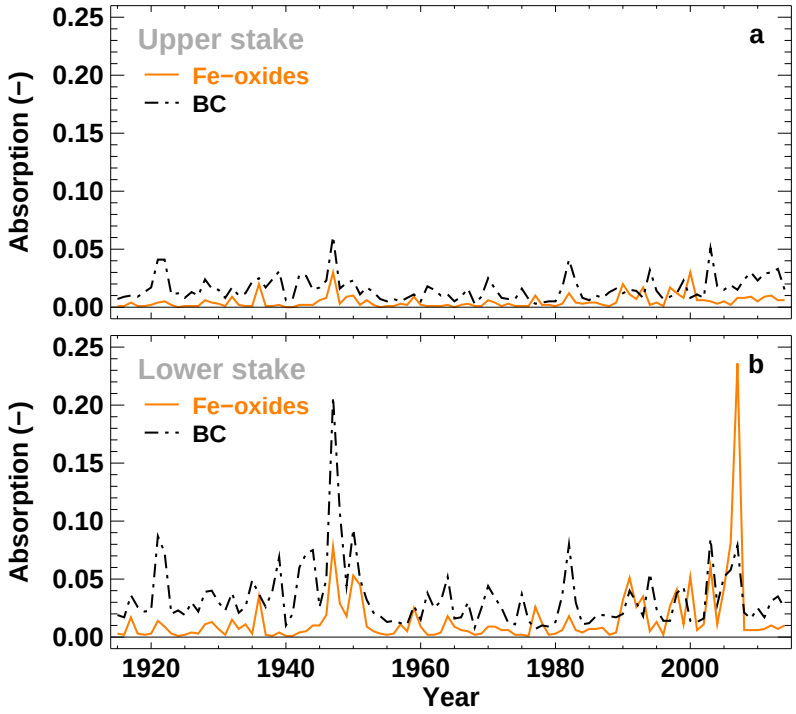


Figure 4.6: Mean annual absorption (optical depth) of mineral dust and BC over the period 1914–2014 for (a) the upper and (b) the lower stake. The optical depth is calculated as a product of the mass absorption coefficient of BC/Fe oxides and the corresponding loading in the snow surface layer (top 2 cm).

### 4.4.2 Effect of Saharan dust and black carbon on albedo and mass balance

#### Surface albedo

On average the reduction of mean annual surface albedo due to Saharan dust was less than 0.01 compared to snow with BC only. At the upper measurement site the mean annual albedo was reduced by $0.004 \pm 0.004$, at the lower stake by $0.008 \pm 0.009$. Regarding summer albedo (April–September), i.e. the albedo during the period with snow, firn and ice melting, the effect of Saharan dust was larger and reduced the mean summer albedo at the upper stake and lower stake by $0.006 \pm 0.006$ and $0.011 \pm 0.012$, respectively. However, in individual years with a high accumulation of Saharan dust (i.e. years with a high Saharan dust input and/or melt-intense periods) the impact on snow albedo was significantly larger. At the lower measurement site, at the transition between accumulation and ablation zone, the largest reduction in albedo occurred in 2007, when the mean annual albedo was reduced by about 0.060. At the upper stake, highest influence of Saharan dust on the surface albedo was observed in the dust-intense year 2000 with a maximal albedo reduction of 0.025.

The overall impact of BC on the surface albedo was substantially higher than that of Saharan dust. Our results suggest that BC reduced the albedo over 1914–2014 by $0.027 \pm 0.009$ at the upper stake and by $0.038 \pm 0.013$ at the lower stake compared to snow with dust only. The largest contribution of BC to albedo reduction occurred in the melt dominated periods in the 1940s and the 2000s, when the albedo was lowered by up to 0.06. In total, Saharan dust and black carbon reduced the mean annual albedo by 0.041 and 0.062 on average compared

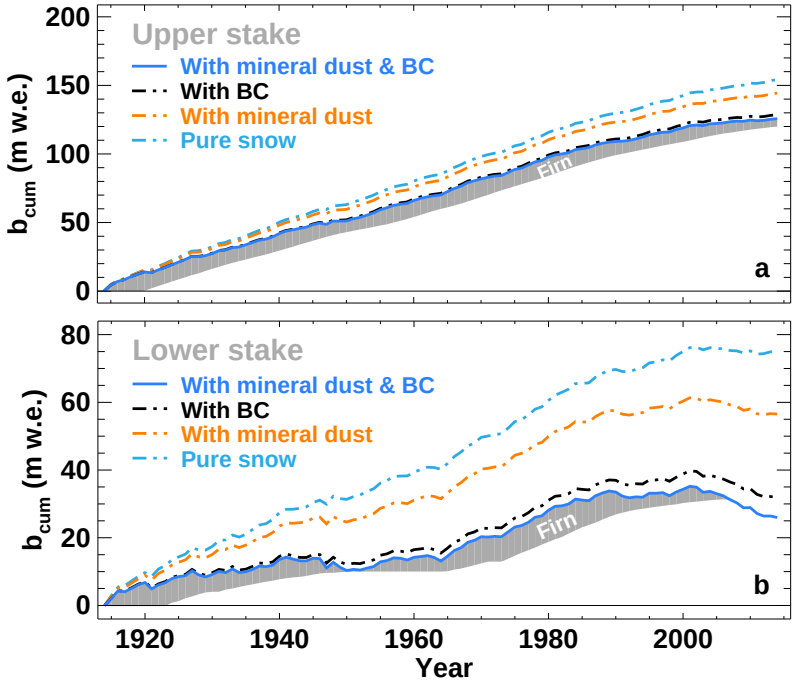


Figure 4.7: Cumulative mass balance over the period 1914–2014 at (a) the upper and (b) the lower measurement site. The solid blue line refers to the cumulative mass balance under real conditions (including Saharan dust and BC) and is consistent with the direct observations on Claridenfirn. The dash-dotted lines correspond to simulations (1) without Saharan dust (with BC), (2) without BC (but with Saharan dust), and (3) with pure snow conditions. The grey shaded area indicates the thickness of the entire firn column in m w.e.

to pure snow at the upper and lower stake.

### Mass balance

The impact of Saharan dust on the total mass change over the 100-year period was in the order of a few meters and was less pronounced in the accumulation area than at the ELA (Fig. 4.7). At the upper measurement site, the difference in total cumulative mass balance due to Saharan dust was 2.8 m w.e. compared to the measured total 100-year cumulative mass balance of 125.8 m w.e. At the lower stake, the absolute difference was twice as large and was 5.8 m w.e. (with a total cumulative mass balance of 26.4 m w.e.). Regarding annual balance, Saharan dust thus accounted for about –28 mm w.e. $yr^{-1}$ at the upper stake and for about –58 mm w.e. $yr^{-1}$ at the lower stake compared to snow with BC only (Fig. 4.8a and c). Mean annual melt was increased by about 1.4% (upper stake) and 2.0% (lower stake) by the presence of Saharan dust. In specific years, Saharan dust enhanced the overall annual melt by up to 13%.

Maximum deviations in annual mass balance due to Saharan dust were up to –142 mm w.e. $yr^{-1}$ for the upper and –271 mm w.e. $yr^{-1}$ for the lower measurement site in individual years. In years with high dust concentrations at the surface (Fig. 4.4) also largest changes in mass balance were observed (Fig. 4.8a and c). However, changes in mass balance cannot be directly deduced from average dust concentrations, because (1) the impurity concentration and albedo changes are not linearly related and thus a higher impurity concentration might lead to smaller changes in albedo, and (2) during years with high melt rates also other particulate impurities accumulate

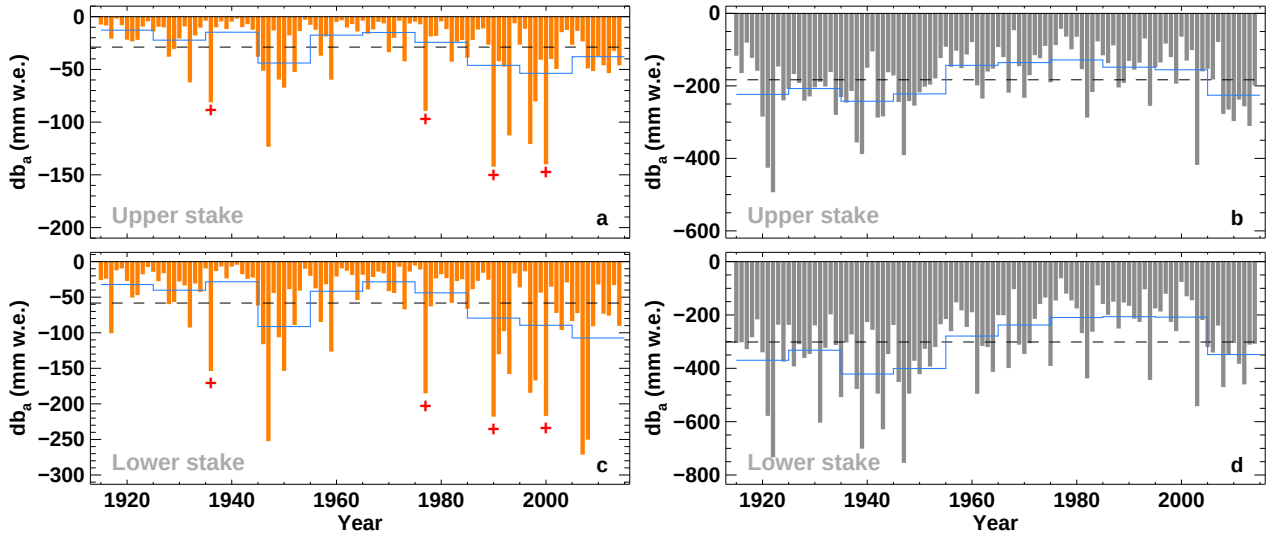


Figure 4.8: Effect of Saharan dust on annual mass balance for the period 1914–2014 for (a) the upper and (c) the lower stake and the effect of BC for (b) the upper and (d) the lower stake. Bars show differences in annual mass balance between model results including or neglecting Saharan dust/BC. The dashed line refers the mean over the period 1914–2014 and the solid blue line to the 10-year average. Crosses mark years with exceptionally high Saharan dust activity.

at the surface, which limits the total impact of Saharan dust on surface mass balance. Thus, despite the exceptionally high surface concentration in 2007, the change in mass balance is only slightly larger than in years with lower surface concentrations as for example in the deposition intense year 2000 (Fig. 4.8a and c).

The BC-induced albedo changes led to an average reduction in annual mass balance of 183 mm w.e. $yr^{-1}$ at the upper and of 301 mm w.e. $yr^{-1}$ at the lower stake compared to snow with dust only. In individual years, annual mass balance anomalies might reach up to –494 mm w.e. $yr^{-1}$ at the upper stake and up to –754 mm w.e. $yr^{-1}$ at the lower stake (Fig. **??**) and peak values up to three times larger compared to the effect of Saharan dust. The difference in cumulative mass balance between the real situation, being consistent with direct field observations (including mineral dust and BC in the model) and simulations without BC (but with mineral dust) over 1914-2014 is 18.3 m w.e. for the upper and 30.1 m w.e. for the lower stake (Fig. 4.7). Annual melt rates were amplified by 9% (11%) at the upper (lower) stake on average and by 19% (22%) at maximum.

The combined effect of Saharan dust and BC reduced the mean annual mass balance by 282 mm w.e. $yr^{-1}$ and 485 mm w.e. $yr^{-1}$ at the upper and lower stake, respectively. Annual melt was amplified by 15% (upper stake) and 19% (lower stake) on average by the presence of two light-absorbing impurities. In the year 1947, characterized by exceptionally high melt rates, Saharan dust and BC intensified annual melt by up to 36%.

## 4.5 Discussion

### 4.5.1 Radiative forcing

Converting changes in annual mass balance caused by absorption of dust into the energy consumed for melt allowed calculating the radiative forcing of snow impurities. The radiative forcing (RF, $\mathrm{W\,m^{-2}}$) was calculated based on the change in melt rate, $\Delta M$ (m/s), caused by the presence/absence of mineral dust and/or BC in snow:

$$\mathrm{RF} = \Delta Q_\mathrm{M} = \Delta M \, L_\mathrm{f} \, \rho_\mathrm{W} \tag{4.12}$$

where $Q_\mathrm{M}$ ($\mathrm{W\,m^{-2}}$) is the energy consumed by melt, $L_\mathrm{f}$ (333'700 $\mathrm{J\,kg^{-1}}$) the latent heat of fusion and $\rho_\mathrm{W}$ (1'000 $\mathrm{kg\,m^{-3}}$) the density of water. Changes in melt rates are equal to changes in mass balances as presented in Section 4.4.2.

For the measurement site in the accumulation area we found a mean radiative forcing over the 100-year period of $+0.3\,\mathrm{W\,m^{-2}}$ due to Saharan dust, whereas at the stake close to the equilibrium line the radiative forcing was $+0.6\,\mathrm{W\,m^{-2}}$. In contrast to Saharan dust, the radiative forcing of BC over 1914–2014 was about seven times larger, and was $+1.9$ and $+3.2\,\mathrm{W\,m^{-2}}$ on average for the two sites. In the summer months, July and August, when melting is strongest, the radiative forcing for BC reached values of 8.7–9.7 $\mathrm{W\,m^{-2}}$ and for Saharan dust of 3.0–3.7 $\mathrm{W\,m^{-2}}$ compared to pure snow at the upper stake, and 12.9–15.9 $\mathrm{W\,m^{-2}}$ and 4.7–6.3 $\mathrm{W\,m^{-2}}$ at the lower stake, respectively. At the daily scale, maximum modelled radiative forcing was 15–42 $\mathrm{W\,m^{-2}}$ for Saharan dust and 43–66 $\mathrm{W\,m^{-2}}$ for BC.

At a global scale, the mean radiative forcing from BC in snow is reported to be in the range of 0.02–0.08 $\mathrm{W\,m^{-2}}$ (Bond et al., 2013; IPCC, 2013). During boreal spring, when the snow-albedo feedback is maximal, the radiative forcing of mineral dust and BC over Eurasia is higher and amounts to 1.2 and 2.7 $\mathrm{W\,m^{-2}}$, respectively (Flanner et al., 2009). For snow-covered surfaces of the Tibetan Plateau the radiative forcing of BC reaches values of up to 5–25 $\mathrm{W\,m^{-2}}$ in springtime (Flanner et al., 2007; Kopacz et al., 2011; Qian et al., 2011). Similar peak values are found for desert dust in the mountain snow cover of the Colorado River Basin (25–50 $\mathrm{W\,m^{-2}}$, Painter et al., 2007; Skiles et al., 2012). In general, radiative forcing of BC found for Claridenfirn is at the lower end of the range of values obtained for Colorado or Tibetan Plateau. Regarding mineral dust, the effect is also clearly stronger on the Colorado Plateau than in the Alps. In terms of maximum daily radiative forcing, values obtained for Claridenfirn are of similar magnitude as for other regions. However, radiative forcing reported in other studies is not directly comparable to the results of this study as dust/BC source and the temporal dynamics of melting are different. Furthermore, radiative forcing of some of the above-mentioned studies was calculated by directly accounting for the change in the energy fluxes, rather than using the change in melt rates due to light-absorbing impurities as in our approach. Hence, the radiative forcing reported here represents a lower limit as the radiative impact in the pre-melt season is not taken into account.

Painter et al. (2013) suggested that the rapid retreat of Alpine glaciers at the end of the Little Ice Age was forced by increasing BC concentration due to industrialisation. They found BC-induced mass balance anomalies in the order of $-500$ mm w.e. $\mathrm{yr^{-1}}$ for the ablation area, which is similar to our results for the accumulation area ($-180$ to $-300$ mm w.e. $\mathrm{yr^{-1}}$) despite the different modelling approaches. While Painter et al. (2013) used a sophisticated radiation model (SNICAR, Flanner et al., 2007) to derive BC radiative forcing and in turn equivalent changes in air temperature and mass balance, we used a simple broadband albedo parameterisation in combination with a mass balance model. However, Painter et al. (2013)

Table 4.1: Parameters of the impurity, the SSA and the snow density model and the corresponding parameter ranges (±20%) applied in the sensitivity analysis.

| Parameter | Unit | Value | Range |
|---|---|---|---|
| **Impurity model** | | | |
| Dust input | $\mu g\,kg^{-1}$ | 22.3 | 17.8 - 26.8 |
| BC input | $\mu g\,kg^{-1}$ | 23.2 | 18.6 - 27.8 |
| BC removal rate | % | 20 | 16 - 24 |
| Fe in FeO | % | 54.5 | 43.6 - 65.4 |
| MAC FeO/BC | - | 0.082 | 0.066 - 0.099 |
| **SSA model** | | | |
| $SSA_{initial}$ | $m^2\,kg^{-1}$ | 73.0 | 58.4 - 87.6 |
| $SSA_{min}$ | $m^2\,kg^{-1}$ | 8.0 | 6.4 - 9.6 |
| $C_1$ | $10^{-3}\,mm^3\,d^{-3}$ | 1.1 | 0.88 - 1.32 |
| $C_2$ | $10^{-5}\,mm^3\,d^{-3}$ | 3.7 | 2.96 - 4.44 |
| **Snow density model** | | | |
| $a_t$ | $°C\,mm^{-1}$ | 0.033 | 0.0264 - 0.0396 |
| $c_1$ | $m^2\,h^{-2}\,kg^{-1}$ | 0.001 | 0.0008 - 0.0012 |
| $k_0$ | $m^3\,kg^{-1}$ | 0.021 | 0.0168 - 0.0252 |
| $k_1$ | $°C^{-1}$ | 0.08 | 0.064 - 0.096 |
| $F_C$ | - | 0.02 | 0.016 - 0.096 |
| $c$ | $m^{-1}\,h^{-(d-1)}$ | 1.0 | 0.8 - 1.2 |
| $d$ | - | 1.25 | 1.0 - 1.5 |

assume 10 to 20 times higher BC concentrations than reported by the ice core data in order account for altitudinal differences between the high-altitude ice core sites and the ablation area. In our study, we do not alter atmospheric deposition rates (see Section 4.5.4), but, contrary to Painter et al. (2013), account for changes in the BC surface concentration due to melt and accumulation processes as well as to removal by melt water. As a result, we obtain similar BC concentrations in the surface layer on average and thus, a comparable impact of BC on glacier mass balance. The general agreement of our assessment with that by Painter et al. (2013) indicates the highly relevant role of BC in shaping changes in glacier mass balance over the last century.

### 4.5.2 Sensitivity analysis

In order to assess the sensitivity of the model results to the chosen input parameters, we performed a sensitivity analysis. Four parameters of the snow impurity model were examined: (1) removal rates of BC by melt water, (2) fraction of Fe which is presented as Fe-oxides, (3) the proportion of haematite and goethite in the Fe-oxides, and (4) the ratio of the MAC of BC vs. MAC of Fe-oxides. In addition, another four parameters of the SSA model ($SSA_{initial}$, $SSA_{min}$, $C_1$, $C_2$) and six parameters of the snow density model ($a_t$, $c_1$, $k_0$, $k_1$, $F_c$, $c$, $d$) were

investigated. Furthermore, we also assessed implications of deviating atmospheric deposition rates of mineral dust and BC on the mass balance as the ice core data is taken from another site (see Section 4.5.4). The parameters of the melt and accumulation model were not included in the sensitivity analysis because they were directly constrained by the continuous seasonal mass balance measurements at the study sites. The sensitivity of the parameters was assigned by varying each parameter by 5% intervals around to the chosen value in a range of $\pm 20\%$, keeping all other parameters constant. Tab. 4.1 shows the used parameter ranges. According to Anslow et al. (2008) we defined the sensitivity of a parameter as the slope around the origin of the curve, defined by the percentage change in the parameter value and the percentage change in the resulting model variable (mass balance in our case). For example a sensitivity of 0.5 designates that an arbitrary percentage change in the parameter value involves a half as large percentage change in the mass balance. A positive sensitivity means that an increase in the parameter value leads to an increase in the mass balance, a negative sensitivity that an increase in the parameter yields a decrease in mass balance.
Results of the sensitivity analysis are shown in Fig. 4.9. The mass balance was most sensitive to the amount of snow impurities and the parameters of the snow density model, while the parameters of the SSA model were clearly less relevant. In contrast to the input quantity of BC, mineral dust had a less pronounced impact on modelled mass balance. A change of 10% in the BC concentration in precipitation led to a 5.8% change in mass balance, whereas the same change in the mineral dust concentration in precipitation only resulted in a 1.6% change in mass balance. The reason for this difference in sensitivity is the stronger absorption of solar radiation by BC compared to mineral dust. An even higher sensitivity could be assigned to the removal efficiency of BC with melt water. A 10% change in the BC removal rate leads to a 1.5 times larger change in the mass balance. This is particularly important since the removal rates are subject to considerable uncertainty (see Section 4.5.5). Hence, the removal of BC by melt water seems to be the most critical point of the simulation and strongly controls the impact of BC on the long-term glacier mass balance. Besides the impurity model, also the performance of the density model affected the simulations. In particular, parameter $k_0$ (Eq. 4.11), describing the density change due to compaction, and the outflow parameter $d$ (Eq. 4.10) were found to have sensitivities that are comparable to those of the input concentration of BC (Fig. 4.9). The higher the values of the density parameters, $k_0$ and $d$, the faster is snow compaction. More efficient compaction in turn entails higher impurity concentrations in the surface snow layer and thus enhanced melt rates. The parameters of the SSA model show the lowest sensitivity and therefore are less relevant for the results. The two parameters, $SSA_{min}$ and $SSA_{initial}$ (Eq. 4.5), are the most sensitive ones. An increase in the two parameter values leads to a depletion in pure snow albedo, which slightly diminishes the impact on snow impurities. However, this effect is small compared to the other uncertainties.

### 4.5.3 Spatial distribution of the effect of light-absorbing impurities

The extent of the impact of Saharan dust and BC on the glacier mass balance is spatially variable and strongly depends on prevailing conditions. According to our results, the effect of light-absorbing impurities increase from the accumulation area towards the equilibrium line as higher melt rates lead to a re-exposure of old firn layers bearing light-absorbing impurities. In the ablation area where most glacier mass loss occurs, however, the processes are different. Winter accumulation is not preserved over multiple years and thus light-absorbing snow impurities affect only the albedo of the winter snow cover until it has been melted away. During the summer season when bare ice is exposed at the surface, snow impurities are removed by

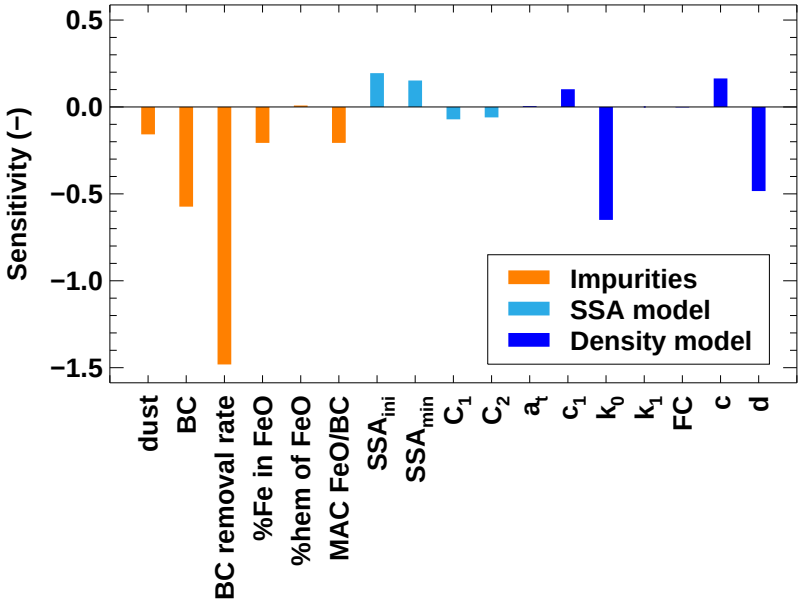


Figure 4.9: Sensitivity of annual surface mass balance (i.e. the percentage change in the parameter value versus the percentage change in annual mass balance) to the different parameters of the impurity, the specific surface area and the snow density model, as well as the sensitivity to the input of mineral dust and BC.

melt water which might limit the impact of impurities on glacier melt, although a darkening on gently-sloping glacier tongues has also been observed (Oerlemans et al., 2009). Hence, we suppose that the effect of Saharan dust and BC in the ablation area is lower compared to areas near the equilibrium line.

### 4.5.4 Transferring mineral dust/black carbon to Claridenfirn

Our analysis is based on the general assumption that concentrations of Saharan dust and BC in precipitation at Colle Gnifetti and Fiescherhorn (Fig. 4.1) are comparable to those at Claridenfirn. In order to receive undisturbed records of past aerosol concentrations only few sites in the Alpine region are suitable. Prerequisites are high elevation to exclude chemical disturbance by melt water percolation, sufficient ice thickness to ensure long enough records and flat terrain to limit the effect of ice flow (Wagenbach and Geis, 1989). For this reason we relied on time series at locations other than Claridenfirn and had to transpose the measurements to the study site for which long-term mass balance measurements were available.

In the 1990s a large-scale study about the chemical composition of high-alpine winter snow packs was carried out in the Alps with the aim of detecting the regional and altitudinal distribution of major ions (SNOSP; Nickus et al., 1997). It was found that the concentration of most ionic species in winter snow increases by about one third from west to east and that ionic loads show no regional preference due to opposite gradients in the prevailing precipitation patterns. The same also applies to variations with altitude: at higher elevation ion concentrations are lower compared to valleys, but the general increase in precipitation with elevation compensates for this effect, so that ionic loads are expected to be in the same order of magnitude independent of absolute elevation. A more detailed investigation of selected sampling locations in the vicinity of Colle Gnifetti/Fiescherhorn (Breithorn, Gorner-/Theodulgletscher, Colle Vincent,

Jungfraujoch) revealed that there is no distinct altitudinal trend in ionic loads (Nickus et al., 1997). A recent study about atmospheric deposition in alpine and subalpine areas confirms these results and concludes that there are no clear regional gradients, but a significant spatial variability of atmospheric ion deposition over the Alps (Rogora et al., 2006). Another study concluded that sites with large quantities of precipitation exhibit highest ion concentrations because they receive generally the first, more contaminated fraction of a precipitation event (Nickus et al., 1998).
The above mentioned studies are mainly focused on anthropogenic impurities of winter snow packs and can not be directly transferred to the situation at Claridenfirn. We suppose that concentrations at Claridenfirn might be higher than at Colle Gnifetti/Fiescherhorn due to (1) its eastern location, (2) the lower elevation and thus proximity to the polluted mixing layer, and (3) the higher precipitation rates (MeteoSwiss, 2014b). However, we are unable to conclude with certainty whether and to what extent ion concentrations differ between the ice cores and our study site. For these reasons we adopted the impurity concentrations measured at Colle Gnifetti/Fiescherhorn directly to the study site without a transfer function. Our assumption is supported by a supplementary analysis carried out on Claridenfirn. Kappenberger and Steingruber (2014) collected and analysed winter snow samples for major ions between 1995 and 2013. Comparison of bulk winter snow concentrations with those at Colle Gnifetti revealed that concentrations at both locations are in the same order of magnitude. In contrast to Saharan dust which is transported by large-scale upper air flows, BC concentrations are more influenced by the regional environment. Therefore, the assumption of using concentrations from a remote location might be less valid for BC than for Saharan dust. Actual BC input concentrations are thus subject to a higher uncertainty.

### 4.5.5 Removal by melt water

When a snowpack begins to melt, the insoluble snow impurities are partly retained and concentration of impurities in the surface snow increases as snow melt proceeds, thus reducing snow albedo. Consequently, melt is amplified and therefore provides a positive feedback on radiative forcing by light-absorbing impurities. To what extent snow impurities are removed by melt water percolation has not been fully clarified and only a small number of studies has addressed this issue so far. Important contribution is made by Conway et al. (1996), who found that particles of volcanic ash remained at or near the surface throughout the melting process while a large part of soot particles was flushed through the snow with the melt water. They suppose that the difference in the particle's diameters is responsible for the different behaviour of ash and soot during the melting process. Doherty et al. (2013) concluded that removal rates due to melt water percolation of BC are in the order of 10–30% which is in agreement with the results by Conway et al. (1996). Based on the limited information available, a removal efficiency of 20% for BC seems to be a reasonable assumption. The sensitivity study indicated that the results are more sensitive on the removal rate than the amount of mineral dust and BC input. Hence, this issue needs further investigation. However, ignoring flushing-out of BC with melt would lead to an overestimation of surface concentrations and thus to an excessive melt amplification through BC (Doherty et al., 2013).

### 4.5.6 Mass balance model

The performance of the albedo parameterisation mainly depends on an accurate modelling of the specific surface area of snow grains and the fraction of snow impurities in the surface snow.

Roy et al. (2013) demonstrate that the simulated snow grain sizes are in good agreement with measurements and that despite the simplicity of the SSA model results are comparable to well-established snow models (i.e. Crocus, Brun et al., 1989, 1992). The root-mean-square error in the overall SSA is $8.0\,m^2\,kg^{-1}$ corresponding to an albedo uncertainty in the order of $\pm 3\%$ for small grains and of $\pm 6\%$ for large grains. The main limitation of the SSA model is the performance during wet conditions due to the simplification regarding the 1-layer model for liquid water. As for the SSA model, the liquid water content is important also for the snow density model (De Michele et al., 2013). Snow density measurements, performed twice a year during the winter and late summer surveys on Claridenfirn, were used to validate the snow density model. Correlation of observed and simulated snow densities reveals a $r^2$ of 0.52 and 0.47. Mean absolute differences are $10.8\,kg\,m^{-3}$ and $9.4\,kg\,m^{-3}$ (corresponding to a relative difference of $\sim 2\%$) for the lower and upper measurement site, respectively. This indicates that the density model well captures the typical snow density, but does not fully reproduce interannual variability.

## 4.6 Conclusions

In this study we analysed the impact of Saharan dust and black carbon on the mass balance of an Alpine glacier over a centennial period (1914–2014) covered by exceptional observational data sets. A mass balance model including a parameterisation for albedo was combined with a snow density model in order to track snow layers and impurities over time. The combined model was forced with temperature and precipitation time series in daily resolution, the latter being assigned by mineral dust and BC concentrations retrieved from ice/firn cores.

On average the presence of Saharan dust at the glacier surface reduced mean annual albedo by less than 0.01. The associated decrease in the mean annual mass balance was $28-58$ mm w.e. depending on the location on the glacier (accumulation area, equilibrium line). However, in individual years with very high supply of Saharan dust, surface albedo can be reduced substantially with a strong impact on snow and ice ablation. In addition to years with large atmospheric dust deposition, also periods of strong melting may lead to significantly enhanced dust concentrations due to re-exposure of buried firn layers with a high impurity content. In contrast to mineral dust, BC affected the mass balance more efficiently and clearly dominated light absorption in snow except for years with large Saharan dust events. On average BC lowered the annual albedo by 0.03 and reduced the mean annual mass balance by 183–301 mm w.e. Due to the combined effect of BC and Saharan dust annual ablation on Claridenfirn was increased by 15–19% on average over 1914-2014 compared to pure snow conditions. In the accumulation area, the impact of Saharan dust and BC on the mass balance was clearly less pronounced due to the prevailing positive mass balances that tend to continuously bury snow impurities. The most sensitive parameter of our assessment is the removal rate of snow impurities by melt water, a process which is until now only poorly understood.

Our study demonstrates that the influence of snow impurities on glacier melting should be taken into consideration, when modelling the mass balance of alpine glaciers over long-term periods in order to increase the reliability of the simulations. Particularly in years with large deposition of Saharan dust or BC and during periods with negative glacier mass balance, re-exposure of old firn layers can importantly impact on the rate of snow and ice ablation and thus enhance the albedo feedback. Furthermore, the study emphasizes the crucial role of BC in melt processes taking place on Alpine glaciers.

**Acknowledgements**

This study was supported by the National Research Programme NRP61. Many thanks go to all those who performed mass balance measurements at Claridenfirn with great effort and care. We particularly thank the two key players, H. Müller and G. Kappenberger, for collecting and homogenizing the mass balance measurements. T.M. Jenk and M. Sigl are gratefully acknowledged for providing ice core data of Colle Gnifetti and Fiescherhorn. The analysis of EC in the upper part of the Fiescherhorn ice core (1940-2002) was funded by the EU FP7 project PEGASOS. We thank M. Funk for his helpful comments on an earlier version of the manuscript. Furthermore, we thank MeteoSwiss for providing meteorological time series and the Global Energy Balance Archive (GEBA), ETH Zurich, for the radiation data of Davos. Aerosol measurements at the high-alpine research station Jungfraujoch were conducted by Global Atmosphere Watch (GAW).

# Chapter 5

# Conclusion and Outlook

## 5.1 Synthesis

The presented thesis investigates different aspects of glacier mass balance modelling in detail with the aim of reducing uncertainties and thus improving mass balance simulations of mountain glaciers with regard to long-term predictions. The thesis focuses, in particular, on the importance of (1) the ice-thickness distribution, (2) the melt model approach and (3) the surface albedo for glacier studies in the past and into the future.

Based on an exceptionally dense network of ground- and helicopter-based ground penetrating radar measurements, the ice-thickness distribution in the Mauvoisin region, comprising a glacier covered area of 63 $km^2$, could be accurately determined. A total ice volume of $3.69 \pm 0.31$ $km^3$ and a maximal ice thickness of nearly 300 m were found. In a further step, the measurement-based ice volume estimate was compared with the result of an ice-thickness estimation approach (Farinotti et al., 2009b) relying on ice flow mechanics and topographic parameters. Results showed that the ice-thickness estimation approach lead to an overestimation of the total ice volume in the order of 36% (-8 $\leftrightarrow$ +80%). Finally, glacio-hydrological modelling was performed and the effect of an inaccurate ice-thickness estimation, due to a lack of measurements or the usage of inappropriate estimation approaches, on runoff projections was examined. The sensitivity analysis revealed that over- and underestimations of the ice volume have a serious impact on glacier and runoff projections and that they might even lead to deviations from the projected general runoff trend. This clearly indicates that ice-thickness data are essential to get reliable ice volume estimates. With regard to helicopter-based measurement techniques, the acquisition of ice-thickness data becomes much less laborious and provides a unique tool to infer the area-wide ice thickness distribution accurately. Knowledge about the ice-thickness distribution, in turn, clearly increases the validity of glacier and runoff simulations, which is particularly important in the case of runoff projections for glacierized basin of hydropower reservoirs.

In a further study, the performance of five different melt model approaches ranging from a simple degree-day to a physically-based energy balance model was investigated over a multi-decadal period for Rhonegletscher (Swiss Alps). Based on a data sets of seasonal mass balance measurements and snow depth surveys of the years 2006-2012, model parameters could be accurately calibrated. All approaches, except the energy-balance model, showed no significant difference in performance over the 6-year period when calibrated to present climate conditions. The analysis revealed that model parameters fluctuate strongly from year to year as a result of an equifinality problem (i.e. different parameter combinations lead to

similar results). Despite the parameter variability, applying multi-year calibration instead of annually calibrated parameters involved only a slight decline in model performance. Compared to empirical melt formulations, the energy-balance model showed poorest performance despite its physical character. We expect that the forcing with data from an off-glacier weather station is responsible for this result as measured variables on non-glacierized ground might only poorly predict energy fluxes in the glacier-atmosphere boundary layer required for energy-balance calculations. Validation over the multi-decadal period by means of geodetically determined ice volume changes of six subperiods between 1929 and 2012 revealed that the choice of the melt equation can have a substantial effect on long-term mass balance simulation. While approaches of intermediate sophistication, including separate terms for temperature and radiation induced melt, performed best, melt models depending solely on air temperature resulted in generally too-positive mass balances. This result implies that the melt-temperature relationship does not remain constant in time and demands for recalibration for distinct climate conditions. The separation of temperature and radiation induced melt is expected to yield reasonably stable model parameters and make these models most suitable for long-term mass balance studies, particularly with respect to glacier projections into the future.

Furthermore, implications of light-absorbing impurities, i.e. Saharan dust and black carbon (BC), on surface albedo and on long-term glacier mass balance were investigated. The aim was to track the temporal evolution of snow impurity concentrations at the glacier surface and to assess associated influences on melt over a 100-year period (1914-2014) making use of the unique mass-balance record at Claridenfirn (Swiss Alps). The analysis was performed for two locations: (1) for a site in the accumulation area experiencing mainly mass gain and (2) for a site switching from accumulation to predominately ablation conditions. The presence of Saharan dust in snow reduces the summer albedo by about 0.005-0.009 on average and the annual mass balance by 21-41 $\mathrm{mm\,a^{-1}}$ depending on the location on the glacier. Results indicated that black carbon has a much stronger impact on the surface albedo and thus melt rates than mineral dust (7-9 times larger). On average, BC lowers the summer albedo by about 0.04-0.06 and the mass balance by 177-293 $\mathrm{mm\,a^{-1}}$. The effect of Saharan dust on albedo is reduced in the presence of strongly light-absorbing black carbon in snow due to a non-linear relationship between impurity concentration and albedo change. Thus, in comparison to pure snow conditions, the effect of BC is only three times higher than that of Saharan dust. In total, Saharan dust and black carbon amplify the mean annual glacier melt by about 14-18% compared to pure snow. This effect is more pronounced at the second site where intense melting entails an increased re-exposure of buried impurity-enriched snow layers leading to a distinct darkening of the glacier surface. At the first site, mostly positive mass balances result in a continuous burial of dust-bearing layers and hence to smaller impact on melt. Model results showed that during periods of intensive melting, as observed in the 1940s and in the 2000s, similarly high impurity concentration are accumulated at the glacier surface as during periods of exceptionally high depositions further amplifying melt rates.

## 5.2 Outlook

This thesis contributes to a better understanding of glacier mass balance and provides indications for improving mass balance simulations for the past and future. The study emphasizes the importance of an accurate estimation of the ice-thickness distribution, an appropriate melt model approach and draws attention to surface albedo changes due to enrichment of light-

absorbing impurities at the glacier surface during conditions of melt. However, distributed mass balance modelling has many aspects and has to scope with various difficulties as limited process understanding, restricted data availability or uncertainties introduced by extra- or interpolation. Hence, further investigation is required to improve the performance of glacier mass balance simulations. In particular, the following issues have emerged in the course of this work which need to be examined in more detail:

- The ice-thickness distribution is an important input quantity for ice flow modelling studies and a key factor for projections of the glacier and runoff evolution. Helicopter-based ground penetrating radar (GPR) measurements provide a unique opportunity to investigate the area-wide ice thickness distribution. However, for inferring the ice thickness inbetween radar profiles and for non-surveyed glaciers, estimation approaches are essential. As shown by the study presented in Chapter 2, there is a need for improving established ice-thickness estimation approaches as they have limitations when no measurements for calibration are available. The ice-thickness estimation approach used in this study has been further developed (Huss and Farinotti, 2012) and several other approaches have been proposed in the meanwhile (Paul and Linsbauer, 2012; Mcnabb et al., 2012; Clarke et al., 2013; van Pelt et al., 2013; Michel-Griesser et al., 2014). However, considerable uncertainties in ice-thickness calculations remain, particular when estimating the ice volume of single glaciers. Further advances in modelling techniques and an improved knowledge base to constrain model parameters are required. Airborne GPR measurements provide therefore a good opportunity to overcome these challenges.

- First attempts to infer the accumulation distribution on Rhonegletscher (Chapter 3) have been made by valley precipitation lapse rates and a gridded precipitation data set (RhiresD, MeteoSwiss). Both approaches considerably underestimated accumulation in the upper part of Rhonegletscher and clearly failed to reproduce the precipitation pattern. Snow depth measurements greatly help to improve snow accumulation estimates and provide invaluable information for mass balance modelling. For glaciers without a good data basis modelling techniques are required. But high spatial variability in precipitation distribution (Schwarb et al., 2001) and complex wind fields in high-mountainous terrain pose a significant challenge for correctly simulating accumulation. This is particularly problematic since uncertainties in the accumulation distribution seems to have strongest impact on the accuracy of runoff projections (Huss et al., 2014). Recently, several studies have looked into this issue and have examined the interannual persistence of the winter snow cover by means of remote sensing techniques (lidar remote-sensing, GPR measurements) providing area-wide snow depth distributions (Sold et al., 2013; Helfricht et al., 2014; Revuelto et al., 2014). Such analysis might contribute to a better understanding of spatial variability of snow accumulation and thus provide a basis for improved snow redistribution approaches.

- The comparative analysis of different melt model approaches revealed that temperature-index models including a separate term for radiation induced melt yield clearly better results than melt formulations based solely on air temperature. These findings are in accordance with results from an earlier study, carried out at the point scale, which reported that degree-day factors are not constant in time (Huss et al., 2009b). Nevertheless, it is important to extend this analysis to other glaciers in order to verify and confirm the presented results. Moreover, further emphasis should be put on the strong variability of melt

parameters, protruding over the six-year period of seasonal mass balance measurements, in order to better understand the cause of parameter variations.

- Differences in the altitudinal distribution of mass balance changes among the melt models may point to discrepancies in the air temperature field. Linear temperature lapse rates derived on the basis of air temperature data of weather stations in the surrounding were used. Recently, different studies have illustrated that the temperature regime on glaciers is distinctly different from off-glacier as air temperature on-glacier is damped by the temperature of the glacier surface and in addition affected by katabatic winds (Petersen and Pellicciotti, 2011; Carenzo, 2012). Only few studies have addressed this issue and provide approaches to infer the glacier air temperature regime based on off-glacier temperature data (Braithwaite et al., 2002; Shea and Moore, 2010). In general, their performance is poor (Petersen et al., 2013) and further examination is required to derive better methods for temperature extrapolation.

- As revealed by the melt model comparison study (Chapter 3), enhanced temperature-index models including the full shortwave radiation balance should be preferred for long-term mass balance studies. Hence, an accurate assessment of incoming shortwave radiation input i.e. taking into account the attenuation of clear-sky shortwave radiation by clouds, is crucial. However, evaluations of the cloud factor parameterisation have demonstrated that the parameterisation fails in case of a supressed daily cycle (e.g. in winter or for free-atmosphere weather stations). To obtain acceptable model results for shortwave radiation, more efforts should be made in improving the cloud factor parameterisation.

- According to the sensitivity analysis performed in Chapter 4, the removal rate of black carbon by meltwater has been recognized as the most sensitive parameter for the mass balance modelling controlling the fraction of snow impurities remaining in the snow/firn column. Up to now, only few studies have analysed the removal rate of snow impurities by meltwater (Conway et al., 1996; Doherty et al., 2013). A better knowledge about the effect of meltwater on light-absorbing particles would help to better assess the impact of mineral dust and black carbon on melt, particularly with respect to global warming and the potential re-exposure of buried impurity-enriched snow layers.

- Less well known is the influence of meltwater on the mobilization of mineral dust and other particles in/on bare ice. While the effect of dust and debris on ice melt has been widely studied (e.g. Adhikary et al., 2000; Nicholson and Benn, 2006; Oerlemans et al., 2009), redistribution and removal processes of impurities by meltwater is only poorly understood. To obtain a complete picture of the influence on mineral dust and black carbon on glacier melt, further research about the residence time of solid particles on ice surfaces is needed.

# Bibliography


Adhikary, S., Nakawo, M., Seko, K., and Shakya, B. (2000). Dust influence on the melting process of glacier ice : experimental results from Lirung Glacier, Nepal Himalayas. In *Debris-Covered Glaciers*, number 264. Proceedings of a workshop held at Seattle, Washington, USA, September 2000.

Aellen, M. (1995). Glacier mass balance studies in the Swiss Alps. *Zeitschrift für Gletscherkunde und Glazialgeologie*, 31(1–2):159–168.

Alfaro, S., Lafon, S., Rajot, J., Formenti, P., Gaudichet, A., and Maillé, M. (2004). Iron oxides and light absorption by pure desert dust: An experimental study. *Journal of Geophysical Research*, 109(D8).

Anderson, E. (1976). A Point Energy and Mass Balance Model of a Snow Cover. *NOAA Technical Report NWS*, 19:150pp.

Andreassen, L., Van den Broeke, M., Giesen, R., and Oerlemans, J. (2008). A 5 year record of surface energy and mass balance from the ablation zone of Storbreen, Norway. *Journal of Glaciology*, 54(185):245–258.

Anslow, F., Hostetler, S., Bidlake, W., and Clark, P. (2008). Distributed energy balance modeling of South Cascade Glacier, Washington and assessment of model uncertainty. *Journal of Geophysical Research*, 113(F02019).

Bahr, D. B., Meier, M. F., and Peckham, S. D. (1997). The physical basis of glacier volume-area scaling. *Journal of Geophysical Research*, 102(B9):20355–20362.

Bauder, A. (2003). Automatic surveying for hazard prevention on Glacier de Giétro. In *Milestones in Physical Glaciology From the Pioneers to a Modern Science*, volume 180, pages 1–3. Mitteilung der Versuchsanstalt für Wasserbau Hydrologie und Glaziologie, ETH Zürich. International Glaciological Symposium held in honor of Prof. Dr. Hans Röthlisberger on the occasion of his 80th birthday, 14. February 2003.

Bauder, A., Funk, M., and Huss, M. (2007). Ice volume changes of selected glaciers in the Swiss Alps since the end of the 19th century. *Annals of Glaciology*, 46:145–149.

Begert, M., Schlegel, T., and Krichhofer, W. (2005). Homogeneous temperature and precipitation series of Switzerland from 1864 to 2000. *International Journal of Climatology*, 25:65–80.

Beniston, M. (2012). Impacts of climatic change on water and associated economic activities in the Swiss Alps. *Journal of Hydrology*, 412–413:291–296.

Beniston, M. and Stoffel, M. (2014). Assessing the impacts of climatic change on mountain water resources. *Science of The Total Environment*, 493:1129–1137.

Bernhardt, M. and Schulz, K. (2010). SnowSlide: A simple routine for calculating gravitational snow transport. *Geophysical Research Letters*, 37(L11502).

Berthier, E., Schiefer, E., Clarke, G. K. C., Menounos, B., and Rémy, F. (2010). Contribution of Alaskan glaciers to sea-level rise derived from satellite imagery. *Nature Geoscience*, 3:92–95. doi:10.1038/ngeo737.

Bird, B. and Hulstrom, R. (1981). A simplified clear sky model for direct and diffuse insolation on horizontal surfaces. Technical Report SERI/TR-642-761, Solar Research Institute, Golden, Colorado.

Blatter, H. (1995). Velocity and stress fields in grounded glaciers: a simple algorithm for including deviatoric stress gradients. *Journal of Glaciology*, 41(138):333–344.

Bond, T., Bhardwaj, E., Dong, R., Jogani, R., Jung, S., Roden, C., Streets, D., and Trautmann, N. (2007). Historical emissions of black and organic carbon aerosol from energy-related combustion, 1850–2000. *Global Biogeochemical Cycles*, 21(2).

Bond, T., Doherty, S., Fahey, D., Forster, P., Berntsen, T., DeAngelo, B., Flanner, M., Ghan, S., Kärcher, B., Koch, D., Kinne, S., Kondo, Y., Quinn, P., Sarofim, M., Schultz, M., Schulz, M., Venkataraman, C., Zhang, H., Zhang, S., Bellouin, N., Guttikunda, S., Hopke, P., Jacobson, M., Kaiser, J., Klimont, Z., Lohmann, U., Schwarz, J., Shindell, D., Storelvmo, T., Warren, S., and Zender, C. (2013). Bounding the role of black carbon in the climate system: A scientific assessment. *Journal of Geophysical Research*, 118(11):5380–5552.

Bosshard, T., Kotlarsky, S., Ewen, T., and Schär, C. (2011). Spectral representation of the annual cycle in the climate change signal. *Hydrology and Earth System Sciences*, 15:2777–2788.

Braithwaite, R., Zhang, Y., and Raper, S. (2002). Temperature sensitivity of the mass balance of mountain glaciers and ice caps as a climatological characteristic. *Zeitschrift für Gletscherkunde und Glazialgeologie*, 38(1):35–61.

Braithwaite, R. J. (1995). Positive degree-day factors for ablation on the Greenland ice sheet studied by energy-balance modeling. *Journal of Glaciology*, 41(137):153–160.

Braithwaite, R. J. and Olesen, O. B. (1990). Response of the energy balance on the margins of the Greenland ice sheet to temperature changes. *Journal of Glaciology*, 36(123):217–221.

Braun, L. N., Weber, M., and Schulz, M. (2000). Consequences of climate change for runoff from alpine regions. *Annals of Glaciology*, 31(1):19–25.

Brock, B. and Arnold, N. (2000). A spreadsheet-based (microsoft excel) point surface energy balance model for glacier and snowmelt studies. *Earth Surface Processes and Landforms*, 25(6):649–658.

Brock, B., Willis, I., and Sharp, M. (2000). Measurement and parameterization of albedo variations at Haut Glacier d'Arolla, Switzerland. *Journal of Glaciology*, 46(155):675–688.

Brubaker, K., Rango, A., and Kustas, W. (1996). Incorporating radiation inputs into the snowmelt runoff model. *Hydrological Processes*, 10:1329–1343.

Brun, E. (1989). Investigation on wet-snow metamorphism in respect of liquid-water content. *Annals of Glaciology*, 13:22–26.

Brun, E., David, P., Sudul, M., and Brunot, G. (1992). A numerical model to simulate snow-cover stratigraphy for operational avalanche forecasting. *Journal of Glaciology*, 38:13–22.

Brun, E., Martin, E., Simon, V., Gendre, C., and Coleou, C. (1989). An energy and mass model of snow cover suitable for operational avalanche forecasting. *Journal of Glaciology*, 35(121):333–342.

Bundesamt für Energie (2011a). Engergieperspektiven für die Schweiz bis 2050. Technical report, Departement für Umwelt, Verkehr, Energie und Kommunikation, Bundesamt für Energie BFE, Switzerland.

Bundesamt für Energie (2011b). Wasserkraft. Technical report, Departement für Umwelt, Verkehr, Energie und Kommunikation, Bundesamt für Energie BFE, Switzerland.

Carenzo, M. (2012). *Distributed modelling of changes in glacier mass balance and runoff*. PhD thesis, Institute of Environmental Engineering, ETH Zurich. 294 p.

Carenzo, M., Pellicciotti, F., Rimkus, S., and Burlando, P. (2009). Assessing the transferability and robustness of an enhanced temperature-index glacier-melt model. *Journal of Glaciology*, 55(190):258–274.

Cazorzi, F. and Fontana, G. D. (1996). Snowmelt modelling by combining air temperature and a distributed radiation index. *Journal of Hydrology*, 181(1-4):169–187.

CH2011 (2011). *Swiss Climate Change Scenarios CH2011*. published by C2SM, MeteoSwiss, ETH, NCCR Climate, and OcCC, Zurich, Switzerland. 88 pp.

Chen, J. and Ohmura, A. (1990). Estimation of Alpine glacier water resources and their change since the 1870s. In *Hydrology in Mountainous Regions I*, pages 127–135. IAHS. Proceedings of two Lausanne Symposia, No. 193.

Clarke, G., Anslow, F., Jarosch, A., Radic, V., Menounos, B., Bolch, T., and Berthier, E. (2013). Ice volume and subglacial topography for western Canadian glaciers from mass balance fields, thinning rates, and a bed stress model. *Journal of Climate*, 26(12):4282–4303.

Cogley, J. G. (2010). Mass-balance terms revisited. *Journal of Glaciology*, 56(200):997–1001.

Collaud Coen, M., Weingartner, E., Schaub, D., Hueglin, C., Corrigan, C., Henning, S., Schwikowski, M., and Baltensperger, U. (2004). Saharan dust events at the Jungfraujoch: detection by wavelength dependence of the single scattering albedo and first climatology analysis. *Atmospheric Chemistry and Physics*, 4(11/12):2465–2480.

Conway, H., Gades, A., and Raymond, C. (1996). Albedo of dirty snow during conditions of melt. *Water Resources Research*, 32(6):1713–1718.

Corripio, J. (2002). *Modelling the energy balance of high altitude glacierised basins in the Central Andes*. PhD thesis, University of Edinburgh.

Corripio, J. (2003). Vectorial albegra algorithms for calculating terrain parameters from DEMs and solar radiation modelling in mountainous terrain. *International Journal of Geographical Information Science*, 17(1):1–23.

Dadic, R., Mott, R., Lehning, M., and Burlando, P. (2010). Wind influence on snow depth distribution and accumulation over glaciers. *Journal of Geophysical Research*, 115(F01012).

De Michele, C., Avanzi, F., Ghezzi, A., and Jommi, C. (2013). Investigating the dynamics of bulk snow density in dry and wet conditions using a one-dimensional model. *The Cryosphere*, 7:433–444.

Doherty, S., Grenfell, T., S, F., Hegg, D., Brandt, R., and Warren, S. (2013). Observed vertical redistribution of black carbon and other insoluble light-absorbing particles in melting snow. *Journal of Geophysical Research*, 118(11):5553–5569.

Domine, F., Taillandier, A.-S., and Simpson, W. (2007). A parameterization of the specific surface area of seasonal snow for field use and for models of snowpack evolution. *Journal of Geophysical Research*, 112(F02031).

Dumont, M., Gardelle, J., Sirguey, P., Guillot, A., D.Six, Rabatel, A., and Arnaud, Y. (2012). Linking glacier annual mass balance and glacier albedo retrieved from MODIS data. *The Cryosphere*, 6:1527–1539.

Dyurgerov, M. (2002). *Glacier mass balance and regime: data of measurements and analysis*. Boulder, CO, University of Colorado. Insititute of Arctic and Alpine Research. (INSTAAR Occasional Paper 55).

EEA (2009). Regional climate change and adaptation: The Alps facing the challenge of changing water resources. *Journal of Glaciology*, 8:143 pp.

Eichler, A., Schwikowski, M., Gäggeler, H., Furrer, V., Synal, H., Beer, J., Saurer, M., and Funk, M. (2000). Glaciochemical dating of an ice core from the upper Grenzgletscher (4200 m a.s.l.). *Journal of Glaciology*, 46(154):507–515.

Essery, R., Morin, S., Lejeune, Y., and Ménard, C. (2013). A comparison of 1701 snow models using observations from an alpine site. *Advances in Water Resources*, 55:131–148.

Farinotti, D., Bauder, A., Boes, R. M., Huss, M., Jouvet, G., and Widmer, F. (2011). Future glacier evolution and impact on the runoff regime in the catchments of Alpine reservoirs: The Aletsch area, Switzerland. In *Dams and Reservoirs under Changing Challenges*, pages 449–458. CRC Press, Taylor & Francis Group.

Farinotti, D., Huss, M., Bauder, A., and Funk, M. (2009a). An estimate of the glacier ice volume in the Swiss Alps. *Global and Planetary Change*, 68(3):225–231.

Farinotti, D., Huss, M., Bauder, A., Funk, M., and Truffer, M. (2009b). A method to estimate ice volume and ice thickness distribution of alpine glaciers. *Journal of Glaciology*, 55(151):422–430.

Farinotti, D., Usselmann, S., Huss, M., Bauder, A., and Funk, M. (2012). The runoff evolution in the Swiss Alps: Projections for selected high-alpine catchments based on ENSEMBLES scenarios. *Hydrological Processes*, 26:1909–1924. doi:10.1002/hyp.8276.

Finger, D., Heinrich, G., Gobiet, A., and Bauder, A. (2012). Projections of future water resources and their uncertainty in a glacierized catchment in the swiss alps and the subsequent effects on hydropower production during the 21st century. *Water Resources Research*, 48(W02521).

Finger, D., Pellicciotti, F., Konz, M., Rimkus, S., and Burlando, P. (2011). The value of glacier mass balance, satellite snow cover images and hourly discharge for improving the performance of a physically based distributed hydrological model. *Water Resources Research*, 47(W07519).

Finsterwalder, S. and Schunk, H. (1887). Der Suldenferner. *Zeitschrift des Deutschen und Oesterreichischen Alpenvereins*, 18:72–89.

Fischer, A. (2009). Calculation of glacier volume from sparse ice-thickness data, applied to Schaufelferner, Austria. *Journal of Glaciology*, 55(191):453–460.

Flanner, M., Zender, C., Hess, P., Mahowald, N., Painter, T., V.Ramanathan, and Rasch, P. (2009). Springtime warming and reduced snow cover from carbonaceous particle. *Atmospheric Chemistry and Physics*, 9:2481–2497.

Flanner, M., Zender, C., Randerson, J., and Rasch, P. (2007). Present-day climate forcing and response from black carbon in snow. *Journal of Geophysical Research*, 112(D11202).

Gabbi, J., Carenzo, M., Pellicciotti, F., Bauder, A., and Funk, M. (2014). A comparison of empirical and physically based glacier surface melt models for long-term simulations of glacier response. *Journal of Glaciology*, 60(224):1140–1154.

Gabbi, J., Farinotti, D., Bauder, A., and Maurer, H. (2012). Ice volume distribution and implications on runoff projections in a glacierized catchment. *Hydrology and Earth System Sciences*, 16:1–14.

Gabbi, J., Huss, M., Bauder, A., Schwikowski, M., and Cao, F. (2015). The impact of Saharan dust and black carbon on albedo and long-term mass balance of an Alpine glacier. *The Cryosphere Discussions*, 9(1):1133–1175.

Gardner, A., Moholdt, G., Cogley, J., Wouters, B., Arendt, A., Wahr, J., Berthier, E., Hock, R., Pfeffer, W., Kaser, G., Lightenberg, S., Bolch, T., Sharp, M., Hagen, J., van den Broeke, M., and Paul, F. (2013). A Reconciled Estimate of Glacier Contributions to Sea Level Rise: 2003 to 2009. *Science*, 314(6134):852–857.

Gardner, A. and Sharp, M. (2010). A review of snow and ice albedo and the development of a new physically based broadband albedo parameterization. *Journal of Geophysical Research*, 115(F01009).

Gerbaux, M., Genthon, C., Etchevers, P., Vincent, C., and Dedieu, J. P. (2005). Surface mass balance of glaciers in the French Alps: distributed modeling and sensitivity to climate change. *Journal of Glaciology*, 51(175):561–572.

Giesen, R. and Oerlemans, J. (2013). Climate-model induced differences in the 21st century global and regional glacier contributions to sea-level rise. *Climate Dynamics*, 41(11–12):3283–3300.

Ginot, P., Dumont, M., Lim, S., Patris, N., Taupin, J.-D., Wagnon, P., Gilbert, A., Arnaud, Y., Marinoni, A., Bonasoni, P., and Laj, P. (2014). A 10 year record of black carbon and dust from a Mera Peak ice core (Nepal): variability and potential impact on melting of Himalayan glaciers. *The Cryosphere*, 8:1479–1496.

Glen, J. W. (1955). The creep of polycrystalline ice. *Proceedings of the Royal Society of London, Ser. A*, 228(1175):519–538.

Gruber, S. (2007). A mass-conserving fast algorithm to parameterize gravitational transport and deposition using digital elevation models. *Water Resources Research*, 43(W06412).

Gudmundsson, G. (1999). A three-dimensional numerical model of the confluence area of Unteraargletscher, Bernese Alps, Switzerland. *Journal of Glaciology*, 45(150):219–230.

Haeberli, W. and Hoelzle, M. (1995). Application of inventory data for estimating characteristics of and regional climate-change effects on mountain glaciers: a pilot study with the European Alps. *Annals of Glaciology*, 21:206–212.

Haeberli, W., Hoelzle, M., Paul, F., and Zemp, M. (2007). Integrated monitoring of mountain glaciers as key indicators of global climate change: the European Alps. *Annals of Glaciology*, 46:150–160.

Helfricht, K., Schöber, J., Schneider, K., Sailer, R., and Kuhn, M. (2014). Interannual persistence of the seasonal snow cover in a glacierized catchment. *Journal of Glaciology*, 60(223):889–902.

Hess, H. (1904). *Die Gletscher*. Friedrich Vieweg und Sohn, Braunschweig.

Hock, R. (1999). A distributed temperature-index ice- and snowmelt model including potential direct solar radiation. *Journal of Glaciology*, 45(149):101–111.

Hock, R. (2003). Temperature index melt modelling in mountain areas. *Journal of Hydrology*, 282:104–115.

Hock, R. (2005). Glacier melt: a review of processes and their modelling. *Progress in Physical Geography*, 29(3):362–391.

Hock, R. and Holmgren, B. (2005). A distributed surface energy balance model for complex topography and its application to Storglaciären, Sweden. *Journal of Glaciology*, 51(172):25–26.

Hock, R., Jansson, P., and Braun, L. N. (2005). Modelling the response of mountain glacier discharge to climate warming. In Huber, U. M., Bugmann, H. K. M., and Reasoner, M. A., editors, *Global Change and Mountain Regions (An Overview of Current Knowledge)*, volume 23 of *Advances in Global Change Research*, pages 243–252. Springer.

Horton, P., Schaefli, B., Hingray, B., Mezghani, A., and Musy, A. (2006). Assessment of climate change impacts on Alpine discharge regimes with climate model uncertainty. *Hydrological Processes*, 20:2091–2109.

Houghton, J. et al. (2001). *Climate Change 2001: The Scientific Basis*. Report of the Intergovernmental Panel on Climate Change (IPCC). Cambridge University Press.

Hurkmans, R., Bamber, J., Davis, C., Joughin, I., Khvorostovsky, K., Smith, B., and Schoen, N. (2014). Time-evolving mass loss of the Greenland Ice Sheet from satellite altimetry. *The Cryosphere*, 8(5):1725–1740.

Huss, M. (2011). Present and future contribution of glacier storage change to runoff from macroscale drainage basins in Europe. *Water Resources Research*, 47(W07511).

Huss, M. (2012). Extrapolating glacier mass balance to the mountain-range scale: the European Alps 1900–2100. *Cryosphere*, 6:713–727.

Huss, M. and Bauder, A. (2009). 20th-century climate change inferred from four long-term point observations of seasonal mass balance. *Annals of Glaciology*, 50(1):207–214.

Huss, M., Bauder, A., and Funk, M. (2009a). Homogenization of long-term mass-balance time series. *Annals of Glaciology*, 50:198–206.

Huss, M., Bauder, A., Funk, M., and Hock, R. (2008a). Determination of the seasonal mass balance of four Alpine glaciers since 1865. *Journal of Geophysical Research*, 113(F1):F01015.

Huss, M. and Farinotti, D. (2012). Distributed ice thickness and volume of all glaciers around the globe. *Journal of Geophysical Research*, 117(F04010).

Huss, M., Farinotti, D., Bauder, A., and Funk, M. (2008b). Modelling runoff from highly glacierized alpine drainage basins in a changing climate. *Hydrological Processes*, 22:3888–3902. doi:10.1002/hyp.7055.

Huss, M., Funk, M., and Ohmura, A. (2009b). Strong Alpine glacier melt in the 1940s due to enhanced solar radiation. *Geophysical Research Letters*, 36(L23501).

Huss, M., Jouvet, G., Farinotti, D., and Bauder, A. (2010). Future high-mountain hydrology: a new parameterization of glacier retreat. *Hydrol. Earth Syst. Sci*, 14:815–829. doi:10.5194/hess-14-815-2010.

Huss, M., Zemp, M., Joerg, P., and Salzmann, N. (2014). High uncertainty in 21st century runoff projections from glacierized basins. *Journal of Hydrology*, 510:35–48.

Immerzeel, W., Petersen, L., Ragettli, S., and Pellicciotti, F. (2014). The importance of observed gradients of air temperature and precipitation for modeling runoff from a glacierized watershed in the Nepalese Himalayas. *Water Resources Research*, 50(3):2212–2226.

IPCC (2000). *IPCC Emission Scenarios (SRES)*. Nakicenovic N, Swart R (eds), Cambridge University Press. 570.

IPCC (2007). *Climate Change 2007. The Physical Scientific Basis. Contributions of Working Group I to the Fourth Assessment Report of the Intergovernmental Panel on Climate Change [Solomon, S., D. Qin, M. Manning, Z. Chen, M. Marquis, K.B. Averyt, M. Tignor and H.L. Miller (eds.)]*. Cambridge University Press, Cambridge, United Kingdom and New York, NY, USA.

IPCC (2013). *Climate Change 2013. The Physical Scientific Basis. Contributions of Working Group I to the Fifth Assessment Report of the Intergovernmental Panel on Climate Change [Stocker, T.F., D. Qin, G.–K. Plattner, M. Tignor, S.K. Allen, J. Boschung, A. Nauels,*

*Y. Xia, V. Bex and P.M. Midgley (eds.)]*. Cambridge University Press, Cambridge, United Kingdom and New York, NY, USA.

Iqbal, M. (1983). *An introduction to solar radiation*. London, Academic Press.

Jenk, T., Szidat, S., Bolius, D., Sigl, M., Gäggeler, H. W., Wacker, L., Ruff, M., Barbante, C., Boutron, C. F., and Schwikowski, M. (2009). A novel radiocarbon dating technique applied to an ice core from the Alps indicating late Pleistocene ages. *Journal of Geophysical Research*, 114(D14305).

Jenk, T., Szidat, S., Schwikowski, M., Gäggeler, H., Brütsch, S., Wacker, L., Synal, H.-A., and Saurer, M. (2006). Radiocarbon analysis in an alpine ice core: record of anthropogenic and biogenic contributions to carbonaceous aerosols in the past (1650–1940). *Atmospheric Chemistry and Physics*, 6(12):5381–5390.

Jóhannesson, T., Raymond, C. F., and Waddington, E. W. (1989). Time-scale for adjustment of glaciers to changes in mass balance. *Journal of Glaciology*, 35(121):355–369.

Johannesson, T., Sigurdsson, O., Laumann, T., and Kennett, M. (1995). Degree-day glacier mass-balance modelling with applications to glaciers in Iceland, Norway and Greenland. *Journal of Glaciology*, 41(138):345–358.

Jost, G., Moore, R. D., Menounos, B., and Wheate, R. (2012). Quantifying the contribution of glacier runoff to streamflow in the upper Columbia River Basin, Canada. *Hydrology and Earth System Sciences*, 16:849–860.

Jouvet, G., Huss, M., Funk, M., and Blatter, H. (2011). Modelling the retreat of Grosser Aletschgletscher, Switzerland, in a changing climate. *Journal of Glaciology*, 57(206):1033–1044.

Jouvet, G., Picasso, M., Rappaz, J., and Blatter, H. (2008). A new algorithm to simulate the dynamics of a glacier: theory and applications. *Journal of Glaciology*, 54(188):801–811.

Kääb, A. (2008). Glacier Volume Changes Using ASTER Satellite Stereo and ICESat GLAS Laser Altimetry. A Test Study on edgeoya, Eastern Svalbard. *Geoscience and Remote Sensing, IEEE Transactions on*, 46(10):2823–2830.

Kääb, A., Berthier, E., Nuth, C., Gardelle, J., and Arnaud, Y. (2012). Contrasting patterns of early twenty-first-century glacier mass change in the Himalayas. *Nature Geoscience*, 488:495–498.

Kappenberger, G. and Steingruber, S. (2014). Analisi chimica del manto nevoso sui ghiacciai basodino e clariden nel periodo 1992-2014. Technical report, Ufficio protezione aria, Sezione protezione aria, acqua e suolo, Dipartimento del territorio, Via C. Salvioni 2a, 6500 Bellizona, Switzerland.

Kaser, G., Grosshauser, M., and Marzeion, B. (2010). Contribution potential of glaciers to water availability in different climate regimes. *Proceedings of the National Academy of Sciences*, 107(47):20223–20227.

Kaspari, S., Painter, T., Gysel, M., Skiles, S., and Schwikowski, M. (2014). Seasonal and elevational variations of black carbon and dust in snow and ice in the Solu-Khumbu, Nepal and estimated radiative forcings. *Atmospheric Chemistry and Physics*, 14(15):8089–8103.

Kelleners, T., Chandler, D., McNamara, J., Gribb, M., and Seyfried, M. (2009). Modelling the water and energy balance of vegetated areas with snow accumulation. *Vadose Zone Journal*, 8:1013–1030.

Kellerer-Pirklbauer, A. (2008). The supraglacial debris system at the pasterze glacier, austria: spatial distribution, characteristics and tranpsort of debris. *Zeitschrift für Geomorphologie*, 52(Suppl.):3–25.

Klok, E. J. and Oerlemans, J. (2002). Model study of the spatial distribution of the energy and mass balance of Morteratschgletscher, Switzerland. *Journal of Glaciology*, 48(163):505–518.

Kobierska, F., Jonas, T., Zappa, M., Bavay, M., Magnusson, J., and Bernasconi, S. (2013). Future runoff from a partly glacierized watershed in Central Switzerland: A two-model approach. *Advances in Water Resources*, 55:204–214.

Koch, D. (2001). Transport and direct radiative forcing of carbonaceous and sulfate aerosols in the GISS GCM. *Journal of Geophysical Research*, 106(D17):20311–20332.

Kojima, K. (1967). Densification fo seasonal snow cover. In *Proc. Internat. Conf. Physics Snow Ice*, 1, pages 929–952.

Kondo, J. and Yamazaki, T. (1990). A prediction model for snowmelt, snow surface temperature and freezing depth using a heat balance method. *Journal of Applied Meteorology*, 29:375–384.

Kongoli, C. and Bland, W. (2000). Long-term snow depth simulations using a modified atmosphere-land exchange model. *Agricultural and Forest Meteorology*, 104(4):273–287.

Kopacz, M., Mauzerall, D., Wand, J., Leibensperger, E., Henze, D., and Singh, K. (2011). Origin and radiative forcing of black carbon transported to the himalayas and tibetan plateau. *Atmospheric Chemistry and Physics*, 11:2837–2852.

Kuhn, M. (1987). Micro-meteorological conditions for snow melt. *Journal of Glaciology*, 33(113):263–272.

Kuhn, M. (1995). The mass balance of very small glaciers. *Zeitschrift für Gletsscherkunde und Glazialgeologie*, 31:171–179.

Kustas, W. and Rango, A. (1994). A simple energy budget algorithm for the snowmelt runoff model. *Water Resources Research*, 30(5):1515–1527.

Lafon, S., Rajot, J., Alfaro, S., and Gaudichet, A. (2004). Quantification of iron oxides in desert aerosol. *Atmospheric Environment*, 38(8):1211–1218.

Lafon, S., Sokolik, I., Rajot, J., Caquineau, S., and Gaudichet, A. (2006). Characterization of iron oxides in mineral dust aerosols: Implications for light absorption. *Journal of Geophysical Research*, 111(D21207).

Lang, H. and Braun, L. N. (1990). On the information content of air temperature in the context of snow melt estimation. In Molnar, L., editor, *Hydrology of mountainous areas*, volume 190, pages 347–354. International Association of Hydrological Sciences. Proceedings of the Štrbské Pleso Symposium, Czechoslovakia, 1988.

Lavanchy, V., Gäggeler, H., Schotterer, U., Schwikowski, M., and Baltensperger, U. (1999). Historical record of carbonaceous particle concentrations from a European high-alpine glacier (Colle Gnifetti, Switzerland). *Journal of Geophysical Research*, 104(D17):21227–21236.

Le Meur, E., Gerbaux, M., Schäfer, M., and Vincent, C. (2007). Disappearance of an Alpine glacier over the 21st Century simulated from modelling its future surface mass balance. *Earth and Planetary Science Letters*, 261(3-4):367–374.

Lehning, M., Loewe, H., Ryser, M., and Raderschall, N. (2008). Inhomogeneous precipitation distribution and snow transport in steep terrain. *Water Resources Research*, 44(7).

Li, H., Ng, F., Li, Z., Qin, D., and Cheng, G. (2012). An extended "perfect-plasticity" method for estimating ice thickness along the flow line of mountain glaciers. *Journal of Geophysical Research*, 117(F01020).

Linsbauer, A., Paul, F., Machguth, H., and Haeberli, W. (2013). Comparing three different methods to model scenarios of future glacier change in the Swiss Alps. *Annals of Glaciology*, 54(63):241–253.

Liston, G. and Sturm, M. (1998). A snow-transport model for complex terrain. *Journal of Glaciology*, 44(148):498–516.

MacDougall, A. and Flowers, G. (2011). Spatial and Temporal Transferability of a Distributed Energy-Balance Glacier Melt Model. *Journal of Climate*, 24:1480–1498.

MacDougall, A., Wheler, B., and Flowers, G. (2011). A preliminary assessment of glacier-melt model parameter sensitivity and transferability in a dry subarctic environment. *The Cryosphere*, 5:1011–1028.

Machguth, H., Paul, F., Kotlarski, S., and Hoelzle, M. (2009). Calculating distributed glacier mass balance for the Swiss Alps from regional climate model output: A methodical description and interpretation of the results. *Journal of Geophysical Research*, 114.

Mayr, E., Hagg, W., Mayer, C., and Braun, L. (2013). Calibrating a spatially distributed conceptual hydrological model using runoff, annual mass balance and winter mass balance. *Journal of Hydrology*, 478:40–49.

Mcnabb, R., Hock, R., O'Neel, S., Rasmussen, L., Ahn, Y., Braun, M., Conway, H., Herreid, S., Joughin, I., Pfeffer, W., Smith, B., and Truffer, M. (2012). Using surface velocities to calculate ice thickness and bed topography: a case study at Columbia Glacier, Alaska, USA. *Journal of Glaciology*, 58(212):1151–1164.

Mellor, M. (1975). A review of basic snow mechanics. In *Snow mechanics: proceedings of the Grindelwald (international) symposium*, volume 114, pages 251–291. International Association of Hydrological Sciences.

Mercanton, P. L. (1916). Vermessungen am Rhonegletscher, Mensurations au Glacier du Rhône, 1874–1915. *Neue Denkschriften der Schweizerischen Naturforschenden Gesellschaft*, 52.

MeteoSwiss (2014a). Detection of Saharan dust event at the Jungfraujoch. http://www.-meteoschweiz.admin.ch/web/en/climate/observation_systems/upperair_observations/-saharan-dust-event.html. Online; accessed 13-October-2014.

MeteoSwiss (2014b). Norm values – maps. http://www.meteoschweiz.admin.ch/web/-en/climate/swiss_climate/Klimakarten_schweiz_1961-90.html. Online; accessed 17-September-2014.

Michel-Griesser, L., Picasso, M., Farinotti, D., Funk, M., and Blatter, H. (2014). Bedrock topography reconstruction of glaciers from surface topography and mass-balance data. *Computational Geosciences*, pages 1–20.

Mölg, T., Cullen, N., and Kaser, G. (2008). Mass balance of a slope glacier on Kilimanjaro and its sensitivity to climate. *International Journal of Climatology*, 28:881–892.

Müller, H. and Kappenberger, G. (1991). Claridenfirn-Messungen 1914-1984. Technical Report 40, Zürcher Geographische Schriften, Zürich.

Munro, D. (1989). Surface roughness and bulk heat transfer on a glacier: comparison with eddy calculation. *Journal of Glaciology*, 35(121):34–348.

Nash, J. and Sutcliffe, I. (1970). River flow forcasting through conceptual models part i – a discussion of principles. *Journal of Hydrology*, 10:282–290.

Nicholson, L. and Benn, D. (2006). Calculating ice melt beneath a debris layer using meteorological data. *Journal of Glaciology*, 52(178):463–470.

Nickus, U., Kuhn, M., Baltensperger, U., Delmas, R., Gäggeler, H., Kasper, A., Kromp-Kolb, H., Maupetit, F., Novo, A., Pichlmayer, F., Preunkert, S., Puxbaum, H., Rossi, G., Schöner, W., Schwikowski, M., Seibert, P., Staudinger, M., Trockner, V., Wagenbach, D., and Winiwarter, W. (1997). SNOSP: Ion deposition and concentration in high alpine snow packs. *Tellus*, 49B:56–71.

Nickus, U., Kuhn, M., Novo, A., and Rossi, G. (1998). Major element chemistry in alpine snow along a north-south transect in the Eastern Alps. *Atmospheric Environment*, 32(23):4053–4060.

Nomura, M. (1994). Studies on the delay mechanism of runoff to snowmelt. *Contributions form the Institute of Low Temperature Science, Hokkaido University*, 39:1–49.

Oerlemans, J. (1997). A flowline model for Nigardsbree, Norway: projection of future glacier length based on dynamic calibration with the historic record. *Annals of Glaciology*, 24:382–389.

Oerlemans, J. (2001). *Glaciers and climate change*. Balkema Publishers.

Oerlemans, J., Giesen, R., and van den Broeken, M. (2009). Retreating alpine glaciers: increased melt rates due to accumulation of dust (Vadret da Morteratsch, Switzerland). *Journal of Glaciology*, 55(192):729–736.

Ohara, N. and Kavvas, M. (2006). Field observations and numerical model experiments for the snowmelt process at a field site. *Advances in Water Resources*, 29(2):194–211.

Ohmura, A. (2001). Physical basis for the temperature-based melt-index method. *Journal of Applied Meteorology*, 40(4):753–761. doi: 10.1175/1520-0450.

Ohmura, A., Gilgen, H., and Wild, M. (1989). Global Energy Balance Archive (GEBA) Report 1: Introduction. *Zürcher Geographische Schriften*, 34:62pp.

Oke, T. (1987). *Boundary layer climates*. Routledge, second edition.

Painter, T., Barrett, A., Landry, C., Neff, J., Cassidy, M., Lawrence, C., McBride, K., and Farmer, G. L. (2007). Impact of disturbed desert soils on duration of mountain snow cover. *Geophysical Research Letters*, 34(L12502).

Painter, T., Deems, J., Belnap, J., Hamlet, A., Landry, C., and Udall, B. (2010). Response of Colorado River runoff to dust radiative forcing in snow. *Proceedings of the National Academy of Sciences*, 10:6603–6615.

Painter, T., Flanner, M., G. Kaser, B. M., VanCuren, R., and Abdalati, W. (2013). End of the Little Ice Age in the Alps forced by industrial black carbon. *Proceedings of the National Academy of Sciences*, 110:15216–15221.

Paul, F. and Linsbauer, A. (2012). Modeling of glacier bed topography from glacier outlines, central branch lines, and a DEM. *International Journal of Geographical Information Science*, pages 1–18. doi:10.1080/13658816.2011.627859.

Paul, F., Maisch, M., Rothenbuehler, C., Hoelzle, M., and Haeberli, W. (2007). Calculation and visualisation of future glacier extent in the Swiss Alps by means of hypsographic modelling. *Global and Planetary Change*, 55(4):343–357.

Pellicciotti, F., Brock, B., Strasser, U., Burlando, P., Funk, M., and Corripio, J. (2005). An enhanced temperature-index glacier melt model including the shortwave radiation balance: development and testing for Haut Glacier d'Arolla, Switzerland. *Journal of Glaciology*, 51(175):573–587.

Pellicciotti, F., Buergi, C., Immerzeel, W., Konz, M., and Shrestha, A. (2012). Challenges and Uncertainties in Hydrological Modeling of Remote Hindu Kush-Karakoram-Himalayan (HKH) Basins: Suggestions for Calibration Strategies. *Mountain Research and Development*, 32(1):39–50.

Pellicciotti, F., Carenzo, M., Helbling, J., Rimkus, S., and Burlando, P. (2009). On the role of subsurface heat conduction in glacier energy-balance modelling. *Annals of Glaciology*, 50:16–24.

Pellicciotti, F., Helbing, J., Rivera, A., Favier, V., Corripio, J., Araos, J., Sicart, J., and Carenzo, M. (2008). A study of the energy balance and melt regime on Juncal Norte Glacier, semi-arid Andes of central Chile, using melt models of different complexity. *Hydrological Processes*, 22:3980–3997.

Pellicciotti, F., Ragettli, S., Carenzo, M., and McPhee, J. (2013). Changes of glaciers in the Andes of Chile and priorities for future work. *Science of The Total Environment*. in press.

Pellicciotti, F., Raschle, T., Huerlimann, T., Carenzo, M., and Burlando, P. (2011). Transmission of solar radiation through clouds on melting glaciers: a comparison of parameterizations and their impact on melt modelling. *Journal of Glaciology*, 57(202).

Petersen, L. and Pellicciotti, F. (2011). Spatial and temporal variability of air temperature on a melting glacier: Atmospheric controls, extrapolation methods and their effect on melt modeling, Juncal Norte Glacier, Chile. *Journal of Geophysical Research*, 116. D23109.

Petersen, L., Pellicciotti, F., Juszak, I., Carenzo, M., and Brock, B. (2013). Suitability of a constant air temperature lapse rate over an Alpine glacier: testing the Greuell and Böhm model as an alternative. *Annals of Glaciology*, 54(63):120–130.

Popovnin, V. and Rozova, A. (2002). Influence of sub-debris thawing on ablation and runoff of the Djankuat Glacier in the Caucasus. *Nordic Hydrology*, 33(1):75–94.

Prodi, F. and Fea, G. (1979). A case of transport and deposition of Saharan dust over the Italian Peninsula and southern Europe. *Journal of Geophysical Research*, 84(C11):6951–6960.

Qian, Y., Flanner, M. G., Leung, L. R., and Wang, W. (2011). Sensitivity studies on the impacts of Tibetan Plateau snowpack pollution on the Asian hydrological cycle and monsoon climate. *Atmospheric Chemistry and Physics*, 11(5):1929–1948.

Radar Systemtechnik GmbH (2012). Website.

Raderschall, N., Lehning, M., and Schär, C. (2008). Fine-scale modeling of the boundary layer wind field over steep topography. *Water Resources Research*, 44(W09425).

Radic, V., Bliss, A., Beedlow, A., Hock, R., Miles, E., and Cogley, J. (2014). Regional and global projections of twenty-first century glacier mass changes in response to climate scenarios from global climate models. *Climate Dynamics*, 42(1-2):37–58.

Radić, V. and Hock, R. (2008). Analysis of scaling methods in deriving future volume evolutions of valley glaciers. *Journal of Glaciology*, 54(187):601–612.

Raes, F., Dingenen, R. V., Vignati, E., Wilson, J., Putaud, J., Seinfeld, J. H., and Adams, P. (2000). Formation and cycling of aerosols in the global troposphere. *Atmospheric Environment*, 34(25):4215–4240.

Ramanathan, V. and Carmichael, G. (2008). Global and regional climate changes due to black carbon. *Nature Geoscience*, 1:221–227.

Reid, T. and Brock, B. (2010). An energy-balance model for debris-covered glaciers including heat conduction through the debris layer. *Journal of Glaciology*, 56(199):903–916.

Revuelto, J., López-Moreno, J., Azorin-Molina, C., and Vicente-Serrano, S. M. (2014). Topographic control of snowpack distribution in a small catchment in the central Spanish Pyrenees: intra- and inter-annual persistence. *The Cryosphere*, 8:1989–2006.

Rogora, M., Mosello, R., Arisci, S., Brizzio, M., Barbieri, A., Balestrini, R., Waldner, P., Schmitt, M., Stähli, M., Thimonier, A., Kalina, M., Puxbaum, H., Nickus, U., Ulrich, E., and A.Probst (2006). An Overview of Atmospheric Deposition Chemistry over the Alps: Present Status and Long-term Trends. *Hydrobiologia*, 562:17–40.

Rolland, C. (2003). Spatial and Seasonal Variations of Air Temperature Lapse Rates in Alpine Regions. *Journal of Climate*, 16(7):1032–1046.

Roy, A., Royer, A., Montpetit, B., Bartlett, P., and Langlois, A. (2013). Snow specific surface area simulation using the one-layer snow model in the Canadian LAnd Surface Scheme (CLASS). *The Cryosphere*, 7:961–975.

Salzmann, N., Machguth, H., and Linsbauer, A. (2012). The Swiss Alpine glaciers repsonse to the global '2°C air temperature taget'. *Environmental Research Letters*, 7(044001).

Schaefli, B., Hingray, B., and Musy, A. (2007). Climate change and hydropower production in the Swiss Alps: quantification of potential impacts and related modelling uncertainties. *Hydrology and Earth System Sciences*, 11(3):1191–1205.

Scherrer, S. (2014). Die grössten Temperatursprünge im automatischen Messnetz der MeteoSchweiz. *Fachbericht MeteoSchweiz*, 248:1–42.

Schneeberger, C., Albrecht, O., Blatter, H., Wild, M., and Hock, R. (2001). Modelling the response of glaciers to a doubling in atmospheric $CO_2$: a case study of Storglaciären, northern Sweden. *Climate Dynamics*, 17(11):825–834.

Schneeberger, C., Blatter, H., Abe-Ouchi, A., and Wild, M. (2003). Modelling changes in the mass balance of glaciers of the northern hemisphere for a transient 2x$CO_2$ scenario. *Journal of Hydrology*, 282(1–4):145–163.

Schneiderbauer, S. and Prokop, A. (2011). The atmospheric snow-transport model: SnowDrift3. *Journal of Glaciology*, 57(203):526–542.

Schwarb, M., Daly, C., Frei, C., and Schär, C. (2001). *The mean annual and seasonal precipitation throughout the European Alps 1971–1990*, volume 2-6, 2-7. Hydrological Atlas of Switzerland.

Schwikowski, M., Seibert, P., Baltensperger, U., and Gäggeler, H. (1995). A study of an outstanding Saharan dust event at the high-alpine site Jungfraujoch, Switzerland. *Atmospheric Environment*, 29(15):1829–1842.

Sevruk, B. (1985). Correction of Measured Precipitation in the Alps Using the Snow Water Equivalent of New Snow. *Nordic Hydrology*, pages 49–58.

Shea, J. and Moore, R. (2010). Prediction of spatially distributed regiona-scale fields of air temperature and vapor pressure over mountain glaciers. *Journal of Geophysical Research*, 115. D23107.

Shi, Z., Krom, M., Bonneville, S., Baker, A., Bristow, C., Drake, N., Mann, G., Carslaw, K., McQuaid, J., Jickells, T., and Benning, L. (2011). Influence of chemical weathering and aging of iron oxides on the potential iron solubility of Saharan dust during simulated atmospheric processing. *Global Biogeochemical Cycles*, 25(2).

Sicart, J., Hock, R., and Six, D. (2002). Glacier melt, air temperature, and energy balance in different climates: The Bolivian Tropics, the French Alps, and northern Sweden. *Journal of Geophysical Research*, 113(D24):2156–2202.

Sigl, M. (2009). *Ice core based reconstruction of past climate conditions from Colle Gnifetti, Swiss Alps*. PhD thesis, Universitiy of Bern, Bern.

Singh, V. (2001). Kinematic wave modelling in water resources: a historical perspective. *Hydrological Processes*, 15:671–706.

Skiles, S., Painter, T., Deems, J., A.C.Bryant, and Landry, C. (2012). Dust radiative forcing in snow of the Upper Colorado River Basin: 2. Interannual variability in radiative forcing and snowmelt rates. *Water Resources Research*, 48(W07522).

SMA-Annalen (1864–2014). *Annalen der Schweizerischen Meteorologischen Anstalt*. Zürich.

Sokolik, I. and Toon, O. (1999). Incorporation of mineralogical composition into models of the radiative properties of mineral aerosol from UV to IR wavelengths. *Journal of Geophysical Research*, 104(D8):9423–9444.

Sold, L., Huss, M., Hoelzle, M., Andereggen, H., Joerg, P., and Zemp, M. (2013). Methodological approaches to infer end-of-winter snow distribution on alpine glaciers. *The Cryosphere*, 29(218):1047–1059.

Stahl, K., Moore, R. D., Shea, J. M., Hutchinson, D., and Cannon, A. J. (2008). Coupled modelling of glacier and streamflow response to future climate scenarios. *Water Resources Research*, 44:W02422.

Sterle, K., McConnell, J., Dozier, J., Edwards, R., and Flanner, M. (2013). Retention and radiative forcing of black carbon in eastern Sierra Nevada snow. *The Cryosphere*, 7:365–374.

Stokes, C., Popovnin, V., Aleynikov, S., Gurney, S., and Shahgedanova, M. (2009). Recent glacier retreat in the Caucasus Mountains, Russia, and associated increase in supraglacial debris cover and supra-/proglacial lake development. *Journal of Glaciology*, 55(191):444–452.

Strasser, U., Bernhardt, M., Weber, M., Liston, G., and Mauser, W. (2008). Is snow sublimation important in the alpine water balance? *The Cryosphere*, 2:53–66.

Sugiyama, S., Bauder, A., Zahno, C., and Funk, M. (2007). Evolution of Rhonegletscher, Switzerland, over the past 125 years and in the future: application of an improved flowline model. *Annals of Glaciology*, 46:268–274.

Taillandier, A.-S., Domine, F., Simpson, W., Sturm, M., and Douglas, T. (2007). Rate of decrease of the specific surface area of dry snow: Isothermal and temperature gradient conditions. *Journal of Geophysical Research*, 112(F03003).

Tangborn, W. (1999). A mass balance model that uses low-altitude meteorological observations and the area-altitude distribution of a glacier. *Geografiska Annaler*, 81 A(4):753–765.

Tarboton, D. and Luce, C. (1996). Utah energy balance snow accumulation and melt model (UEB): computer model technical description and users guide. Technical report, Utah Water Resources Laboratory, Logan.

Uhlmann, B., Jordan, F., and Beniston, M. (2013). Modelling runoff in a Swiss glacierized catchment - Part I: methodology and application in the Findelen basin under a long-lasting stable climate. *International Journal of Climatology*, 33(5):1293–1300.

van der Linden, P. and Mitchell, J. (2009). *ENSEMBLES: Climate Change and its Impacts: Summery of research and results from the ENSEMBLES project*. Met Office Hadley Centre, Exeter EX1 3PB, UK. 160pp.

van Pelt, W., Oerlemans, J., Reijmer, C., Pettersson, R., Pohjola, V., Isaksson, E., and Divine, D. (2013). An iterative inverse method to estimate basal topography and initialize ice flow models. *The Cryosphere*, 7(3):987–1006.

VAW (1998). Mauvoisin – Giétrogletscher – Corbassièregletscher. Glaziologische Studien im Zusammenhang mit den Stauanlagen Mauvoisin. Im Auftrag der Elektrizitätsgesellschaft Lauffenburg AG, (M. Funk, unveröffentlicht).

Verbunt, M., Gurtz, J., Jaspera, K., Langa, H., P., W., and Zappa, M. (2003). The hydrological role of snow and glaciers in alpine river basins and their distributed modeling. *Journal of Hydrology*, 282:36–55.

Vieli, A., Funk, M., and Blatter, H. (1997). Griesgletscher: Berechnungen des Gletscherfliessens und Perspektiven für die Zukunft. *Wasser Energie Luft*, 89(5/6):107–114.

Vionnet, V., Martin, E., Masson, V., Guyomarc'h, G., Naaim-Bouvet, F., Prokop, A., Durand, Y., and Lac, C. (2014). Simulation of wind-induced snow transport and sublimation in alpine terrain using a fully coupled snowpack/atmosphere model. *The Cryosphere*, 8:395–415.

Wagenbach, D. and Geis, K. (1989). The mineral dust record in a high altitude Alpine glacier (Colle Gnifetti, Swiss Alps). In Leinen, M. and Sarnthein, M., editors, *Paleoclimatology and Paleometeorology: Modern and Past Patterns of Global Atmospheric Transport*, volume 282, pages 543–564. Springer Netherlands.

Wagenbach, D., Preunkert, S., Schäfer, J., Jung, W., and Tomadin, L. (1996). Northward Transport of Saharan Dust Recorded in a Deep alpine Ice Core. In Guerzoni, S. and Chester, R., editors, *The Impact of Desert Dust Across the Mediterranean*, volume 11 of *Environmental Science and Technology Library*, pages 291–300. Springer Netherlands.

Warren, S. (1984). Impurities in snow: Effects on albedo and snowmelt (review). *Annals of Glaciology*, 5:177–179.

Winstral, A. and Marks, D. (2002). Simulating wind fields and snow redistribution using terrain-based parameters to model snow accumulation and melt over a semi-arid mountain catchment. *Hydrological Processes*, 16:3585–3603.

Winstral, A., Marks, D., and Gurney, R. (2013). Simulating wind-affected snow accumulations at catchment to basin scales. *Advances in Water Resources*, 55:64–79.

Zemp, M., Paul, F., Hoelzle, M., and Haeberli, W. (2008). Glacier fluctuations in the European Alps, 1850–2000: an overview and spatio-temporal analysis of available data. In *Darkening Peaks: Glacier Retreat, Science, and Society*, pages 152–167. Berkeley and Los Angeles: University of California Press.

Zhang, Y., Wang, S., Barr, A., and Black, T. (2008). Impact of snow cover on soil temperature and its simulation in a boreal aspen forest. *Cold Regions Science and Technology*, 52(3):355–370.

Zuzel, J. and Cox, L. (1975). Relative importance of meteorological variables in snowmelt. *Water Resources Research*, 11(1):174–176.

# Acknowledgements

Many people have accompanied me along the way and have helped, supported, motivated, encouraged and inspired me. All those I would like to express my heartfelt thanks.

Above all, I would like to express my gratitude to Martin Funk. He gave me the opportunity of doing a PhD at VAW, which was a great experience. I would like to thank him for his patience, the continuous support, his kindness and his always helpful advice. He kept me free of obligation and provided me a lot of freedom. He initiated and enabled the joint project with Francesca and Marco which was a turning point in my PhD. Thank you for that, Martin!
Then I would like to thank my supervisor Andreas Bauder which has accompanied me not only during my PhD, but also during my Bachelor and Master thesis. He was always there for me and had always an open ear to any problems. He provided me with valuable advice and helped me to improve many reports, manuscripts, posters and presentations. Thank you also a lot for your great support on fieldwork!
A very special thank goes to Francesca Pellicciotti who supervised me in my second project. It was a great experience to work with her together. She inspired me a lot with her enthusiasm, her structured work style and her amazing work flow. I am very grateful for her precious advice, her extensive knowledge and her continuous encouragement. She was always available for my questions and problems and gave me a lot of her time. Thank you so much, Francesca!
Furthermore, I would like to thank Matthias Huss for offering me the opportunity to make the Claridenfirn analysis. I enjoyed this project a lot and appreciated his support, his constructive comments and his enthusiasm! I am very happy that I had the chance to work with him.
Many thanks to Marco Carenzo who supported me with his collaboration, his knowledge and his support. I am grateful for the interest and assistance of Margit Schwikowski who provided me with useful advice and competent knowledge in chemical related questions.
I thank Thomas Wyder for assembling and entertaining the field equipment and all those who helped me in the field and took the trouble to undertake the long travel to Rhone- or Griesgletscher and to carry heavy backpacks.
I wish to thank all my colleagues at VAW for the good time, the good chats and discussions and the always pleasant atmosphere, thanks Claudia Ryser, Patrick Becker, Isabelle Frei, Daniel Farinotti, Arne Keller, Pierre Dalban, Claudia Röösli, Ivo Weidmann, Thomas Wyder, Oliver Nicolay, Martin Lüthi, Martin Truffer, Patrick Riesen, Jerome Failletaz, Stefanie Usselmann, Kolumban Hutter, Nina Zoller, Marco Cortesi, Marcel Knöri, Sahara Thompson, Jed Brown, Hermann Bösch and Bruno Nedela.
My deepest gratitude goes to my parents and Albin Kretz for their help, their support, their continuous love and encouragement. They were always there, listened when I needed and believed in me when I didn't.

This thesis was founded by the Swiss National Science Foundation within the framework of the National Research Program NRP61 *Sustainable water management* (http://www.nfp61.ch).